Stony Brook University

A Role for HMGB2 in Mammalian Neurogenesis and Stroke

A Dissertation Presented

By

Robert Bronstein

To

The Graduate School

in Partial Fulfillment of the Requirements

for the Degree of

DOCTOR OF PHILOSOPHY

in

Neuroscience

Stony Brook University

May 2015

Stony Brook University

The Graduate School

Robert Bronstein

We, the dissertation committee for the above candidate for the
Doctor of Philosophy degree,
hereby recommend acceptance of this dissertation.

Styliani-Anna E. Tsirka Ph.D. - Dissertation Advisor
Professor, Department of Pharmacological Sciences

William Van Nostrand, Ph.D. – Chairperson of Defense
Professor, Department of Neurosurgery

Shaoyu Ge, Ph.D.
Associate Professor, Department of Neurobiology and Behavior

Adan Aguirre, Ph.D.
Assistant Professor, Department of Pharmacological Sciences

Mirjana Maletic-Savatic, Ph.D. – Outside Committee Member
Assistant Professor, Department of Pediatrics, Baylor College of Medicine

This dissertation has been accepted by the Graduate School

Charles Taber
Dean of the Graduate School

Abstract of the Dissertation

A Role for the Chromatin-Associated Protein HMGB2 in Mammalian Neurogenesis and Thalamic Ischemia.

by

Robert Bronstein

Doctor of Philosophy

in

Neuroscience

Stony Brook University

2015

Stroke results in areas of neuronal cell death with concomitant inflammation and edema in the surrounding tissues. Ischemia in the thalamus can present as an accumulation of many smaller lacunar infarcts leading to potential cognitive deficits and central post-stroke pain syndromes, for which curative therapies are lacking. The capacity of the brain to repair itself rests upon the robust response of adult neurogenesis, and gliogenesis, to formidable ischemic conditions. In this study I assess the role chromatin modulator HMGB2 plays in both neurogenesis/gliogenesis and adult thalamic ischemia. Firstly, we demonstrate that this protein can affect the transition between the creation of new neurons and glial cells during development. Secondly, following the induction of stroke in the thalamus, loss of HMGB2 lowers the rate of apoptotic cell death and differentially modulates behavioral outcomes of the ischemic lesion. The numerous intra and extra-cellular roles for HMGB2 in a diverse array of brain functions makes it an important molecule for further study.

Table of Contents

List of Figures

List of Tables

List of Abbreviations

5-hmC	5-Hydroxymethylcytosine
Akt	Protein Kinase B
AraC	Arabinofuranosyl Cytidine
ARC	Arcuate Nucleus
AT	Adenine & Thymine
BMI1	Polycomb Ring Finger Oncogene
BMP	Bone Morphogenetic Protein
BrdU	Bromodeoxyuridine
CC	Corpus Callosum
CC1	Adenomatous Polyposis Coli
CNS	Central Nervous System

CXCR4	CXC Chemokine Receptor 4
DAPI	4',6-diamidino-2-phenylindole
DIV	Days In-Vitro
DCX	Doublecortin
DG	Dentate Gyrus
DNA	Deoxyribonucleic Acid
DNMT	Deoxyribonucleic Methyltransferase
ECM	Extra Cellular Matrix
EED	Embryonic Ectoderm Development
EGF	Epidermal Growth Factor
ESC	Embryonic Stem Cell
ET-1	Endothelin 1
EZH1	Enhancer Of Zeste Homolog 1
FGF	Fibroblast Growth Factor
FSHD	Facioscapulohumeral Muscular Dystrophy
GCL	Granule Cell Layer
GFAP	Glial Fibrillary Acid Protein
GPI	Glycosylphosphatidyl Inositol
H1	Linker Histone H1
H2A	Histone H2A
H2B	Histone H2B
H3	Histone H3
H4	Histone H4

HMGA2	High Mobility Group A2
HMGB2	High Mobility Group B2
ICH	Intra-Cerebral Hemorrhage
KO	Knock Out
lncRNA	long non-coding RNA
Mash1	Mammalian Achaete Scute Homolog 1
ME	Median Eminence
miRNA	micro RNA
NB	Neuroblast
NG2	Neural/Glial Antigen 2
NPC	Neural Progenitor Cell
NSC	Neural Stem Cell
NSPC	Neural Stem/Progenitor Cell
OB	Olfactory Bulb
Oct4	Octamer Binding Transcription Factor 4
OPC	Oligodendrocyte Precursor Cell
PFA	Paraformaldehyde
pAkt	Phosphorylated Protein Kinase B
PcG	Polycomb Group Proteins
PN	Pyramidal Neuron
PRC	Polycomb Repressive Complex
PRE	Polycomb Response Element
PSA–NCAM	Polysialated Neural Cell Adhesion Molecule

PTM	Post-Translational Modification
PVN	Paraventricular Nucleus
RG	Radial Glia
RGC	Radial Glial Cell
RMS	Rostral Migratory Stream
RNA	Ribonucleic Acid
SAH	Sub-Arachnoid Hemorrhage
SHH	Sonic Hedgehog
SDF1	Stromal Derived Factor 1
SGZ	Sub-Granular Zone
STAT	Signal Transducer and Activator of Transcription
SUZ12	Polycomb Repressive Complex 2 Subunit
SVZ	Sub-Ventricular Zone
TIA	Transient Ischemic Attack
tMCAo	Transient Middle Cerebral Artery Occlusion
TRE	Trithorax Response Element
trxG	Trithorax Group Proteins
V(D)J	Variable Diversity Joining
VZ	Ventricular Zone
YY1	Ying Yang 1 (transcription factor)

Acknowledgements

Without a doubt the first person I have to thank for providing me with the requisite tools and knowledge in the completion of this dissertation is my advisor Dr. Stella Tsirka. Since joining the lab in the spring of 2011 she has been an extremely steady and patient guide, and really helped me to understand how to think about experiments, controls, and most importantly the big picture scientific questions. Stella has had the uncanny ability to help me focus on discrete sets of experimental problems, especially given my propensity for tangents. All in all its been a wonderful experience being a graduate student in Stella's lab, with the friendly and collegial environment she so effortlessly fosters.

Secondly I have thank the members of my thesis committee Dr. William Van Nostrand, Dr. Shaoyu Ge, Dr. Adan Aguirre and my outside committee member Dr. Mirjana Maletic-Savatic. Their questions and advice during our annual meetings have been invaluable in refining the goals of my doctoral research as well as providing me with potential new directions – many times with the help of expertise, and reagents, from their own laboratories.

I also want to thank current and former members of the Tsirka lab for making it such a scientifically rich and fun place to work everyday. I'm grateful to Dr. Ari Abraham, many aspects of whose work I took over upon his graduation, for teaching me about confocal microscopy as well as critical questions in the field of neurogenesis. I also want to thank Dr. Jillian Nissen for considerable help with qRT-PCR experiments and data interpretation, as well as Dr. Luisa Torres Duque for advice on behavioral assessment of gait characteristics. I want to thank Jeremy

Miyauchi for being a great bench neighbor and always knowing what is happening in our cell culture room. I would like to thank Joan Danver for her constant upbeat attitude even amidst very time-consuming and frustrating behavioral experiments. Lastly, I want to thank my undergraduate student Chris Lopez for always being able to distract me in lab and remind me of my mid 1990s musical tastes.

A large number of labs and faculty/staff members have been instrumental in my time as a graduate student at SBU. Odalis Hernandez has been extremely helpful with any and all administrative issues as well as during my time in the Med Into Grad program. I want to thank all the members of the Colognato lab as their assistance with reagents and knowledge of glial biology was extremely helpful. Lastly I want to thank the administrative staff of both the Pharmacological Sciences and Neurobiology and Behavior departments for their support and help over the years.

Finally I would like to thank my family, especially my mom and dad and my brothers Alex and Gary for their unflappable support and encouragement. My mom and older brother Gary are both physicians, and I have always looked up to them immensely. From helping in the nephrology department at a Moscow hospital when I was little, to listening to my brothers stories of residency – those moments really sowed the seed for where I am today. I met my future wife, Dr. Amy DeMarco, while doing research rotations in my first year of graduate school and for that I am most thankful. Her unwavering love and support has really propelled me through this process and will continue to do so for many years to come.

Chapter I

General Introduction

Mammalian Neurogenesis & Gliogenesis

Neural stem cells (NSCs) in the developing and adult mammalian central nervous system (CNS) produce a diverse range of specialized cell types that are exquisitely fit to function in as complex an environment as the adult human brain - which houses one hundred billion neurons with one hundred trillion synaptic connections. During embryonic and perinatal development the mammalian cerebral cortex undergoes sustained waves of neurogenesis and gliogenesis, ultimately culminating in several discrete neurogenic niches in the adult brain.

History of Neurogenesis Research

In the mid 20th century the entrenched scientific opinion maintained that the postnatal CNS was a static environment with no neuronal turnover. The experiments of Joseph Altman and colleagues (Altman, 1962; 1963; Altman and Bayer, 1975; Altman and Das, 1965) in the 1960s began to incrementally shift the tide of opinion towards acceptance of adult neurogenesis. In one experiment, electrolytic lesions of the lateral geniculate body in adult Long-Evans hooded rats were performed with simultaneous stereotaxic injections of ^{3}H-thymidine, a radioactive nucleotide analogue (Altman, 1962). This approach allowed the investigators to assess the label-retaining cells at different time-points following injury. (Altman, 1962) uncovered labeling of not only injury-reactive glial cells, but neuroblasts (NBs) and cortical pyramidal neurons (PNs) in areas at great distances from the electrolytic focus. Similar results were obtained when observing cells specifically in the dentate gyrus of the hippocampal formation in rats (Altman and Bayer, 1975). In the 1980s a clearer picture of adult neurogenesis in vertebrates started taking shape, led by the laboratory of Fernando Nottebohm. (Paton and Nottebohm, 1984) not

only observed turnover of adult canary (Serinus canaria) neuronal pools via ^{3}H-thymidine labeling but also demonstrated that these cells were functionally integrating into neural circuits critical to song generation. The seminal finding in rodents came in the late 1990s, when (Alvarez-Buylla and Doetsch, 1999) demonstrated that sub-ventricular zone (SVZ) glial fibrillary acid protein positive (GFAP) astrocyte populations were responsible for giving rise to neuroblasts. The antimitotic agent AraC was stereotaxically injected into the lateral ventricle of mice, effectively stopping the proliferation of all SVZ and ventricular zone (VZ) cells – however following natural elimination of the drug, cell division of GFAP+ cells was once again evident (Alvarez-Buylla and Doetsch, 1999). Upon infection of this putative NSC population with a retrovirus (which only integrates into the DNA of actively dividing cells), label retaining neuroblasts were tracked to the olfactory bulb (OB) where they differentiated into different interneuron populations (Alvarez-Buylla and Doetsch, 1999). Since that time, considerable experimental evidence has demonstrated that robust neurogenesis occurs within three distinct CNS niches: within the olfactory system of rodents the SVZ gives rise to OB interneurons, the dentate gyrus of the hippocampal formation, as well as more recently around the 3rd ventricle by tanycytes (a radial-glia like cell population) whose descendants add fresh interneurons to the arcuate and paraventricular nuclei of the hypothalamus (Bennett et al., 2009; Haan et al., 2013; Lim and Alvarez-Buylla, 2014; Robins et al., 2013a).

Early Neurogenesis and Cortical Development

In the developing murine cerebral cortex radial glial (RG) processes stretch from the ventricular to the pial surface, serving as migratory scaffolds for excitatory (Glutamatergic) pyramidal cells moving into their final laminar positions (Marin et al.,

2010). On the other hand, GABAergic interneuron progenitors are primarily located within the lateral, medial and caudal ganglionic eminences during development and undergo a tangential/laminar migration to integrate into appropriate cortical circuitry (Huang, 2014).

SVZ & Gliogenesis

Cortical neurogenesis begins to wane around embryonic day 17.5 (E17.5) giving way to increased periods of astrogliogenesis and oligodendrogenesis, with astrocytes being produced until approximately postnatal day 2 (p2) followed by oligodendrocyte development which continues until approximately p10 (Kriegstein and Alvarez-Buylla, 2009) (Lim and Alvarez-Buylla, 2014). In the perinatal period (on either side of birth) RG fibers retract their apical arbors and become contained entirely within the SVZ, comprising a niche which contains: ependymal cells, microglia, astrocytes, axonal projections as well as a vast vascular plexus (Figure I-1A+B) (Kokovay et al., 2010; Tong et al., 2014). In the adult mouse brain, under physiological conditions, the SVZ gives rise primarily to OB interneurons, as well as astrocytes, and neural/glial antigen 2+ (NG2+) oligodendrocyte progenitors (OPCs) which migrate into the white matter (e.g. corpus callosum CC) (Abraham et al., 2013b; Aguirre et al., 2004).

At its core, the SVZ houses three primary cell types – namely B, C and A cells (Lim and Alvarez-Buylla, 2014). B cells are comprised of B1 and B1a NSCs, with B1a cells being the ones to extend their primary cilia through the center of the pinwheel structures that make up the lateral ventricle walls (Kriegstein and Alvarez-Buylla, 2009). The B cell population can also be parsed by virtue of its cell cycle dynamics, with quiescent or epidermal growth factor- (EGFR-) and actively dividing or EGFR+, with the former

laying the foundation for sustained adult neurogenesis and the latter being an immediate reservoir for the A intermediate progenitor cell population (Kriegstein and Alvarez-Buylla, 2009; Lim and Alvarez-Buylla, 2014). Just as the B cells have the propensity for symmetric and assymetric division, so goes the story for the intermediate progenitor population. In the end they primarily give rise to C type neuroblasts defined by expression of polysialated neural cell adhesion molecule (PSA-NCAM) and doublecortin (DCX), as well OPCs and mature astrocytes of various kinds (Alvarez-Buylla and Doetsch, 1999; Kriegstein and Alvarez-Buylla, 2009; Lim and Alvarez-Buylla, 2014). The overall process of adult SVZ neurogenesis involves many more distinct players such as microglia, extracellular matrix (ECM) proteins as well as netrins and semaphorins which are crucial in neuroblast migration and axon guidance (Borrell et al., 2012; Sawamoto et al., 2006; Xu et al., 2014), and paints a complex picture which, at least in mice, is crucial for olfaction and glial cell turnover.

Neurogenesis in the Dentate Gyrus of the Hippocampal Formation

The subgranular zone (SGZ) of the dentate gyrus (DG) houses more limited potential progenitors than the SVZ, with the vast majority of NSCs giving rise to dentate granule cells (DGCs) (Lim and Alvarez-Buylla, 2014). Initially quiescent NSCs move into a more actively dividing state to asymmetrically produce a large number of DCX+ neuroblasts – most of which are pruned off during their development by microglia (Sierra et al., 2010). A small number of neuroblasts fully mature into DG granule neurons and participate in computations involving learning and memory formation (Encinas et al., 2011). Newborn neurons in the DG demonstrate a period of enhanced experience dependent plasticity, deficits in which, result in shortfalls in core hippocampus dependent

functions (Ge et al., 2007). A number of epigenetic choreographers are critical to the development of NSCs into fully functional adult dentate granule neurons - specifically in relations to the cell fate transitions upon which synaptic plasticity heavily relies (Ma et al., 2010). Crosstalk amongst pathways as diverse as DNA methylation, histone modifications and long non-coding RNAs is essential for the proper pruning and maturation of adult newborn DG neurons (Jobe et al., 2012). One of the primary aspects of mouse, as well as human, behavior that is largely hippocampus dependent is contextual memory – which is heavily diminished following a targeted acute reduction in adult DG neurogenesis (Akers et al., 2014; Sahay et al., 2011).

Hypothalamic Neurogenesis at the 3rd Ventricle

The more recently characterized hypothalamic neurogenic niche exists in direct adherence with the posteroventral aspect of the 3rd ventricle (Haan et al., 2013) (Xu et al., 2005). The principal cellular actors driving neurogenesis in this region are various subpopulations of tanycytes – a radial glia-like population of progenitors whose cell bodies reside among the numerous ependymocytes lining the 3rd ventricle walls. Alpha and beta tanycytes extend long Nestin+/Vimentin+ processes into various hypothalamic nuclei (arcuate, paraventricular) along which immature interneurons migrate to their final position prior to establishing functional connectivity (Bolborea and Dale, 2013; Cheng, 2013; Robins et al., 2013a). In addition to the typical subependymal NSC populations, NG2+ progenitors in the 3rd ventricle niche have also been shown to give rise to interneurons in adulthood – differentiating them significantly from the oligodendrocyte progenitor role they serve in the SVZ (Robins et al., 2013b). The various hypothalamic

nuclei in question are critical to processes ranging from mating, to feeding control, to thermoregulation (Kokoeva et al., 2005; Li et al., 2014).

Factors Involved in Mammalian Neurogenesis

There are a considerable number of protein as well as modified RNA molecules involved in the control of neurogenesis and gliogenesis in mammals (Lim and Alvarez-Buylla, 2014). Common factors crucial to tissue development and organ morphogenesis such as Wnt, Bone Morphogenetic Proteins (BMPs), Sonic Hedgehog (SHH), and others - are also important in the embryonic to adult progression of neurogenic and gliogenic cascades (Ming and Song, 2011). In addition, recently it has been demonstrated that long non-coding RNAs (lncRNAs) also help to orchestrate adult newborn DG granule cell development and function (Jobe et al., 2012). Of particular interest for our group were proteins that modulate progression of the cell cycle in NSPCs and as such function to modify neurogenic and gliogenic fates (Nishino et al., 2008). One such protein is high mobility group A2 (HMGA2) which has been found to decrease in abundance within the SVZ from embryonic ages into adulthood, and it is in fact this downregulation which allows the critical tumor suppressor protein p16 to apply a break to the cell cycle of NSCs later in life (Nishino et al., 2008). Additionally the micro RNA (miRNA) let-7b also has a regulatory role in this system, modifying the early levels of HMGA2 expression in the embryonic SVZ (Nishino et al., 2008; Rybak, 2009). HMGA2 comes from a large family of chromatin-associated proteins with known roles in transcriptional regulation and chromatin dynamics (Kishi et al., 2012).

HMG(B) Chromatin Architectural Proteins

The HMGB family of chromatin structural proteins are a ubiquitous collection of DNA binding proteins which lack sequence specificity in mammals (Stros, 2010). Their preference for binding sites lies within the minor groove of DNA in adenine & thymine (AT) rich regions (Stros, 2010). HMG(B) group proteins are structurally composed of two DNA box binding motifs connected by a short linker, plus an intracellular C-terminal tail (Stros, 2010). The two best characterized proteins within this family, HMGB1 and HMGB2, differ by just five amino acids within the C-terminal tail – which helps stabilize the interaction of these proteins with the linker histone H1, while the DNA box motifs bind different aspects of the nucleosomal structure (Prasad et al., 2007; Stros, 2010).

Given their promiscuous binding characteristics the mammalian HMG(B) family of proteins have been implicated in a number of critical functions, ranging from assisting RAG proteins to bind certain DNA motifs during V(D)J recombination in B cells and T cells within lymphoid organs, to regulating chondrocyte fate and cartilage surface maintenance via the canonical β-catenin pathway (Schatz and Swanson, 2011; Taniguchi et al., 2009a). In *Drosophila melanogaster* an additional epigenetic role has been ascertained for Dsp1, a homologue of HMGB1/2 (Déjardin et al., 2005; Janke et al., 2003). Dsp1 appears to have the ability to recruit PcG and trxG proteins to DNA which results in either silencing or promotion of gene transcription, respectively (Déjardin et al., 2005). The specificity of Dsp1 is embedded within its ability to recognize specific DNA sequences termed Polycomb Response Elements (PREs) and Trithorax Response Elements (TREs) to which it recruits PRC1, PRC2 and trxG complexes to PTMs on various histone tails thereby altering gene transcription(Decoville et al., 2001; Déjardin et al., 2005;

Fujioka et al., 2008; Lanzuolo and Orlando, 2012). Although HMGB proteins as yet have no discernible sequence specificity in mammals it has been shown that HMGB2 binds nucleolin and Ying-Yang 1 (YY1) to silence 3.3 kilobase tandem repeat sequences termed D4Z4 – with facioscapulohumeral muscular dystrophy (FSHD) patients demonstrating deletions in these tandem repeat sequences and subsequent derepression of chromosome 4q35 genes (Gabellini et al., 2002). YY1 *Drosophila* homolog Pho is known to bind to Dsp1 to enable the recruitment of PcG and trxG complexes to chromatin (Atchison, 2014; Basu et al., 2013), which points to the mammalian Dsp1 homolog HMGB2 as being a potentially important epigenetic player in the control/recruitment of PcG and/or trxG chromatin modifying complexes.

Chromatin Remodeling in the Brain

The epigenome undergoes substantial modification during embryonic as well as postnatal brain development in mammals (Ma et al., 2010). Changes ranging from DNA methylation to various histone modifications imbue the underlying genetic code with enhanced variability, which is critical from an evolutionary perspective to enhance organismal fitness (Gabriel Gonzales-Roybal, 2013) (Hirabayashi and Gotoh, 2010). Fate restriction during CNS development is essential to generating the vast array of specific cell types important to the proper functioning of neural circuits. One of the central ways in which cells achieve fate restriction is through the epigenetic modification of gene expression. CpG dinucleotides serve as substrates for methyl groups, which can be added and/or removed by DNA methyltransferases (DNMTs) and demethylases respectively. Although most genes in embryonic stem cells (ESCs) are highly methylated, they become actively demethylated through the process of fate restriction (Hirabayashi and Gotoh,

2010). Which specific proteins and/or protein complexes act to demethylate DNA is still hotly debated, with only the potential intermediate steps of the pathway elucidated so far in mature post-mitotic neurons (e.g. 5-hydroxymethylation 5hmC) (Szulwach et al., 2011). 5hmC occurs primarily at CpG sites within the DNA double helix, and is marooned on CpG islands over the course of active demethylation – with these islands, as identified by bi-sulfite sequencing, serving as regulatory hubs within chromatin (Mellén et al., 2012; Sun et al., 2014).

Another major epigenetic contributor to chromatin dynamics is the post-translational (PTM) modifications of histones. The histone octamer containing two copies each of histone H3, H2A, H2B and H4 makes up the core of the nucleosomal structure around which 147 base pairs of DNA are wound (Shechter et al., 2007). Core histone proteins are subject to many PTMs including (but not limited to) phosphorylation, acetylation, methylation and SUMOylation (Shechter et al., 2007).

A number of molecular players participate at the epigenetic level during neural development, especially in the transition from the neurogenic phase to the astrocytic/gliogenic phase (Hirabayashi and Gotoh, 2010). Polycomb repressive complexes (PRCs) are endowed with the capacity to read and modify the methylation status of lysine 27 on histone H3 – which when present as a trimethylation mark shuts down gene transcription at specific loci (Hirabayashi and Gotoh, 2010). PRC1 and PRC2 are the two primary polycomb chromatin modifying complexes containing proteins such as Ezh2, EED, Suz12 and Bmi1 which form the core subunits of this repressive machinery (Figure I-2A+B)(Lanzuolo and Orlando, 2012; Sparmann et al., 2013a). It has been demonstrated that cell fate decisions during the progression from SVZ neurogenesis to

astrogliogenesis can be dictated by PRC2, whereby the enzymatic activity of Ezh2 and the presence of the other core components maintains a transcriptional block on astrocytic genes such as GFAP – however releasing such a block early with various perturbations leads to early-onset astrogliogenesis (Sparmann et al., 2013a). There are however some conflicting findings regarding a role for PRC2 in the neurogenic/gliogenic fate transition – with another group showing that knockdown of EED is responsible for a prolonged neurogenic phase (Hirabayashi et al., 2009a). An emerging role for such chromatin complexes has also recently been postulated for neurodevelopmental disorders such as autism and schizophrenia (Ho and Crabtree, 2010).

Stroke and Its Animal Models

Stroke is among the leading causes of death and disability in the developed world (Mozaffarian et al., 2015a; 2015b). In the period from 2009-2012 6.6 million Americans older than twenty years of age experienced an episode of cerebral ischemia, which amounts to 2.6% prevalence overall in the general population (NHANES, NHLBI) (Mozaffarian et al., 2015a; 2015b). On average every 40 seconds an individual in the US will have a stroke, and every 4 minutes one of these individuals will lose their life – accounting for 128,932 deaths in 2011 (NHANES, NHLBI) (Mozaffarian et al., 2015b). Although stroke deaths have been in decline over the past 15 years it is essential to continually innovate in the area of healthy brain tissue preserving therapies (Mozaffarian et al., 2015b). The four primary stroke types are as follows: ischemic stroke, sub-arachnoid hemorrhage (SAH) and intra-cerebral hemorrhage (ICH), and transient ischemic attack (TIA) (Carrera et al., 2012) Ischemic stroke is the prevalent type (~87%) (Mozaffarian et al., 2015b). In this most common iteration, a thrombus within the CNS or

in the periphery is dislodged from a vessel wall and transiently or permanently occludes blood flow in a downstream vascular narrowing – very commonly middle cerebral artery territory in the cerebral cortex (Carrera et al., 2012). The thalamus, a three centimeter ovoid structure rostral to the brainstem in the human brain is also a prominent location of ischemic infarcts (Carrera et al., 2012). Although the thalamus is a relatively small structure, due to its role as a relay between the brain stem and cerebral cortex and between different cortical regions, small lacunar infarcts tend to have big ramifications behaviorally (Carrera et al., 2012). Thalamic infarcts can manifest as purely sensation robbing phenomena, perturbing projections to somatosensory cortices – however ataxias and various movement disturbances can also be present implicating defects in intracortical communication (Carrera et al., 2012). There are a number of prominent animal models of stroke ranging from transient middle cerebral artery occlusion (tMCAo) to photothrombosis, to focal injections of the vasoconstrictive peptide Endothelin 1 (ET-1) (Carmichael, 2005; Sozmen et al., 2012). tMCAo is has traditionally been the most commonly used model given its close mechanistic ties with underlying stroke etiology. During tMCAo a small bore filament is threaded up the internal carotid artery until a resistance can be felt, indicating that it has reached its final position at the ipsilateral entrance to the MCA (Ansari et al., 2011). Following an hour long blockade of the MCA the filament is retrieved and local reperfusion occurs, mimicking the vast majority of human cerebral infarcts (Ansari et al., 2011; Carmichael, 2005). While tMCAo is an effective model of stroke, high mortality rates are associated with the surgical procedure (~10-20%), and it is difficult to accurately predict the size/location of the infarct. For this reason our laboratory has been establishing a focal model of thalamic ischemia in mice

utilizing injections of ET-1 (Wang et al., 2007). Overall there are a number of different animal models of stroke providing a range of benefits depending on the experimental question.

Neurogenesis and Stroke

Cerebral ischemia can stimulate cell turnover and endogenous neurogenesis as well as gliogenesis in the mammalian CNS (Jin et al., 2006; Niv et al., 2012; Ohab and Carmichael, 2008). The ischemic penumbra post-stroke in the human brain includes Ki67+ cycling cells which stain positive for the neuroblast marker Dcx – indicating that parenchymal neurogenesis may be present (Jin et al., 2006). In the mouse brain, tMCAo induces SVZ-born neural progenitors to aberrantly migrate into the post-stroke striatum and, in small numbers, differentiate into functional spiny projection neurons – all the while maintaining the specific genetic profile of OB interneurons (the OB is the intended target for migrating SVZ progenitors under non-pathological conditions) (Kreuzberg et al., 2010; Yamashita and Ninomiya, 2006; Zhang et al., 2007). The recent discovery of putative NSCs within other circumventricular areas of the CNS warrants inquiring into whether progenitors housed along, for example the 3rd ventricle neurogenic niche, actively migrate towards ischemic lesions (Bennett et al., 2009; Haan et al., 2013; Robins et al., 2013a; Rojczyk-Gołębiewska et al., 2014).

Thesis Work

The overall goals of my doctoral work are to uncover the biological basis of how HMGB2 functions in perinatal and adult neurogenesis and whether this immune modulator also has a role in post-stroke CNS responses.

A

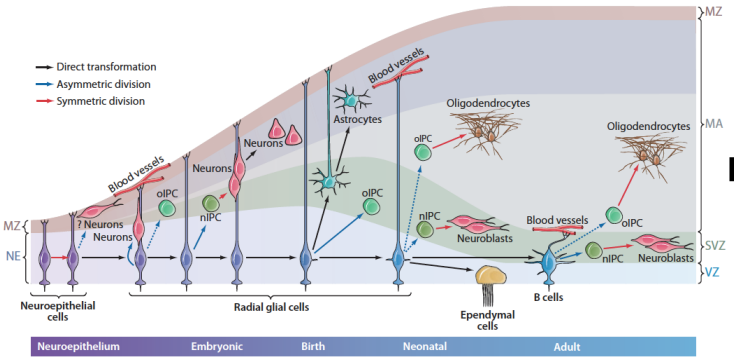
Direct transformation
Asymmetric division
Symmetric division
MZ
MA
SVZ
VZ
NE
Blood vessels
Neurons
Astrocytes
Oligodendrocytes
oIPC
nIPC
? Neurons
Neuroblasts
B cells
Ependymal cells
Neuroepithelial cells
Radial glial cells
Neuroepithelium
Embryonic
Birth
Neonatal
Adult

B

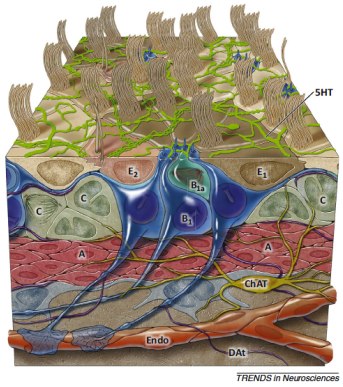
5HT
ChAT
Endo
DAt
TRENDS in Neurosciences

Figure I-1: Embryonic and postnatal development of the VZ/SVZ. (A) Timecourse of the organization and morphological development of embryonic VZ/SVZ as well as the reorganization of the adult SVZ niche. **(B)** 3D depiction of the organization of the adult SVZ niche including the ependymal cells, as well as NSCs and their progeny.

A

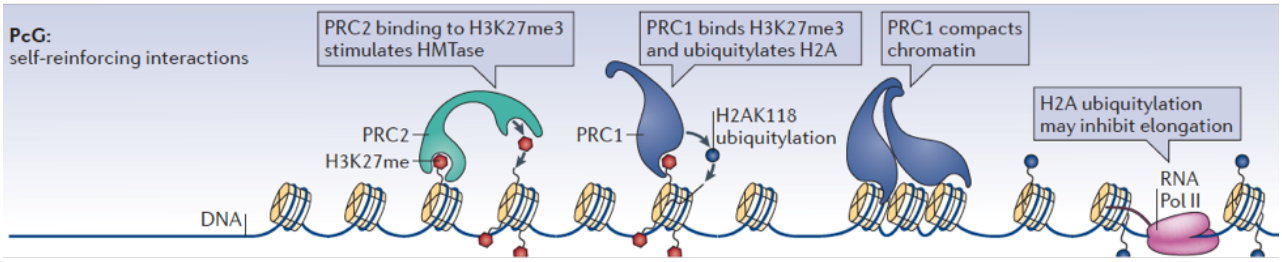

B

PRC1	
Subunit	Molecular function
Pc (CBX)	Chromodomain binds H3K27me3
Psc (BMI1 and MEL18)	Binds DNA and compacts chromatin
Ph (PH)	SAM domain self-associates
Sce (RING1A and RING1B)	Ubiquitylates H2AK118 (K119 in vertebrates), compacts chromatin

PRC2	
Subunit	Molecular function
E(z) (EZH2)	SET domain methylates H3K27
Su(z)12 (SUZ12)	Enhances E(z) HMTase activity
Esc (EED)	Enhances E(z) HMTase activity and binds H3K27me3
Nurf55 (RbAp46 and RbAp48)	Binds histones and SU(z)12

Figure I-2: Cartoon demonstrating the association of PcG PRCs with the chromatin macro-complex. (A) A look at how PRC1 and PRC2 bind to chromatin to catalyze their repressive histone modifications such as H3K27me3 and H2AK119. **(B)** List of PRC1 and PRC2 complex subunits and their respective functions.

Chapter II

Materials and Methods

Animals

All animal experiments were performed with the express written consent and under the guidelines of the Stony Brook University (SBU) Institutional Animal Care and Use Committee (IACUC). HMGB2 null breeding pairs on a C57Bl6 background were obtained from Dr. Lorenza Ronfani (Core Facility for Conditional Mutagenesis, San Raffaele Scientific Institute, Milan 20132, Italy). The HMGB2 transgenic mouse line was created by conventional gene targeting methods (Ronfani et al., 2001). Due to the sterility of the HMGB2 homozygous null males (Ronfani et al., 2001), two breeding strategies were employed for the following experiments: heterozygous females were crossed with heterozygous males or homozygous females crossed with heterozygous males. In instances where Mendelian ratios did not yield adequate numbers of HMGB2 +/+ controls (e.g. the second breeding scheme), age-matched controls were substituted from non-transgenic C57Bl6 breedings.

Adherent Monolayer NPC Cell Culture

Pups ranging in age from postnatal day zero to postnatal day two, obtained from the breedings listed in the animals and genotyping section, were used for all cell culture experiments. Brains were extracted and placed in sterile Hank's buffered salt solution (HBSS) containing 2% glucose. The following brain regions/tissues were dissected away and discarded from each hemisphere: olfactory bulbs, hippocampi, midbrain, cerebellum and meninges. The remaining brain regions, ventricular zone (VZ), subventricular zone (SVZ), striatum and minimal underlying cortex were placed in five milliters of HBSS supplemented with 2% glucose. The tissue was hereafter triturated in one milliliter of complete Neurocult NSC Basal Proliferation Media with the addition of 20ng/mL of

recombinant human epidermal growth factor (rh EGF), 10ng/mL recombinant human basic fibroblast growth factor (rh bFGF), 0.2% heparin and 5% penicillin/streptomycin. Following trituration with a p1000 pipette, the tissue suspension was spun down at 1500 revolutions per minute (RPMs) in a tabletop centrifuge at room temperature. The subsequent tissue pellet was resuspended in 200µl of complete Neurocult NSC Basal Proliferation Media with the addition of 20ng/mL of recombinant human epidermal growth factor (rh EGF), 10ng/mL recombinant human basic fibroblast growth factor (rh bFGF), 0.2% heparin and 5% penicillin/streptomycin. A p200 pipette was set to 180µl and the tissue was further broken up until a uniform cell suspension was achieved. The cell suspension was passed through a 40um nylon mesh cell strainer and plated in 6-well plates precoated with 100ug/mL poly-D-lysine (PDL – 1 hour), and 10ug/mL laminin (4 hours) in a tissue culture incubator at 37 degrees Celsius. Following approximately two to three days of proliferative growth the cells were replated in precoated 60mm tissue culture plates in complete Neurocult Differentiation medium containing supplements and 5% penicillin/streptomycin.

qRT-PCR Arrays

The following Qiagen RT^2 Profiler 84-gene arrays were utilized: Mouse Polycomb & Trithorax Complexes (PAMM-506Z), Mouse Neurogenesis (PAMM-404Z). The arrays were loaded with cDNA reverse transcribed from RNA which was obtained from 24 hour differentiation cultures of HMGB2+/+ and HMGB2-/- NSPCs. An Applied Biosystems StepOnePlus qRT-PCR machine served as the PCR platform. Data were analyzed initially on the Qiagen web-based analysis software followed by Microsoft Excel.

Quantitative real-time PCR

Total RNA was obtained from differentiating HMGB2+/+ and HMGB2-/- NSPCs at days one and three. RNAbee (Ambsbio) was used for RNA extraction followed by purification via the Qiagen RNeasy Mini Kit (74104). Subsequently cDNA was reverse transcribed using the High-Capacity cDNA Reverse Transcription Kit (Life Technologies - 4368814). All primer sequences are listed in Table 1.

Reverse Transcription PCR

Total RNA was extracted from a 1mm slice of thalamic tissue cut on a coronal mouse brain matrix. RNA was converted to cDNA using the High-Capacity cDNA Reverse Transcription Kit (Life Technologies - 4368814). The following primer pairs were used in the experiment, with PCR products being run out on a 1% agarose gel:

ET-1

F 5'-ACT TCT GCC ACC TGG GCA TC-3'

R 5'-ACT TTG GGC CCT GAG TTC TT-3'

ET_AR

F 5'-ACG GTC TTG AAC CTC TGT GC -3'

R 5'-AGC CAC CAG TCC TTC ACA TC -3'

ET_BR

F 5'-AGC TGG TGC CCT TCA TAC AG-3'

R 5'-GGG GCT TTC CTT TGT AGT CC-3'

Edothelin-1 Thalamic Stroke

In our current studies of ET-1 induced ischemia we largely utilized a protocol from (Tennant and Jones, 2009). The lyophilized ET-1 peptide was purchased from Calbiochem (Human & Porcine 05-23-3800) and reconstituted at 0.5ug/µl in sterile saline. Acetic acid was added to a concentration 0.01% to aid in bringing ET-1 fully into solution, and the working stock was stored in 50µl aliquots. Once removed from -20°C, each aliquot was used only for surgical experiments within a 12 hour period, and never refrozen for further stereotaxic injections. Throughout the surgical day the ET-1 vial was kept constantly on ice and vortexed before every injection. A 5µl Hamilton syringe was used to deliver 2µl (1µg ET-1) to the following stereotaxic coordinates (relative to bregma) in the ventromedial thalamus: anterior/posterior -1.79mm, medial/lateral +/- .7mm, dorsal/ventral -4.2mm. Saline (0.9%) was delivered to the identical coordinates as a control.

SVZ Wholemount Preparation

Protocol largely obtained from (Mirzadeh et al., 2010), employing eight to ten week old HMGB2+/+ and HMGB2-/- mice. Animals were euthanized with avertin overdose followed by cervical dislocation, and finally decapitation. The subsequent dissection of the SVZ wholemount completed in sterile ice-cold Hank's balanced salt solution (HBSS) using a Sharpoint 22.5° microsurgical stab knife (Mirzadeh et al., 2010).

Shotgun Proteomics

Proteomic analysis of SVZ wholemount tissue

Sample Preparation:

Samples for proteomic analysis were derived from SVZ wholemount tissue dissected out from HMGB2+/+ and HMGB2-/- mice, and were concentrated in Amicon Ultra-15, UltraCel 3k columns (ThermoFisher) to acquire appropriate concentrations for digestion. Protein concentration was determined by the EZQ protein quantification assay (Invitrogen, CA) according to the manufacturer suggested protocol.

Trypsin Digestion:

50 μg of proteins from the conditioned media were diluted in 50 mM NH4HCO3 solution for trypsin digestion. Trypsin was added to each sample at a ratio of 1:30 enzyme/protein along with 2 mM CaCl2 and incubated for 16 hours at 37°C. Following digestion, all reactions were acidified with 90% formic acid (2% final) to stop proteolysis. Then, samples were centrifuged for 30 minutes at 14,000 RPMs to remove insoluble material. The soluble peptide mixtures were collected for LC-MS/MS analysis.

Multidimensional chromatography and tandem mass spectrometry:

Peptide mixtures were pressure-loaded onto a 250 μm inner diameter (i.d.) fused-silica capillary packed first with 3 cm of 5 μm strong cation exchange material (Partisphere SCX, Whatman), followed by 3 cm of 10 μm C18 reverse phase (RP) particles (Aqua, Phenomenex, CA). Loaded and washed microcapillaries were connected *via* a 2 μm filtered union (UpChurch Scientific) to a 100 μm i.d. column, which had been pulled to a 5 μm i.d. tip using a P-2000 CO2 laser puller (Sutter Instruments), then packed with 13 cm of 3 μm C18 reverse phase (RP) particles (Aqua, Phenomenex, CA) and equilibrated in 5% acetonitrile, 0.1% formic acid (Buffer A). This split-column was then installed in-line with a NanoLC Eskigent HPLC pump. The flow rate of channel 2 was set at 300 nl/min for the organic gradient. The flow rate of channel 1 was set to 0.5 μl/min for

the salt pulse. Fully automated 11-step chromatography runs were carried out. Three different elution buffers were used: 5% acetonitrile, 0.1% formic acid (Buffer A); 98% acetonitrile, 0.1% formic acid (Buffer B); and 0.5 M ammonium acetate, 5% acetonitrile, 0.1% formic acid (Buffer C). In such sequences of chromatographic events, peptides are sequentially eluted from the SCX resin to the RP resin by increasing salt steps (increase in Buffer C concentration), followed by organic 28 gradients (increase in Buffer B concentration). The last chromatography step consists in a high salt wash with 100% Buffer C followed by acetonitrile gradient. The application of a 2.5 kV distal voltage electrosprayed the eluting peptides directly into a LTQ-Orbitrap XL mass spectrometer equipped with a nano-LC electrospray ionization source (ThermoFinnigan). Full MS spectra were recorded on the peptides over a 400 to 2000 m/z range by the Orbitrap, followed by five tandem mass (MS/MS) events sequentially generated by LTQ in a data-dependent manner on the first, second, third, and fourth most intense ions selected from the full MS spectrum (at 35% collision energy). Mass spectrometer scan functions and HPLC solvent gradients were controlled by the Xcalibur data system (ThermoFinnigan, San Jose, CA).

Database search and interpretation of MS/MS datasets:

Tandem mass spectra were extracted from raw files, and a binary classifier - previously trained on a manually validated data set - was used to remove the low quality MS/MS spectra. The remaining spectra were searched against a UniProt mouse protein database released on May, 3rd 2011 (2004a) and 124 common contaminant proteins. To calculate confidence levels and false positive rates, we used a decoy database containing the reverse sequences of the UniProt protein database appended to the target database

(Chen et al., 2008; McClatchy et al., 2011; 2007a), and the SEQUEST algorithm to find the best matching sequences from the combined database. SEQUEST searches were done through the Integrated Proteomics Pipeline (IP2, Integrated Proteomics Inc., CA) on Intel Xeon X5450 X/3.0 PROC processor clusters running under the Linux operating system. The peptide mass search tolerance was set to 50 ppm. No differential 29 modifications were considered. A fully tryptic status was imposed on the database search. The validity of peptide/spectrum matches was assessed in DTASelect2 (1994)using SEQUEST-defined parameters, the cross-correlation score (XCorr) and normalized difference in cross-correlation scores (DeltaCN). The search results were grouped by charge state (+1, +2, and +3) and tryptic status (fully tryptic, half-tryptic, and non-tryptic), resulting in 9 distinct sub-groups. In each one of the sub-groups, the distribution of XCorr and DeltaCN values for (a) direct and (b) decoy database hits was obtained, and the two subsets were separated by quadratic discriminant analysis. Outlier points in the two distributions (for example, matches with very low Xcorr but very high DeltaCN) were discarded. Full separation of the direct and decoy subsets is not generally possible; therefore, the discriminant score was set such that a false discovery rate of 1% was determined based on the number of accepted decoy database peptides. This procedure was independently performed on each data subset, resulting in a false positive rate independent of tryptic status or charge state. In addition, a minimum sequence length of 7 amino acid residues was required, and each protein on the final list was supported by at least two independent peptide identifications unless specified. These additional requirements – especially the latter - resulted in the elimination of most decoy database and false positive hits, as these tended to be overwhelmingly present as proteins identified by single peptide matches.

After this last filtering step, the false discovery rate was reduced to below 1%. Relative fold difference between samples was derived using the spectral counting method (2004b; 2008).

STRING Proteomics Analysis and Modeling

Protein-protein interaction analysis interface integrates data from two primary sources: scientific texts, homologs in other species (Franceschini et al., 2013). When protein candidates are used as input for the online tool a map of protein interactions is created based on those primary sources, detailing whether an interaction exists between proteins and the statistical strength of that interaction given the readout from the STRING algorithm (Franceschini et al., 2013). In our analyses we included only those proteomic hits that display interactions, with the line thickness between protein nodes representing the inferred strength of any one particular interaction.

Western Blots

Histones were obtained from cell culture lysates at various timepoints primarily employing the method described in (Shechter et al., 2007). Briefly, cells were centrifuged in a room temperature table top centrifuge at 300g and the pellets cleaned with 10ml of sterile HBSS, which was also subsequently spun out. The pellets were resuspended in one milliliter of hypotonic lysis buffer (10 mM Tris–Cl pH 8.0, 1 mM KCl, 1.5 mM MgCl2, 1 mM DTT, protease and phosphatase inhibitors) (Shechter et al., 2007) and rotated at 4 degrees Celsius for 30 minutes. Following this step a nuclear pellet was obtained by spinning the hypotonically dissociated cells at 4 degrees Celsius, 10,000g for 10 minutes. Following this step the NSPC nuclear pellet was resuspended in 400µl of H_2SO_4 and rotated overnight at 4 degrees Celsius. Nuclear debris were removed by spinning the acid

extracted preparation at 16,000g for 10 minutes. 132µl of trichloroacetic acid (TCA) was added to the supernatant to a 33% final concentration to precipitate the histones. A final spin step was used to pellet the purified histones and two subsequent washes with ice-cold acetone cleared away any remaining acid. The histones were dried for 20 minutes at room temperature and resuspended in 100µl of ddH_2O. Concentrations of purified histone proteins were obtained via ImageJ densitometry measurements following 15% SDS-PAGE and subsequent coomassie staining. Western blots utilized the aforementioned percentage gels followed by transfer to PVDF membranes. The following antibodies were used to probe for specific histone modifications: 1.) Tri-Methyl-Histone H3 (Lys27), Rabbit monoclonal (mAb) from Cell Signaling (#9733) at a concentration of 1:1000, 2.) Di/Tri-Methyl-Histone H3 (Lys9), Mouse IgG1 mAb from Cell Signaling (#5327) at a concentration of 1:2000, 3.) Tri-Methyl-Histone H3 (Lys4), Rabbit mAb from Cell Signaling (#9751) at a concentration of 1:1000, 4.) Anti-Histone H3 Rabbit polyclonal from Abcam (ab1791) at a concentration of 1:2500.

Immunohistochemistry

Cresyl violet immunohistochemistry following ET-1 induced VM thalamic stroke was performed on 50µm paraformaldehyde (PFA) perfused sections cut on a cryostat and dried overnight in the dark, at room temperature (RT). All steps are performed at RT with no agitation: 15 minutes 95% Ethanol (EtOH), 1 minute 70% EtOH, 1 minute 50% EtOH, 2 minutes dH_2O, 1 minute dH_2O, 5 minutes Cresyl Violet (pre-warmed at 45°C), 2 minutes dH_2O, 1 minute dH_2O, 1 minute 70% EtOH, 1 minute 95% EtOH, 30 seconds differentiation: 98ml 95% EtOH+2ml acetic acid, 1 minute 100% EtOH, 5 minutes xylol and finally mount with vectamount (Bacigaluppi et al., 2009). Fluoro-Jade B staining

following ET-1 induced thalamic ischemia in the VM thalamus was conducted by making use of the following protocol (2005), using the contralateral VM thalamus as the control.

Immunofluorescence

Cell Culture

HMGB2+/+ and HMGB2-/- NSPCs were differentiated for three or seven days in 8-well chamber slides (Fisher-Mediatech 177445) precoated with 100ug/mL poly-D-lysine (PDL – 1 hour), and 10ug/mL laminin (4 hours) in a tissue culture incubator at 37 degrees Celsius. Following 4% PFA fixation, individual chambers were blocked for one hour with phosphate buffered saline (PBS) containing 5% normal goat serum, 1% bovine serum albumin (BSA), and 0.3% Triton-X100. Antibody solution was made up of PBS containing 1% BSA, and 0.03% Triton-X100. All antibodies used are listed in Table 2.

Tissue Sections

PFA perfused tissue sections were blocked for one hour with PBS containing 5% normal goat serum, 1% bovine serum albumin, and 0.3% Triton-X100. Antibody solution was made up of PBS containing 1% BSA, and 0.3% Triton-X100. Antibodies used are listed in Table 2.

Fluorescent Image Quantification

All image quantification and analysis was completed in Fiji (2012). Maximum projections of confocal z-stacks were split into single channels, thresholded, and finally a watershed correction was applied to delineate individual cell bodies (2012). Individual particles were analyzed based on specific and consistent size and circularity inputs, and counts were achieved with the Fiji cell counting plug-in. Finally, for all of the figures

which include fluorescent images, ratios were employed as a readout for statistical analysis.

Behavior

Spontaneous freely moving behavior was judged in the home cage of the animal from days two to seven following ET-1 induced VM thalamic ischemia. A one minute video of each animal was recorded on each of those days, as it moved around the cage. Analysis was based on how many times each animal reared up with either its left, right or both paws on the side of the cage. Secondly, the Noldus Catwalk XT system was utilized in analyzing limb biomechanics of multiple treatment groups as mice navigated a glass pathway and were video recorded from underneath (Chen et al., 2014; Chiang et al., 2014). All statistical analysis was completed in the Noldus Catwalk XT software package and GraphPad Prism (2015a).

Statistics

For comparisons between groups of two an unpaired, two-tailed t-test was employed. For multiple comparisons within a group a one-way ANOVA was used followed by either Holm-Sidak multiple comparison post-hoc analysis, or Bonferroni's post-hoc multiple comparisons test. GraphPad Prism and Microsoft Excel were used for all statistical analyses (2015a). A 95% confidence interval is used for all figures indicating initial significance at $p < 0.05$ marked by one *, and greater significance at $p<.01$ marked by two **. Standard error of the mean is the calculation underlying all graph error bars, *n* refers to the number of biological replicates used in each experiment.

Table 1. Primers used in qRT-PCR

Primer name	Sequence (5'-3')	PrimerBank ID
BMI1_F	ATCCCCACTTAATGTGTGTCCT	192203a1
BMI1_R	CTTGCTGGTCTCCAAGTAACG	192203a1
EED_F	ATGCTGTCAGTATTGAGAGTGGC	2088637a1
EED_R	GAGGCTGTTCACACATTTGAAAG	2088637a1
SUZ12_F	TGCCACTAGAAATTCAGAGAGCC	30046920a1
SUZ12_R	TTGTGCAGGTTTAACAGAACCA	30046920a1
CBX3_F	ACTGGACCGTCGTGTAGTGAA	6680860a1
CBX3_R	GCCCCTTGGTTTGTCAGCA	6680860a1

Table 2. Immunofluorescence Antibodies – cells/tissues

Name	Species	Manufacturer	Working Dilution
Tuj1 (β3-Tubulin)	Mouse IgG1	Cell Signaling	1:250
GFAP	Mouse IgG1	Cell Signaling	1:800
CC1	Mouse mAb	Abcam	1:250
Iba1	Rabbit pAb	Waco	1:500
NeuN	Mouse mAb	Millipore	1:500
Cleaved Caspase3	Rabbit IgG	Sigma-Aldrich	1:250

Chapter III

SVZ Proteomics + Validation

Introduction

The SVZ neural stem cell niche is the site of the most copious production of newborn neurons and glial cells in the adult murine CNS. Its characteristic organization can be broken down into a number of constituent parts, including – the ependymal cell niche, the vascular plexus which feeds the SVZ, as well as the actively dividing and quiescent progenitors which make up the core of the niche and give rise to OB interneurons, NG2+ glia, and mature astrocytes which express GFAP (Lim and Alvarez-Buylla, 2014).

The ependymal compartment contains very unique VZ inputs as well as a distinctive architecture, making it critically important in structure and function relationships in adult neurogenesis (Kriegstein and Alvarez-Buylla, 2009; Mirzadeh et al., 2008). The multi-ciliated ependymal cell lineage emerges during the perinatal structural reorganization of the VZ/SVZ (Jacquet et al., 2011; 2009), with the transcription factor FoxJ1 playing a decisive role (Jacquet et al., 2009; 2011). FoxJ1-/- animals demonstrate disrupted differentiation of perinatal ependymal cells and of a small subset of GFAP+ astrocytes in the VZ/SVZ, with concomitant disruption in the stereotypical pinwheels along the lateral walls of the lateral ventricles later in development (Jacquet et al., 2009; Mirzadeh et al., 2008). These pinwheels are essentially clusters of multi-ciliated ependymal cells with an B1 NSC primary cilium contacting the ventricle through the center of the pinwheel, thereby giving quiescent and active NSCs in the SVZ access to soluble CSF signals (Figure III-1A+B)(Mirzadeh et al., 2008) (Lim and Alvarez-Buylla, 2014). In addition, recent work has revealed axonal arbors emanating from distant structures such as the Raphe nucleus and nucleus basalis of Meynert that exert local activity-dependent control

of ependymal layer VZ/SVZ function through serotonergic and cholinergic neuromodulation (Paez-Gonzalez et al., 2014; Tong et al., 2014).

The SVZ vascular plexus represents the other side of the coin, feeding soluble signals from the blood stream such as growth factors and chemokines directly to the neurogenic niche – largely via B1 cell processes/astrocytic end feet (Kokovay et al., 2010; 2012; Shen et al., 2008). It has been demonstrated that dividing neural progenitors and PSA-NCAM+ neuroblasts home to the vasculature which lays in direct apposition to the SVZ niche, where they receive signals important for their survival, maturation and migration (Kokovay et al., 2010; Shen et al., 2008). Stromal-derived factor 1 (SDF1) in quiescent B1 NSCs upregulates epidermal growth factor receptor (EGFR) which leads to the division and migration of these neural progenitors towards the vasculature – seemingly following the gradient established by the chemokine and its receptor CXC chemokine receptor 4 (CXCR4) (Kokovay et al., 2010).

Identifying Novel Intrinsic Proteins Affecting Neurogenesis

The initial goal of pilot studies in our lab some time ago sought to identify novel putative factors demonstrating an impact on embryonic murine neurogenesis. To this end we utilized the neurosphere model of embryonic NSC growth, following timed mating and dissection of E12.5 - E15.5 pups (Abraham et al., 2013a). Upon confirmation that these WT neurospheres expressed embryonic NSC markers such as GFAP and CD133, we performed shotgun proteomics analysis and identified 383 variably expressed proteins at the developmental timepoints mentioned earlier (Abraham et al., 2013a). The high mobility group B (HMGB) protein family, especially HMGB2, were particularly interesting since their levels fluctuated considerably at different embryonic time points as

well as consecutive passages in culture (Abraham et al., 2013a). HMGB2 protein levels more than doubled in E12.5 neurospheres as seen by western blot following eight consecutive passages in cell culture, however as development went on the levels of HMGB2 in proliferating NSCs were downregulated (Abraham et al., 2013a). NSC differentiation especially led to the significant downregulation of both HMGB2 mRNA and protein levels, so much so that by 48 hours following removal of proliferation dependent growth factors from the cell culture medium, HMGB2 protein levels were halved (Abraham et al., 2013a). To fully appreciate the effect HMGB2 was exerting in embryonic NSCs we obtained a germline KO mouse and compared neurosphere growth between the WT mouse and the HMGB2 deficient mouse (Abraham et al., 2013a). It was discovered that the HMGB2 KO mouse grew significantly more neurospheres that measured less than 50 microns in size, and those smaller floating NSC clumps were significantly more proliferative as measured by the levels of BrdU incorporation (Abraham et al., 2013a). Given these changes in the proliferative potential of HMGB2 deficient neurospheres, we ran a differentiation assay and found no differences in the neuron to glial ratio produced from WT and HMGB2 KO NSCs (Abraham et al., 2013a).

As a followup to these studies we wanted to observe whether SVZ neurogenesis specifically was perturbed in the adult HMGB2 null mice. Upon multiple injections of BrdU to mark S phase of the cell cycle and subsequent co-labeling with Ki67, a pan cell cycle marker - we observed greater numbers of adult SVZ stem cells remaining within the cell cycle, as compared with WT (Abraham et al., 2013b). Additionally our studies uncovered greater numbers of GFAP+/Nestin+ NSCs in the SVZ and RMS of HMGB2 deficient mice at ten weeks of age, indicating greater numbers of symmetric divisions of B

stem cells (Abraham et al., 2013b). As I mentioned previously, B cells in the SVZ eventually give rise to intermediate progenitors and finally migrating neuroblasts destined for the OB – and, in fact, we discovered more DCX+ neuroblasts in the HMGB2 KO SVZ and rostral migratory stream (Abraham et al., 2013b). As a final test as to whether the increased numbers of SVZ NSCs and migrating neuroblasts in the HMGB KO mouse lead to downstream changes within the OB, we injected WT and KO mice with BrdU at eight weeks of age and euthanized them two weeks later (Abraham et al., 2013b). Upon staining the tissue obtained from these mice for the BrdU label retaining cells in the OB that also expressed NeuN (a pan-neuronal marker), we discovered modest increases in granule cell layer newborn interneurons in the HMGB deficient mice (Abraham et al., 2013b), leading us to conclude that increased levels of SVZ neurogenesis were having downstream effects on the whole system.

Results

Shotgun Proteomics of Adult NSC Tissue

We reasoned that given the changes seen in HMGB2 during embryonic as well as adult neurogenesis, we may be able to uncover a series of molecular changes via a shotgun proteomics approach in the adult HMGB2-/- CNS – which would provide us with a more mechanistic insight into the HMGB2-/- phenotype. To this end, we dissected out wholemount tissue from the SVZ/lateral ventricle walls of HMGB2+/+ and HMGB2-/- mice at 10 weeks of age, employing a preexisting protocol (Mirzadeh et al., 2010). Following proteomics analysis, MS/MS datasets were partitioned in two principal ways: 1.) Specific protein candidates present in both the HMGB2+/+ and HMGB2-/- SVZ samples, though often in variable abundances, 2.) Proteins present in either HMGB2+/+,

HMGB2-/-, but not both. We uncovered a total of 1983 proteins variably expressed between the two genotypes, with 277 uniquely expressed in the HMGB2+/+ SVZ and 270 in the HMGB2-/- wholemount tissue – with the top 25 candidates overrepresented in each genotype shown here (Figure III-2A+B). A tight Gaussian distribution of WT/KO peaks can be observed in instances when both genotypes express a particular unique protein (Figure III-2C). At 38% enrichment, the membrane fraction accounted for the largest subset of MS/MS hits, with the nuclear fraction containing a majority of putative chromatin binding proteins accounting for just 6% of the total (Figure III-2D). We next utilized the Search Tool for the Retrieval of Interacting Genes/Proteins (STRING) clustering algorithm to assay the physical and/or functional interactions between our MS/MS derived protein candidates (Franceschini et al., 2013). STRING integrates information from a number of sources including - genomic context, (conserved) co-expression analyses and PubMed metadata (Franceschini et al., 2013). We chose to visualize interactions of proteins just within the outer bounds of our Gaussian MS/MS distribution, interspersed between the -5 to -4 bars as well as the 4 to 5 bars within the graphed ratios (Figure III-2C). These two groups represent the instances in which many more MS/MS peaks were uncovered in the WT vs. KO and the KO vs. WT for any one unique protein respectively. Figure III-3 represents physical and/or functional interactions between proteins overrepresented in the WT/KO analysis, with distinct clusters representing ribosomal and mitochondrial functions as well as those of intracellular signaling complexes (Figure III-3+4). The increased thickness of the blue lines connecting hubs indicates more evidence of physical and/or functional affiliation between protein candidates (Franceschini et al., 2013). The proteins overrepresented in the KO/WT

samples mimic the previous figure by skewing towards mitochondrial and ribosomal subunits, however there is also a distinct cluster representing major synaptic and adhesion proteins such as NrCAM, L1cam, and CamKII (Figure III-4).

Validation of Proteomics Dataset

Our lab has previously demonstrated that the neuroblast specific protein DCX was significantly upregulated in the SVZ and rostral migratory stream (RMS) of HMGB2-/- mice (Abraham et al., 2013b). Because neural cell adhesion molecule (NrCAM), a proxy for DCX in the SVZ and RMS, is highly enriched in cluster A (Figure III-4A) we decided to validate its expression level via immunoblot assays. Three distinct alternatively spliced isoforms of NrCAM are expressed in the mouse brain, NrCAM 120, 140 & 180 (Polo-Parada et al., 2004). NrCAM 120 (kD) is a glycosylphosphatidyl-inositol linked isoform (GPI) isoform primarily expressed on glial cell membranes in the CNS, while NrCAM 140 & 180 are expressed pre and post-synaptically, as well as extrasynaptically on excitatory as well as inhibitory neuron pools (Polo-Parada et al., 2004). In 10 week old SVZ wholemount preparations we observed a significant increase in the NrCAM140 isoform as well a trending upregulation of the NrCAM180 isoform (Figure III-5D). Increases in these two particular isoforms within the SVZ have been demonstrated to accompany either an increase in neuroblast production, or a delay in the migration of DCX+/NrCAM+ neuroblasts out of the SVZ niche and towards the OB (Boutin et al., 2009). A recent study from a group at the University of Ottawa (Campbell and Rudnicki, 2013a) revealed that HMGB2 may be critical to stem cell function by interacting with pluripotency factor Oct4, leading to the downregulation of phosphorylated Akt (pAkt). We found reduced levels of Oct4 as well as pAkt in the HMGB-/- SVZ wholemount tissue (Figure III-5A+B). A

concomitant increase in the levels of tumor suppressor protein p21 were also found in the 10 week old HMGB2-null SVZ wholemount tissue (Figure III-5C). These changes may underlie a shift towards differentiation in the adult HMGB2-/- SVZ (Figure III-6A).

Discussion

In this study we provide evidence that the genetic ablation of HMGB2 in the adult murine SVZ leads to distinct changes in the proteome of this critically important neurogenic niche. Previous work from our laboratory has demonstrated clear increases in the numbers of DCX+ neuroblasts and concomitant reduction in Mash1+ intermediate progenitors, indicating that the process of adult NSC differentiation may be perturbed in the HMGB2-/- mouse brain (Abraham et al., 2013b). In addition, this previous publication from our group also demonstrated an increase in the number of interneurons in the GCL of the OB in the HMGB2-/- animal, demonstrating a possible link between a shift in differentiation dynamics of the SVZ and forthcoming changes within the OB newborn neuron population (Abraham et al., 2013b). Given that HMGB2 is a global modulator of chromatin structure it is possible that the changes we are observing are simply an extension of a plethora of other gene expression aberrations leading to changes in protein levels; however other studies have specifically implicated chromatin binding proteins such as HMGA1 & HMGA2 (closely conserved domain structures to HMGB2) in embryonic as well as adult murine neurogenesis (Kishi et al., 2012; Nishino et al., 2008). HMGB2 loss in non-neural tissues has been associated with abandonment of stem cell characteristics, and a general movement towards terminal differentiation – especially in the development and maintenance of chondrocytes and articular cartilage (Taniguchi et al., 2009a; 2009b). In the model we are proposing, HMGB2-/- loss acts to increase the numbers of neuroblasts

in the adult mouse SVZ through the upregulation of specific isoforms of neuronal NrCAM and the tumor suppressor protein p21, and subsequent downregulation of the pluripotency factor Oct4 (Figure III-6).

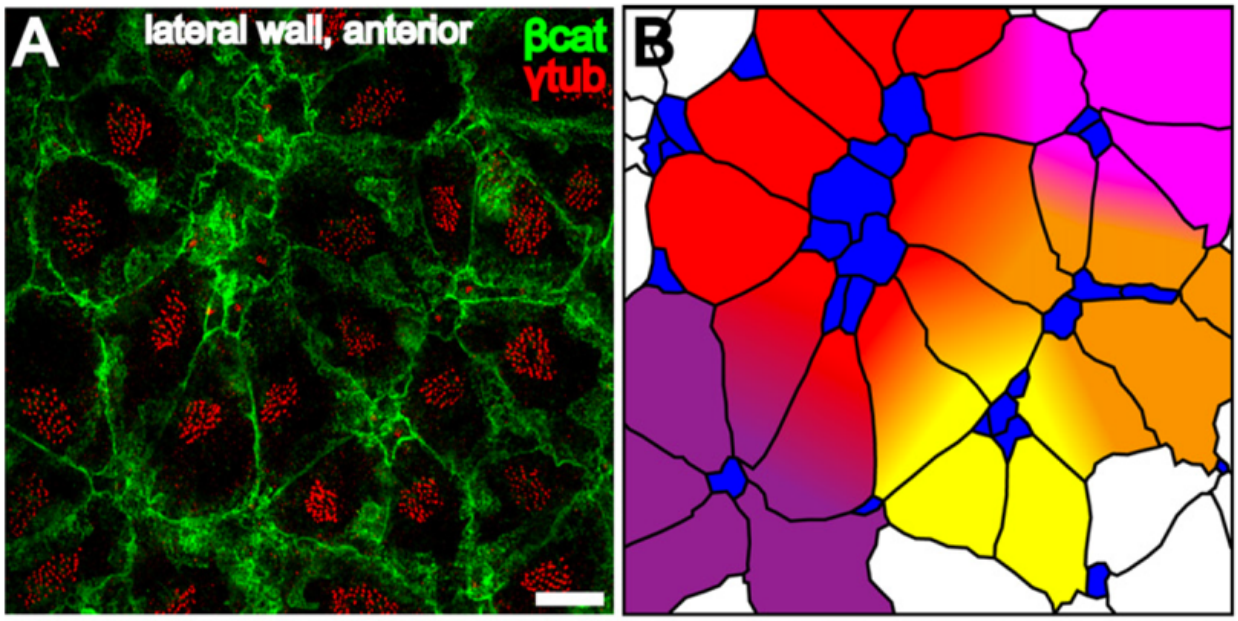
A
lateral wall, anterior
βcat
γtub
B

Figure III-1: En-face depiction of the lateral ventricle wall in the mouse. (A) Beta-catenin and gamma-tubulin staining showing cellular borders between ependymal cell clusters as well their multi-ciliated cell bodies. **(B)** Cartoon depiction of 'pinwheel' organization of lateral ventricle wall, with red ependymal cell groups surrounding NSCs which lie underneath and extend a single primary cilium into the ventricular space.

Top 25 Shared MS/MS Peaks

A

	Accession #	Molecular Weight	WT	KO	▲
N-ethylmaleimide sensitive fusion protein attachment protein beta Napb	A2APW8_MOUSE	34 kDa	10	1	10.0
V-type proton ATPase subunit H Atp6v1h	VATH_MOUSE	56 kDa	9	1	9.0
Electrogenic sodium bicarbonate cotransporter 1 Slc4a4	E9Q8N8_MOUSE	123 kDa	8	1	8.0
Kinesin-1 heavy chain Kif5b	KINH_MOUSE	110 kDa	8	1	8.0
MCG7979 Gm8054	D3YVN8_MOUSE	18 kDa	8	1	8.0
Phenylalanine--tRNA ligase beta subunit Farsb	SYFB_MOUSE	66 kDa	8	1	8.0
Cell division control protein 42 homolog Cdc42	CDC42_MOUSE	21 kDa	14	2	7.0
Aminopeptidase B Rnpep	AMPB_MOUSE	72 kDa	7	1	7.0
Protein Rap1gds1 Rap1gds1	E9Q6Q4_MOUSE	61 kDa	7	1	7.0
Neuronal growth regulator 1 Negr1	A0A4W9_MOUSE	36 kDa	20	3	6.7
Casein kinase II subunit alpha Csnk2a1	CSK21_MOUSE	45 kDa	13	2	6.5
Long-chain-fatty-acid--CoA ligase 6 Acsl6	ACSL6_MOUSE	78 kDa	12	2	6.0
Acetyl-CoA acetyltransferase, cytosolic Acat2	THIC_MOUSE	41 kDa	6	1	6.0
Acylglycerol kinase, mitochondrial Agk	AGK_MOUSE	47 kDa	6	1	6.0
Adaptin ear-binding coat-associated protein 1 Necap1	NECP1_MOUSE	30 kDa	6	1	6.0
Adenylate kinase isoenzyme 4, mitochondrial Ak4	F8WH88_MOUSE	38 kDa	6	1	6.0
Adenylosuccinate synthetase isozyme 1 Adss1l	PURA1_MOUSE	50 kDa	6	1	6.0
Amyloid-like protein 2 Aplp2	APLP2_MOUSE	80 kDa	6	1	6.0
Anion exchange protein 3 Slc4a3	B3A3_MOUSE	135 kDa	6	1	6.0
Atlastin-1 Atl1	ATLA1_MOUSE	63 kDa	6	1	6.0
Breast carcinoma-amplified sequence 1 homolog Bcas1	BCAS1_MOUSE	67 kDa	6	1	6.0
Cysteine desulfurase, mitochondrial Nfs1	NFS1_MOUSE	50 kDa	6	1	6.0
Cytochrome b-c1 complex subunit 8 Uqcrq	QCR8_MOUSE	10 kDa	6	1	6.0
Exocyst complex component 8 Exoc8	EXOC8_MOUSE	81 kDa	6	1	6.0
Galectin-related protein A Lgalsla	LEGLA_MOUSE	19 kDa	6	1	6.0
Heat shock 70 kDa protein 4L Hspa4l	HS74L_MOUSE	94 kDa	6	1	6.0

	Accession #	Molecular Weight	WT	KO	▲
Sulfurtransferase Mpst	Q3UW66_MOUSE	33 kDa	1	3	0.3
Ubiquitin-associated protein 2 Ubap2	A2AMY5_MOUSE	118 kDa	1	3	0.3
WAS/WASL-interacting protein family member 2 Wipf2	WIPF2_MOUSE	46 kDa	1	3	0.3
WD repeat-containing protein 37 Wdr37	WDR37_MOUSE	55 kDa	1	3	0.3
CD166 antigen Alcam	CD166_MOUSE	65 kDa	5	18	0.3
40S ribosomal protein S23 Rps23	Q9CZI5_MOUSE	16 kDa	3	11	0.3
40S ribosomal protein S4, X isoform Rps4x	Q545F8_MOUSE	28 kDa	3	12	0.3
Protein Ppp2r5d Ppp2r5d	Q91V89_MOUSE	69 kDa	2	8	0.3
60S ribosomal protein L11 (Fragment) Rpl11	A2BH06_MOUSE	20 kDa	1	4	0.3
Glutamyl-tRNA(Gln) amidotransferase subunit B, mitochondrial Pet112	GATB_MOUSE	62 kDa	1	4	0.3
Heterogeneous nuclear ribonucleoprotein A/B Hnrnpab	Q20BD0_MOUSE	36 kDa	1	4	0.3
NADH dehydrogenase [ubiquinone] iron-sulfur protein 8, mitochondrial Ndufs8	NDUS8_MOUSE	24 kDa	1	4	0.3
Peptidyl-prolyl cis-trans isomerase FKBP4 Fkbp4	FKBP4_MOUSE	52 kDa	1	4	0.3
Protein FAM171A2 Fam171a2	F1712_MOUSE	87 kDa	1	4	0.3
Spectrin alpha chain, erythrocyte Spta1	SPTA1_MOUSE	280 kDa	1	4	0.3
MCG141483 Ctnbp2	G3X9L7_MOUSE	179 kDa	2	10	0.2
60S ribosomal protein L32 Rpl32	RL32_MOUSE	16 kDa	1	5	0.2
Pyrroline-5-carboxylate reductase 2 Pycr2	P5CR2_MOUSE	34 kDa	1	5	0.2
Profilin-1 Pfn1	PROF1_MOUSE	15 kDa	1	6	0.2
Septin-2 Sept2	SEPT2_MOUSE	42 kDa	1	6	0.2
tRNA-splicing ligase RtcB homolog D10Wsu52e	RTCB_MOUSE	55 kDa	1	6	0.2
ATP synthase subunit delta, mitochondrial Atp5d	ATPD_MOUSE	18 kDa	4	26	0.2
Glutathione peroxidase 1 Gpx1	GPX1_MOUSE	22 kDa	1	8	0.1
MAP/microtubule affinity-regulating kinase 4 Mark4	MARK4_MOUSE	83 kDa	1	8	0.1
Signal-induced proliferation-associated 1-like protein 1 Sipa1l1	SI1L1_MOUSE	197 kDa	1	8	0.1
Coronin-1C Coro1c	COR1C_MOUSE	53 kDa	1	9	0.1

B

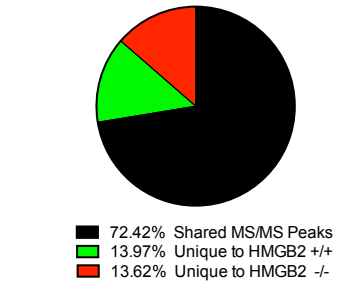

C

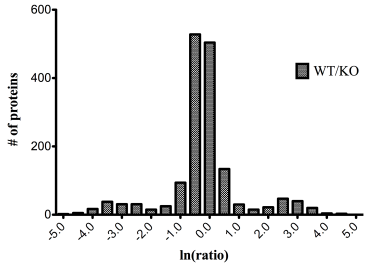

D

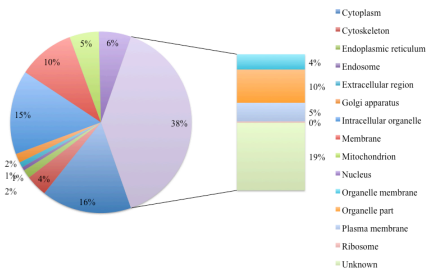

Figure III-2:Shotgun proteomics results and analysis from WT and HMGB2-/- SVZ wholemount tissue. 1983 proteins were identified from total sub-fractionated lysates derived from SVZ wholemount tissue. **(A)** On the left are listed the top 25 candidates overrepresented in the HMGB2+/+ tissue samples and on the right the top 25 candidates overrepresented in the HMGB-/- tissue. They are listed with their NCBI accession numbers as well as their respective molecular weights. **(B)** The pie chart demonstrates the breakdown, by parts of the whole, of peaks shared between the HMGB2+/+ and HMGB2-/- genotypes, and those that are unique to each genotype. **(C)** The bar graph pictured depicts the ratios of MS/MS peaks between the HMGB2+/+ and HMGB2-/- genotyped proteomics samples. **(D)** The pie chart demonstrates the distribution of the identified MS/MS peaks within different subcellular compartments. n=1 per genotype.

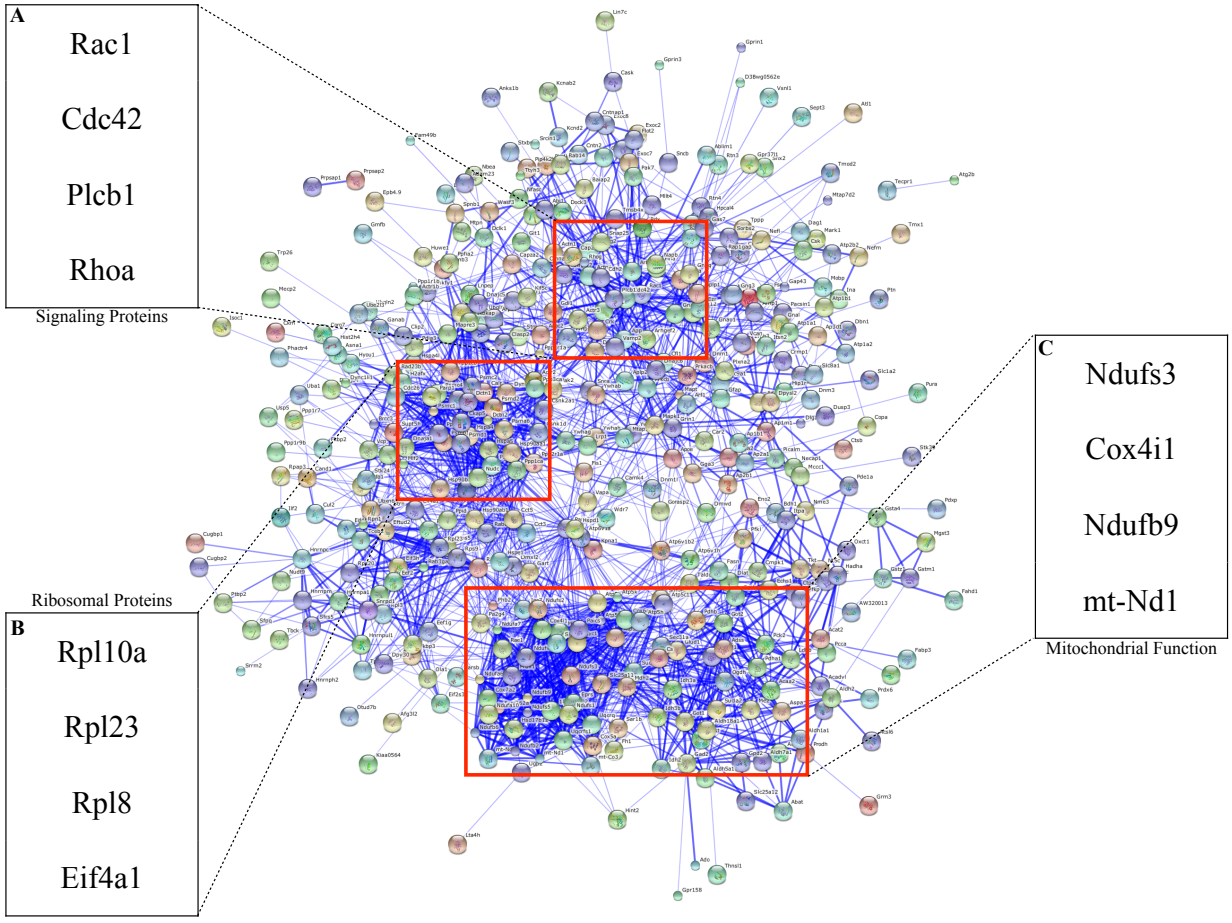
A
Rac1
Cdc42
Plcb1
Rhoa
Signaling Proteins
B
Rpl10a
Rpl23
Rpl8
Eif4a1
Ribosomal Proteins
C
Ndufs3
Cox4i1
Ndufb9
mt-Nd1
Mitochondrial Function

Figure III-3:STRING protein clusters of MS/MS peaks overrepresented in HMGB2+/+ SVZ wholemount tissue. Using the STRING algorithm we demonstrate functionally interconnected protein nodes, with thicker lines representing more robust connections backed up by experimental evidence. **(A)** Signalling protein cluster including proteins such as Rac1, CDC42, RhoA and Plcb1. **(B)** Ribosomal protein cluster including proteins such as Rp110a, Rpl23, Rpl8, and Eif4a1. **(C)** Mitochondrial protein cluster including proteins such as Ndufs3, Cox4i1, Ndufb9 and mt-Nd1.

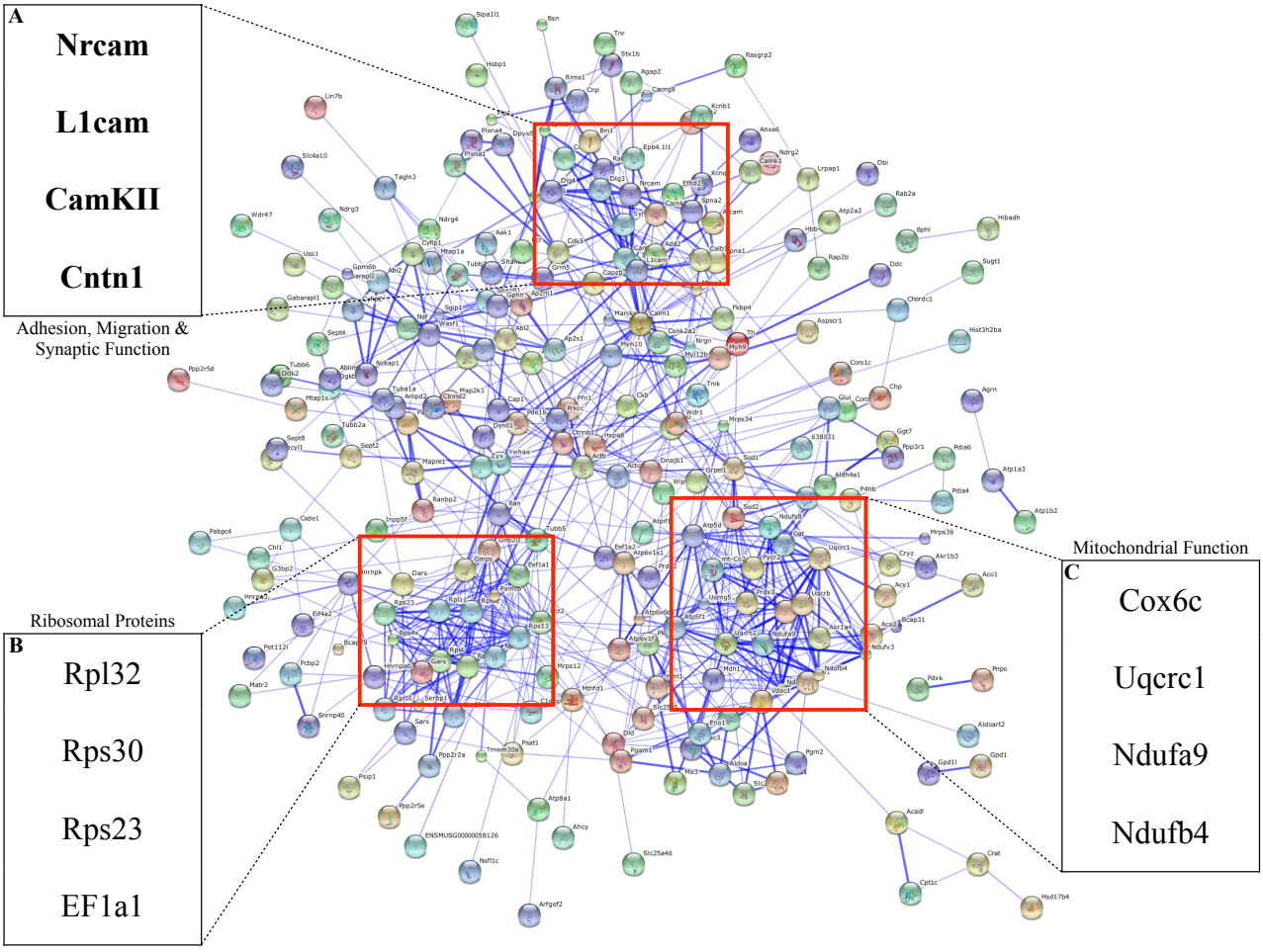
A
Nrcam
L1cam
CamKII
Cntn1
Adhesion, Migration & Synaptic Function
Ribosomal Proteins
B
Rpl32
Rps30
Rps23
EF1a1
Mitochondrial Function
C
Cox6c
Uqcrc1
Ndufa9
Ndufb4

Figure III-4: STRING protein clusters MS/MS peaks overrepresented in HMGB2-/- SVZ wholemount tissue. Using the STRING algorithm we demonstrate functionally interconnected protein nodes, with thicker lines representing more robust connections backed up by experimental evidence. **(A)** Adhesion, migration and synaptic function protein cluster including proteins such as NrCAM, L1cam, CamKII and Cntn1. **(B)** Ribosomal protein cluster including proteins such as Rpl32, Rps30, Rps23 and EF1a1. **(C)** Mitochondrial protein cluster including proteins such as Cox6c, Uqcrc1, Ndufa9 and Ndufb4.

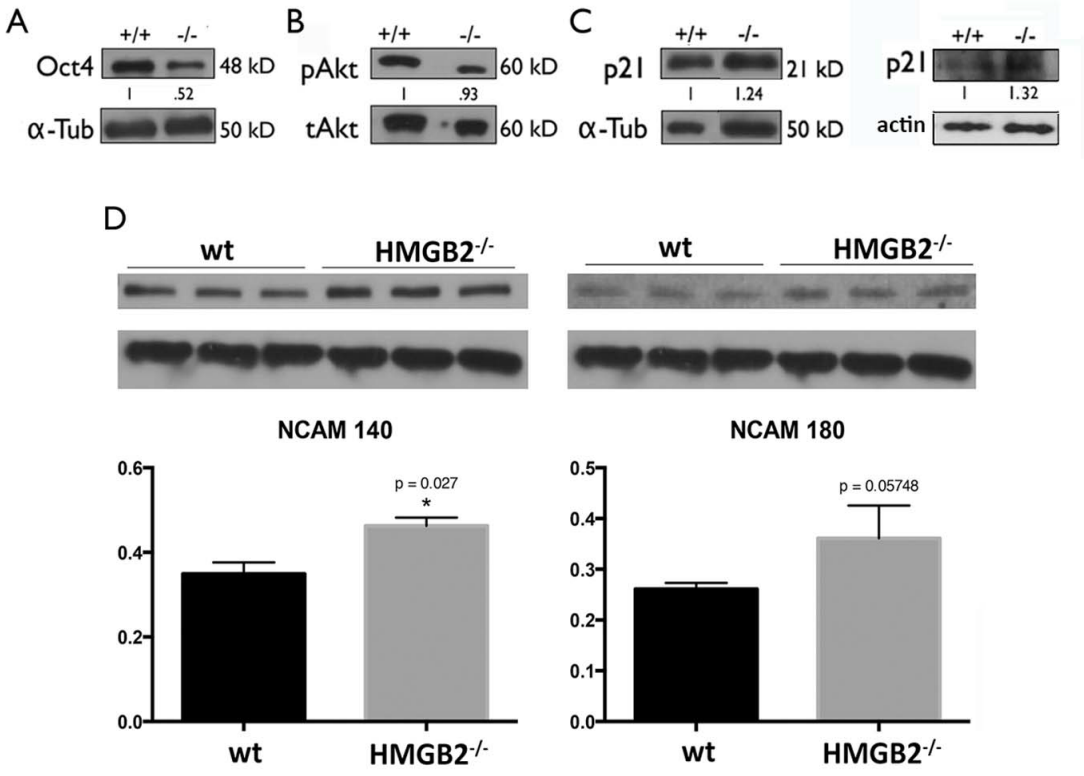
A
+/+
-/-
Oct4
48 kD
1
.52
α-Tub
50 kD
B
+/+
-/-
pAkt
60 kD
1
.93
tAkt
60 kD
C
+/+
-/-
p21
21 kD
1
1.24
α-Tub
50 kD
+/+
-/-
p21
1
1.32
actin
D
wt
HMGB2-/-
wt
HMGB2-/-
NCAM 140
NCAM 180
p = 0.027
*
p = 0.05748
0.6
0.4
0.2
0.0
0.5
0.4
0.3
0.2
0.1
0.0
wt
HMGB2-/-
wt
HMGB2-/-

Figure III-5: Validation of candidates from shotgun proteomics MS/MS data and literature by western blotting analysis. Altered expression of protein candidates from shotgun proteomic MS/MS dataset as well as from associated literature searches in adult HMGB2-/- SVZ wholemount tissue. **(A)** Western blots of the pluripotency factor Oct4 in HMGB2+/+ and HMGB2-/- SVZ wholemount tissue. n=2. **(B)** Western blots of the cytoplasmic signalling molecule pAkt in HMGB2+/+ and HMGB2-/- SVZ wholemount tissue. n=2. **(C)** Western blots of the nuclear tumor suppressor protein p21 in HMGB2+/+ and HMGB2-/- SVZ wholemount tissue. n=2. **(D)** Western blots and quantifications of the protein levels of two NCAM isoforms (140,180) in HMGB2+/+ and HMGB2-/- SVZ wholemount tissue. n=3 per genotype. NCAM140 p=.05748, NCAM180 p=.027*

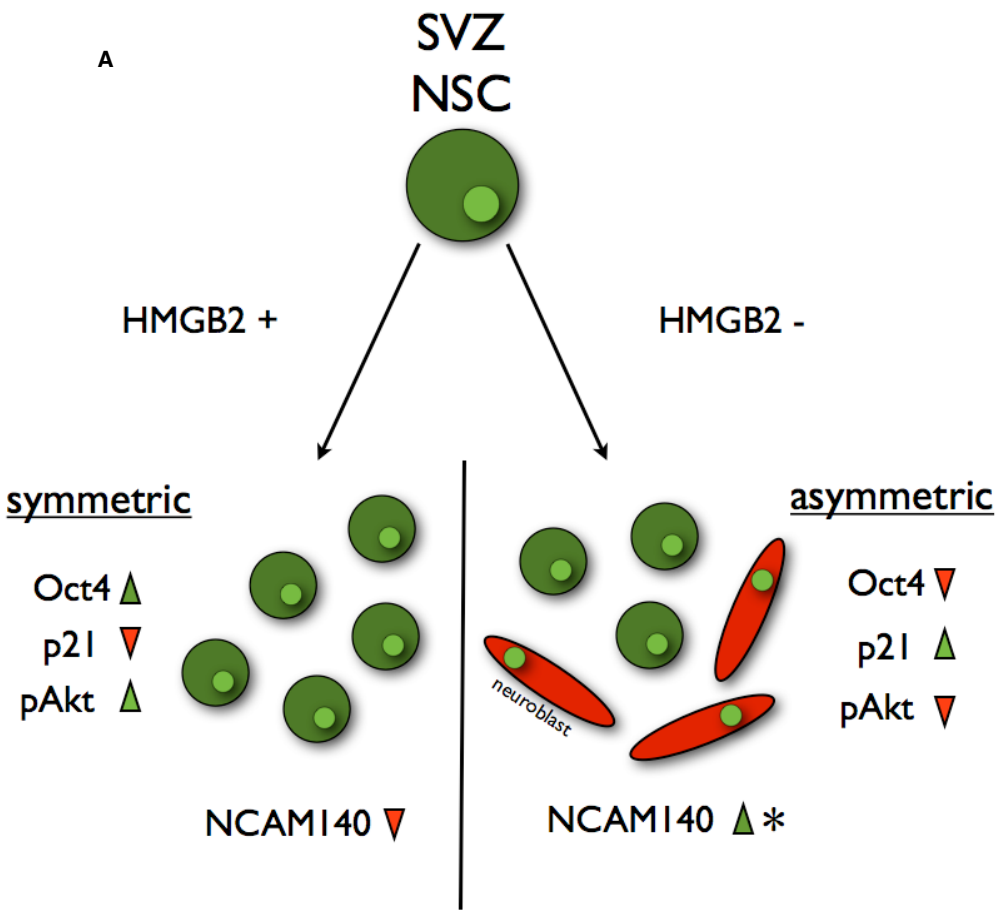
A
SVZ
NSC
HMGB2 +
HMGB2 -
symmetric
asymmetric
Oct4
p21
pAkt
Oct4
p21
pAkt
neuroblast
NCAM140
NCAM140 *

Figure III-6: Proposed model of NSC cell cycle characteristics in the SVZ of WT and HMGB2-/- mice based on shotgun proteomics. Adult HMGB2+/+ SVZ tissue demonstrates greater symmetric NSC divisions, retaining more stem cells within the neurogenic niche which is evidenced through lower levels of NCAM isoforms than the HMGB2-/- SVZ niche which our lab has shown to be accompanied by greater neuroblast birth and migration. Remaining protein differences accompanying either genotype as outlined in Figure III-5 also listed.

Chapter IV

Perinatal Neurogenesis & Gliogenesis

Introduction

The perinatal SVZ stem cell compartment undergoes a number of important changes beginning in late embryogenesis to culminate in the creation of the postnatal SVZ niche. Initially, diverse classes of excitatory cortical pyramidal neurons are created through many rounds of radial glial cell (RGC) division, which occur at the surface of the lateral ventricle approximately between E10 and E17.5 (Kriegstein and Alvarez-Buylla, 2009). These RGCs divide both symmetrically, to amplify their own numbers, as well as asymmetrically to produce daughter cells destined for an intrinsically and temporally specified cortical layer (Huang, 2014; Kriegstein and Alvarez-Buylla, 2009). RGCs are endowed with processes that span the cortical plate, finally attaching to the glia limitans on the pial surface of the brain - and it is precisely these fibers that act as migratory scaffolds for newborn cortical neurons (Huang, 2014). Although these pyramidal cells pattern the cortex in an inside-out fashion starting in early development, their myelination and final integration into discrete neural circuits require the presence of a number of glial cell subpopulations. RGCs begin a developmental program shift around E17.5 to reduce their neurogenic competence and significantly increase production of several glial subclasses (Lim et al., 2009). To achieve this paradigm shift, the RGC population has to modulate the levels of a number of key developmental genes, some of which are instrumental in repressing neuronal differentiation and others critical to increasing glial production (Hirabayashi et al., 2009a). Astrocytes comprise a major group of glial cells produced by RGCs (which are in and of themselves members of a specialized astrocyte subgroup), starting at approximately E17.5 and continuing early postnatally (Covacu et al., 2014; Hwang et al., 2014). The signal transducer and activator of transcription (STAT)

family of transcription factors are instrumental in this ramping up of astrogliogenesis (He et al., 2005). Leukemia inhibitory factor (LIF) induced signalling represents the upstream, extracellular signal, working through Janus kinase (JAK) in the cytosol to induce STAT-mediated transcription of key developmental and proliferative gene sets in early astrocytes (He et al., 2005). Genetic disruptions in this signaling pathway impair astrocyte differentiation and thereby delay comprehensive corticogenesis (He et al., 2005). In totality, a pro-neural basic helix-loop-helix (bHLH) family of transcription factors such as Neurogenin 1/2 (ngn1/2) inhibit STAT 1/3 during the neurogenic phase, through the activation of glial-specific genes (with derepression of this pathway mediated by LIF/JAK signaling) by eventually promoting astrocyte differentiation (He et al., 2005; Sun et al., 2001). NG2+ glia and mature oligodendrocytes are produced during, and following, the astrocyte surge by following much the same genetic schema (Hirabayashi et al., 2009b). In addition to these canonical repressors and inducers of astrogliogenesis, there exists an epigenetic regulatory overlay which is important for gene regulation and homeostasis in the CNS and peripheral tissues. PcG and trxG group proteins act upon this process through epigenetic repression of the *ngn1* locus, which is critical to progression of embryonic neurogenesis. These protein complexes characteristically modify histones through methylation of lysine residues: PcG proteins add the repressive H3K27me3 mark, and trxG members add the permissive H3K4me3 (Aloia et al., 2013).

Results

Knockdown of EED, a critical component of the PcG PRC2, has been demonstrated to result in a delayed neurogenic to gliogenic fate shift in E11.5 NPCs following nine days in-vitro (DIV) (Hirabayashi et al., 2009a). Given the epigenetic role played by homologs of HMGB2 such as DSP1 in *Drosophila*, as well as the cooperative relationship with the mammalian chromatin regulator YY1, we reasoned that the genetic ablation of HMGB2 in NSCs may have an effect on the timecourse and chromatin characteristics of differentiated progeny (Decoville et al., 2001; Déjardin et al., 2005; Gabellini et al., 2002). To investigate this hypothesis monolayer NSC cultures from HMGB2+/+ and HMGB2-/- p0-p2 pups (primary dissections of SVZ) were grown in media promoting cellular proliferation (bFGF & rhEGF) until the plates were ~85% confluent. The cells were replated in 60mm dishes containing differentiation media. Following 24 hours of differentiation we harvested the cells and extracted total RNA for 84-gene analysis via the Qiagen qRT-PCR array system – specifically looking at genes encoding key PcG and trxG subunits as well as those critical to murine neurogenesis (Figures IV-1,2,3,4). Most interestingly, in the PcG and trxG arrays key PRC1 and PRC2 subunits (EED, SUZ12, CBX3, BMI1) were uncovered, which are downregulated in the HMGB2-/- NSCs following 24 hours of differentiation (Figures IV-9+11). Although many other complex macromolecular assemblies have built-in redundancies making the elimination of one component unnoticeable, these key PcG genes encode critical pieces of PRC1 and PRC2 complexes (Margueron and Reinberg, 2011). To further refine our analysis we sought to verify which of these four components was downregulated at days one and three of NSC differentiation by standard qRT-PCR methods (Figures IV-5). Our findings indicate that EED, an important player in the function of PRC1 and PRC2 is downregulated

50% in HMGB2-/- NSCs at day one of differentiation, and 20% at day three of differentiation – and both of these results were statistically significant (Figures IV-5). In the opposite experiment, where we expressed constitutively active Myc-tagged HMGB2 in WT differentiating NSCs, we observed a trend towards the upregulation of EED gene expression (Figures IV-6). EED is a core component of the PRC2 complex and as such functions to recruit PRC1 complexes to H3K27me3 marks on histone tails as well as stabilizing H2A ubiquitin E3 ligase activity (Cao et al., 2014). As such, it is responsible for the coordination of PRC1 and PRC2 activities, which are critical to the repression of specific neuronal and astroglial genes (Cao et al., 2014; Hwang et al., 2014). To test whether global levels of H3K27me3 were altered in HMGB2-/- NSCs we utilized the same monolayer NSC culture system and acid extracted histone proteins, which are labile in sulfuric acid, at days one and three of differentiation (Figures IV-7). H3K27me3 levels remained the same 24 hours following the initiation of differentiation in the HMGB2+/+ and HMGB2-/- NSCs, however they were significantly reduced at day three of differentiation in the HMGB2-/- cultures (Figures IV-7). We also blotted for another repressive histone modification, H3K9me3, which is laid down by a different epigenetic complex not containing EED (Kim and Kim, 2012) and did not observe any changes between HMGB2 WT and KO NSCs at either day of differentiation (Figures IV-8). To examine what was occurring at the cellular level we induced monolayer NSC cultures to differentiate in 8-well chamber slides for three days and seven days, followed by immunostaining with cell-type specific primary antibodies (Figures IV-9). At day three of differentiation significantly more GFAP+ astrocytes were present in the HMGB2-/- wells compared to WT, while neuronal populations characterized by Tuj1 staining, remained at near undetectable levels (Figures IV-9). Interestingly at day seven of

differentiation the ratio of Tuj1+ cells, to GFAP+ and CC1+ (an oligodendrocyte marker), is significantly increased – pointing to a possible effect of HMGB2 loss on the neurogenic to gliogenic fate transition that occurs in perinatal NSCs (Hirabayashi et al., 2009b) (Figures IV-10).

Discussion

In the above described set of experiments we identified a potential role for HMGB2 in the epigenetic dynamics of NSC chromatin. The global, germline loss of the HMGB2 gene and hence the chromatin architectural protein it encodes contributes to a significant reduction in the expression of the vital PcG gene EED, with concomitant reduction in total H3K27me3 levels in NSC histone lysates. These specific genetic changes in the HMGB2-/- NSC population may be linked to altered fate transitions we observe in p0-p2 murine NSCs when the proliferating cells are allowed to differentiate into three principal CNS cell types: neurons, astrocytes and oligodendrocytes. In the *Drosophila* model system DSP1 (HMGB2 homolog) is critical for recruitment of PcG complexes to specific PRE sites within chromatin. While HMGB2 may also have a similar role to play in mammalian systems, we have found an upstream regulatory role in the control of gene expression for those specific genes encoding PcG subunits (Déjardin et al., 2005). Although our analysis of chromatin modifications included all gene loci (total lysates), EED has been shown to interact with the promoters of specific pro-neuronal and pro-glial genes, inhibiting the expression of their gene products at specific developmental timepoints(Egan et al., 2013a; Hu et al., 2012; Jobe et al., 2012).

A

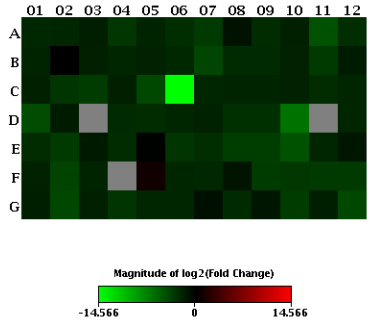

Layout	01	02	03	04	05	06	07	08	09	10	11	12
A	Ache **-4.95** OKAY	Adora1 **-4.38** OKAY	Adora2a **-3.16** OKAY	Alk **-8.53** A	Apbb1 **-4.03** OKAY	Apoe **-6.12** OKAY	App **-9.66** OKAY	Artn **-2.12** OKAY	Ascl1 **-5.83** OKAY	Bcl2 **-3.56** OKAY	Bdnf **-25.43** A	Bmp2 **-6.02** A
B	Bmp4 **-4.31** OKAY	Bmp8b **-1.00** B	Cdk5r1 **-3.66** OKAY	Cdk5rap2 **-4.42** A	Chrm2 **-3.84** A	Creb1 **-4.84** OKAY	Cxcl1 **-16.49** A	Dcx **-5.17** OKAY	Dlg4 **-5.42** OKAY	Dll1 **-3.71** OKAY	Drd2 **-10.18** A	Dvl3 **-3.04** OKAY
C	Efnb1 **-3.51** OKAY	Egf **-7.54** B	Ep300 **-10.53** OKAY	Erbb2 **-3.42** OKAY	Fgf2 **-17.18** A	Flna **-24261.15** A	Gdnf **-4.43** A	Gpi1 **-4.31** OKAY	Grin1 **-4.09** OKAY	Hdac4 **-3.82** OKAY	Hes1 **-5.53** OKAY	Hey1 **-4.66** OKAY
D	Hey2 **-20.93** A	Heyl **-3.02** OKAY	Il3 **1.00** C	Mdk **-5.24** OKAY	Mef2c **-5.77** OKAY	Kmt2a **-4.38** OKAY	Map2 **-3.98** OKAY	Ndn **-6.77** OKAY	Ndp **-6.47** OKAY	Neurod1 **-87.80** A	Neurog1 **1.00** C	Neurog2 **-4.36** A
E	Nf1 **-5.84** OKAY	Nog **-9.76** OKAY	Notch1 **-2.70** OKAY	Notch2 **-5.87** OKAY	Nr2e3 **-1.12** B	Nrcam **-8.08** OKAY	Nrg1 **-6.20** OKAY	Nrp1 **-11.35** OKAY	Nrp2 **-11.28** OKAY	Ntf3 **-26.44** B	Ntn1 **-4.47** OKAY	Tenm1 **-2.37** A
F	Olig2 **-3.85** OKAY	Pafah1b1 **-14.57** OKAY	Pard3 **-4.22** OKAY	Pax3 **1.00** C	Pax5 **1.93** OKAY	Pax6 **-4.41** OKAY	Pou3f3 **-5.01** OKAY	Pou4f1 **-2.26** B	Ptn **-10.42** OKAY	Rac1 **-8.90** OKAY	Robo1 **-10.24** OKAY	Rtn4 **-9.73** OKAY
G	S100a6 **-3.34** OKAY	S100b **-17.30** OKAY	Shh **-3.58** OKAY	Slit2 **-8.10** OKAY	Sod1 **-4.40** OKAY	Sox2 **-4.36** OKAY	Sox3 **-1.94** OKAY	Stat3 **-5.44** OKAY	Tgfb1 **-2.46** OKAY	Th **-10.96** B	Tnr **-3.20** OKAY	Vegfa **-17.44** OKAY

Figure IV-1: Heat map and software validation of targets in 84-gene Qiagen qRT-PCR Neurogenesis array. HMGB2+/+ vs HMGB2-/- cDNA samples from 24 hours of differentiation are loaded into this array **(A)** Heat map reflects the numbers in the table below which signify relative fold-change of the HMGB2-/- samples as compared with HMGB2+/+. Each box contains the gene symbol along with software validation as to the likelihood that the qRT-PCR reaction is reliable, with OKAY indicating statistically reliable CT values across samples. n=1 per genotype.

A

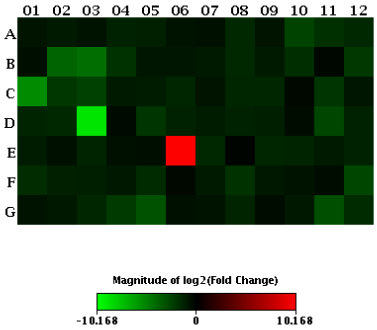

Layout	01	02	03	04	05	06	07	08	09	10	11	12
A	Aebp2 **-1.72** OKAY	Arid1a **-2.03** OKAY	Arid1b **-1.61** OKAY	Ash1l **-2.63** OKAY	Ash2l **-2.37** OKAY	Asxl1 **-1.62** OKAY	Asxl2 **-1.60** OKAY	Asxl3 **-3.01** OKAY	Bap1 **-1.72** OKAY	Bmi1 **-6.36** OKAY	Bptf **-3.79** OKAY	Cbx1 **-3.01** OKAY
B	Cbx2 **-1.47** OKAY	Cbx3 **-15.48** OKAY	Cbx4 **-21.03** A	Cbx5 **-3.92** OKAY	Cbx7 **-1.86** OKAY	Cbx8 **-1.80** OKAY	Ctbp1 **-2.07** OKAY	Ctbp2 **-2.96** OKAY	Cxxc1 **-2.07** OKAY	Dnmt1 **-3.56** OKAY	Dnmt3a **-1.17** OKAY	Dnmt3b **-4.69** A
C	Dnmt3l **-46.85** A	E2f6 **-4.34** OKAY	Eed **-6.01** OKAY	Epc1 **-2.08** OKAY	Ezh1 **-2.19** OKAY	Ezh2 **-2.86** OKAY	Hltf **-1.73** OKAY	Htt **-2.84** OKAY	Ino80 **-2.86** OKAY	Ino80b **-1.23** OKAY	Ino80c **-4.11** OKAY	Ino80d **-1.82** OKAY
D	Jarid2 **-2.75** OKAY	Kdm2b **-2.96** OKAY	Kdm5d **-574.53** A	L3mbtl2 **-1.34** OKAY	Larp7 **-4.30** OKAY	Mbtd1 **-2.56** OKAY	Kmt2a **-2.14** OKAY	Kmt2d **-2.62** OKAY	Kmt2c **-2.26** OKAY	Mov10 **-1.36** OKAY	Mtf2 **-6.92** OKAY	Pbrm1 **-2.63** OKAY
E	Pcgf1 **-2.20** OKAY	Pcgf2 **-1.52** OKAY	Pcgf5 **-2.73** OKAY	Phc1 **-1.52** OKAY	Phc2 **-1.45** OKAY	Phc3 **1150.38** A	Phf1 **-3.01** OKAY	Phf19 **-1.12** OKAY	Ppp1cc **-2.87** OKAY	Ppp1r8 **-2.76** OKAY	Rbbp4 **-2.08** OKAY	Rbbp5 **-2.59** OKAY
F	Rbbp7 **-3.43** OKAY	Rbp2 **-2.44** A	Ring1 **-2.32** OKAY	Rnasel **-1.92** OKAY	Rnf2 **-3.23** OKAY	Scmh1 **-1.22** OKAY	Scml2 **-2.09** OKAY	Sirt1 **-4.02** OKAY	Smarca1 **-1.90** OKAY	Smarca2 **-1.64** OKAY	Smarca4 **-1.42** OKAY	Smarca5 **-7.01** OKAY
G	Smarcb1 **-1.63** OKAY	Smarcc1 **-1.98** OKAY	Smarcc2 **-2.83** OKAY	Snai1 **-4.91** A	Suz12 **-9.75** OKAY	Trim27 **-1.55** OKAY	Usp11 **-1.64** OKAY	Usp7 **-2.71** OKAY	Kmt2b **-1.42** OKAY	Wdr5 **-1.97** OKAY	Yaf2 **-8.69** A	Zbtb16 **-3.21** OKAY

Figure IV-2: Heat map and software validation of targets in 84-gene Qiagen qRT-PCR PcG and trxG complex array. HMGB2+/+ vs HMGB2-/- cDNA samples from 24 hours of differentiation are loaded into this array **(A)** Heat map reflects the numbers in the table below which signify relative fold-change of the HMGB2-/- samples as compared with HMGB2+/+. Each box contains the gene symbol along with software validation as to the likelihood that the qRT-PCR reaction is reliable, with OKAY indicating statistically reliable CT values across samples. n=1 per genotype.

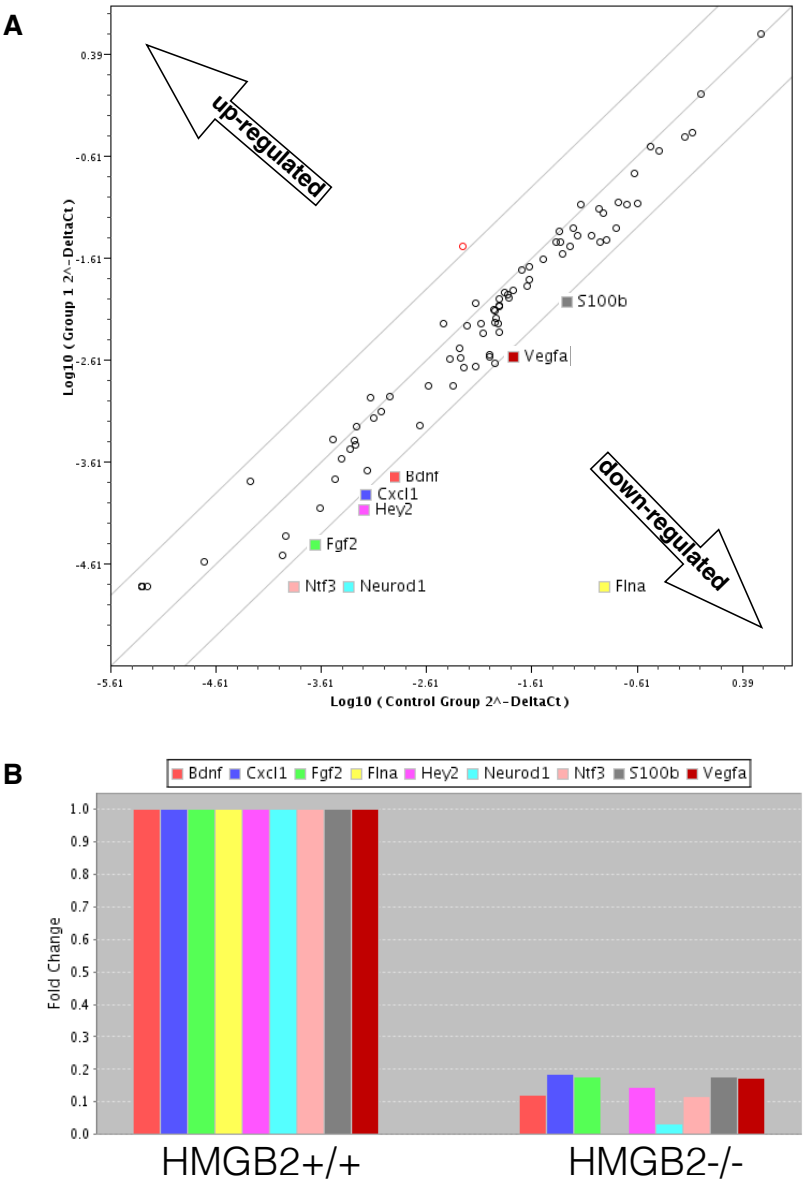
A
up-regulated
down-regulated
S100b
Vegfa
Bdnf
Cxcl1
Hey2
Fgf2
Ntf3
Neurod1
Flna
Log10 (Group 1 2^-DeltaCt)
Log10 (Control Group 2^-DeltaCt)
B
Bdnf Cxcl1 Fgf2 Flna Hey2 Neurod1 Ntf3 S100b Vegfa
Fold Change
HMGB2+/+
HMGB2-/-

Figure IV-3: Genes involved in neurogenesis downregulated in HMGB2 KO SVZ cultures as compared with WT. We set a 6-fold cutoff and appraised a subset of genes that met this criteria. **(A)** This scatter plot indicates up and down-regulated genes in NSCs at 24 hours of differentiation in the HMGB2 KO as compared with HMGB2+/+. The lower right quadrant contains a number of downregulated neurogenesis related genes in the HMGB2-/-. **(B)** This bar graph shows fold-change values for 10 downregulated neurogenesis related genes in the HMGB2-/- NSCs at 24 hours of differentiation. n=1 per genotype.

A

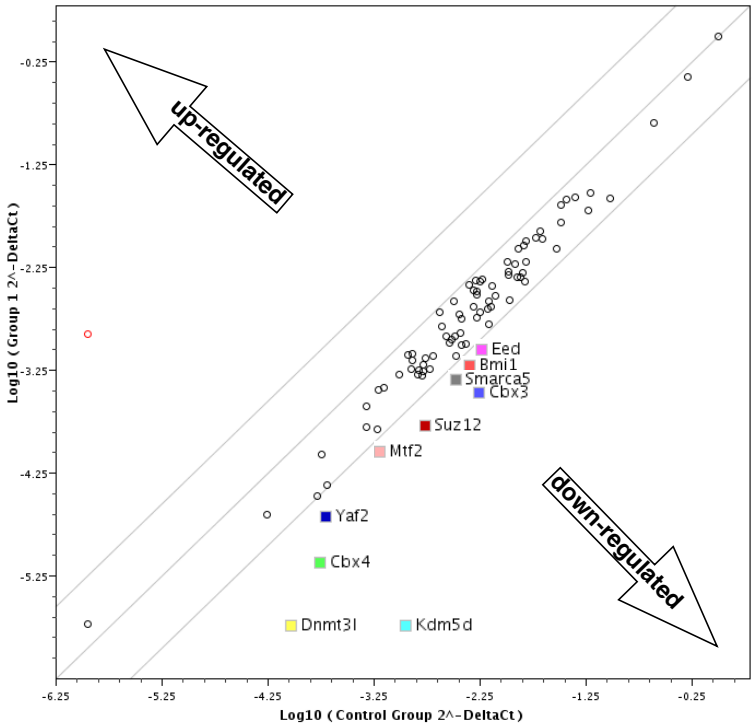
up-regulated
down-regulated
Log10 (Group 1 2^-DeltaCt)
Log10 (Control Group 2^-DeltaCt)
-0.25
-1.25
-2.25
-3.25
-4.25
-5.25
-6.25
-5.25
-4.25
-3.25
-2.25
-1.25
-0.25
Eed
Bmi1
Smarca5
Cbx3
Suz12
Mtf2
Yaf2
Cbx4
Dnmt3l
Kdm5d

B

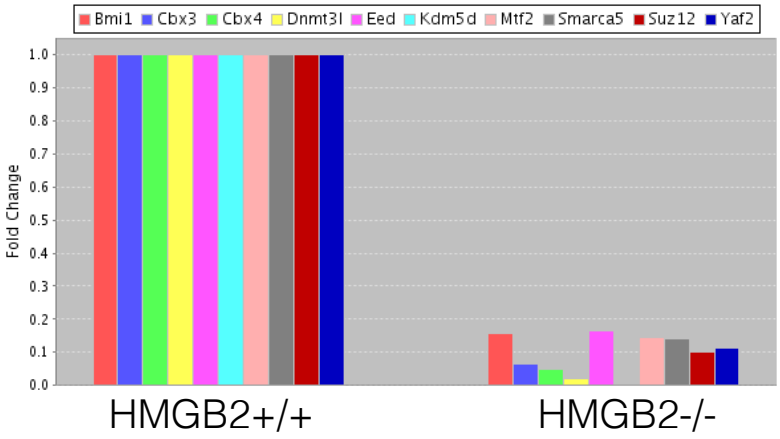
Bmi1
Cbx3
Cbx4
Dnmt3l
Eed
Kdm5d
Mtf2
Smarca5
Suz12
Yaf2
Fold Change
1.0
0.9
0.8
0.7
0.6
0.5
0.4
0.3
0.2
0.1
0.0
HMGB2+/+
HMGB2-/-

Figure IV-4: Genes encoding members of PcG and trxG complexes downregulated in HMGB2 KO SVZ cultures as compared with WT. We set a 6-fold cutoff and appraised a subset of genes that met this criteria. **(A)** This scatter plot indicates up and down-regulated genes in NSCs at 24 hours of differentiation in the HMGB2 KO as compared with HMGB2+/+. The lower right quadrant contains a number of downregulated PcG and trxG complex genes in the HMGB2-/-. **(B)** This bar graph shows fold-change values for 10 downregulated PcG and trxG complex genes in the HMGB2-/- NSCs at 24 hours of differentiation. n=1 per genotype.

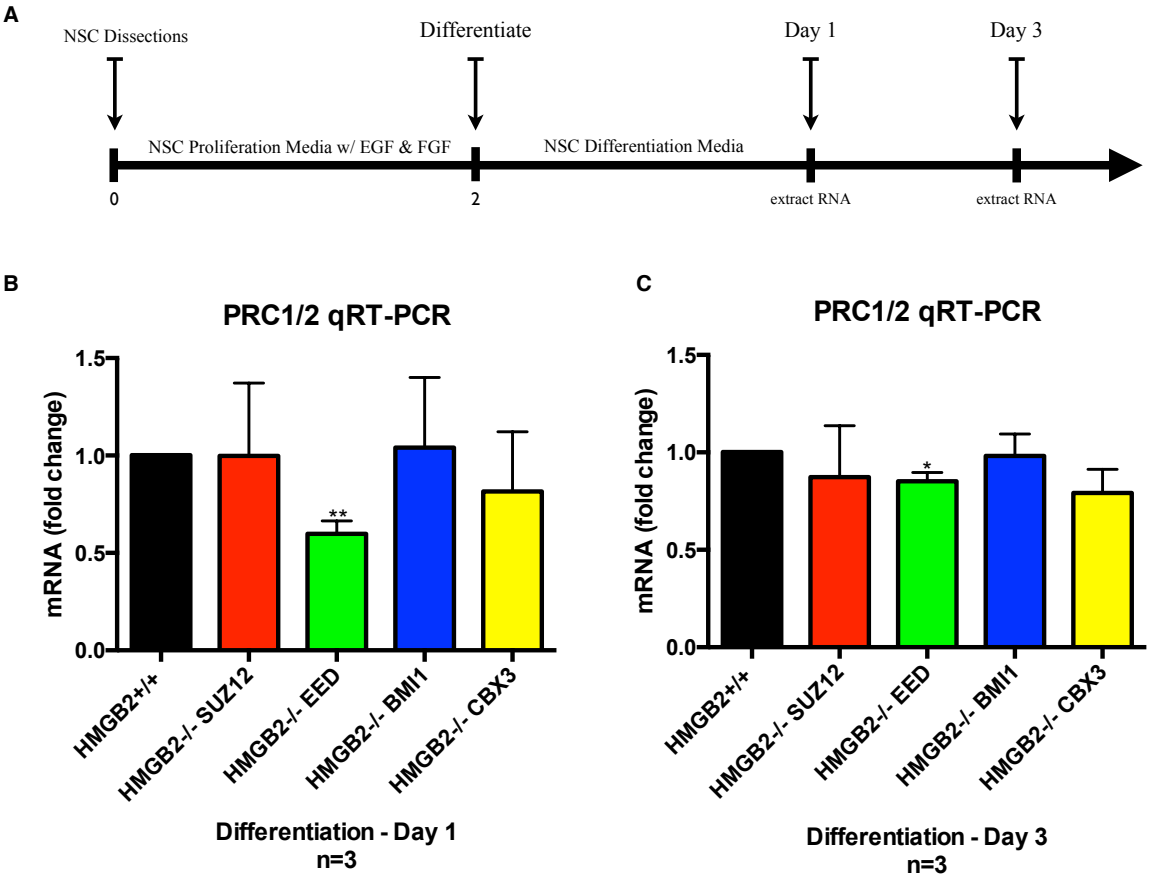
A
NSC Dissections
Differentiate
Day 1
Day 3
NSC Proliferation Media w/ EGF & FGF
NSC Differentiation Media
0
2
extract RNA
extract RNA
B
PRC1/2 qRT-PCR
mRNA (fold change)
1.5
1.0
0.5
0.0
**
HMGB2+/+
HMGB2-/- SUZ12
HMGB2-/- EED
HMGB2-/- BMI1
HMGB2-/- CBX3
Differentiation - Day 1
n=3
C
PRC1/2 qRT-PCR
mRNA (fold change)
1.5
1.0
0.5
0.0
*
HMGB2+/+
HMGB2-/- SUZ12
HMGB2-/- EED
HMGB2-/- BMI1
HMGB2-/- CBX3
Differentiation - Day 3
n=3

Figure IV-5: Validation of genes downregulated in PcG and trxG arrays via qRT-PCR. Following differentiation of NSCs for one and three days cDNA was obtained for verification of gene expression patterns obtained via qRT-PCR arrays. **(A)** Representative experimental timeline demonstrating two days of primary NSC proliferation followed by differentiation of one and three days. **(B)** qRT-PCR results from samples obtained at day one of differentiation showing fold-change differences for four key PcG subunit complex genes, with EED showing significant downregulation in the HMGB2-/- samples as compared with HMGB2+/+. **(C)** qRT-PCR results from samples obtained at day three of differentiation showing fold-change differences for four key PcG subunit complex genes, with EED showing significant downregulation in the HMGB2-/- samples as compared with HMGB2+/+. n=3 per genotype. **EED at day one p=.0038 *EED at day three p=0.0109

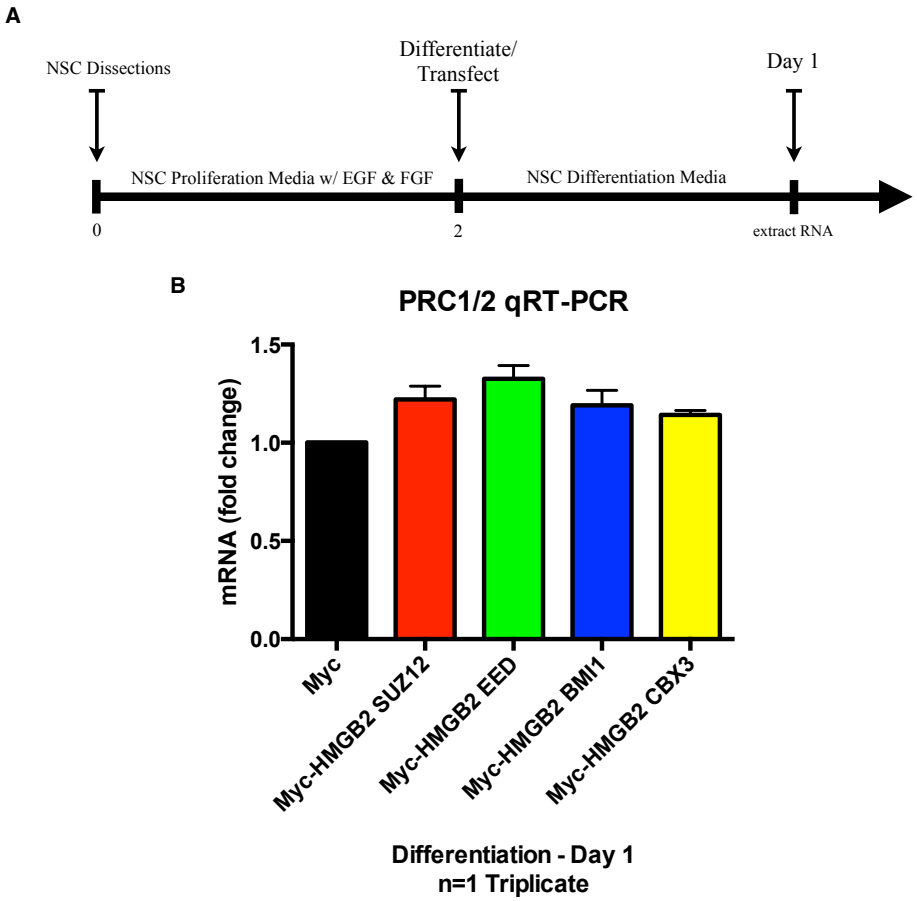
A
NSC Dissections
Differentiate/
Transfect
Day 1
NSC Proliferation Media w/ EGF & FGF
NSC Differentiation Media
0
2
extract RNA
B
PRC1/2 qRT-PCR
mRNA (fold change)
1.5
1.0
0.5
0.0
Myc
Myc-HMGB2 SUZ12
Myc-HMGB2 EED
Myc-HMGB2 BMI1
Myc-HMGB2 CBX3
Differentiation - Day 1
n=1 Triplicate

Figure IV-6: Upregulation of PcG genes following transfection of constitutively active Myc-HMGB2 into NSCs. We sought to constitutively up-regulate HMGB2 in primary mouse perinatal NSCs and observe their behavior following one day of differentiation. **(A)** Timeline of experimental route indicating two day period of proliferation, followed by transfection with empty Myc and Myc-tagged HMGB2 plasmids and subsequent one day of differentiation. **(B)** qRT-PCR results from samples obtained at day one of differentiation showing fold-change differences for four key PcG subunit complex genes, with EED showing modest upregulation in the samples transfected with Myc-tagged HMGB2 as compared to the empty Myc plasmid. n=1 per genotype, three technical replicates per n.

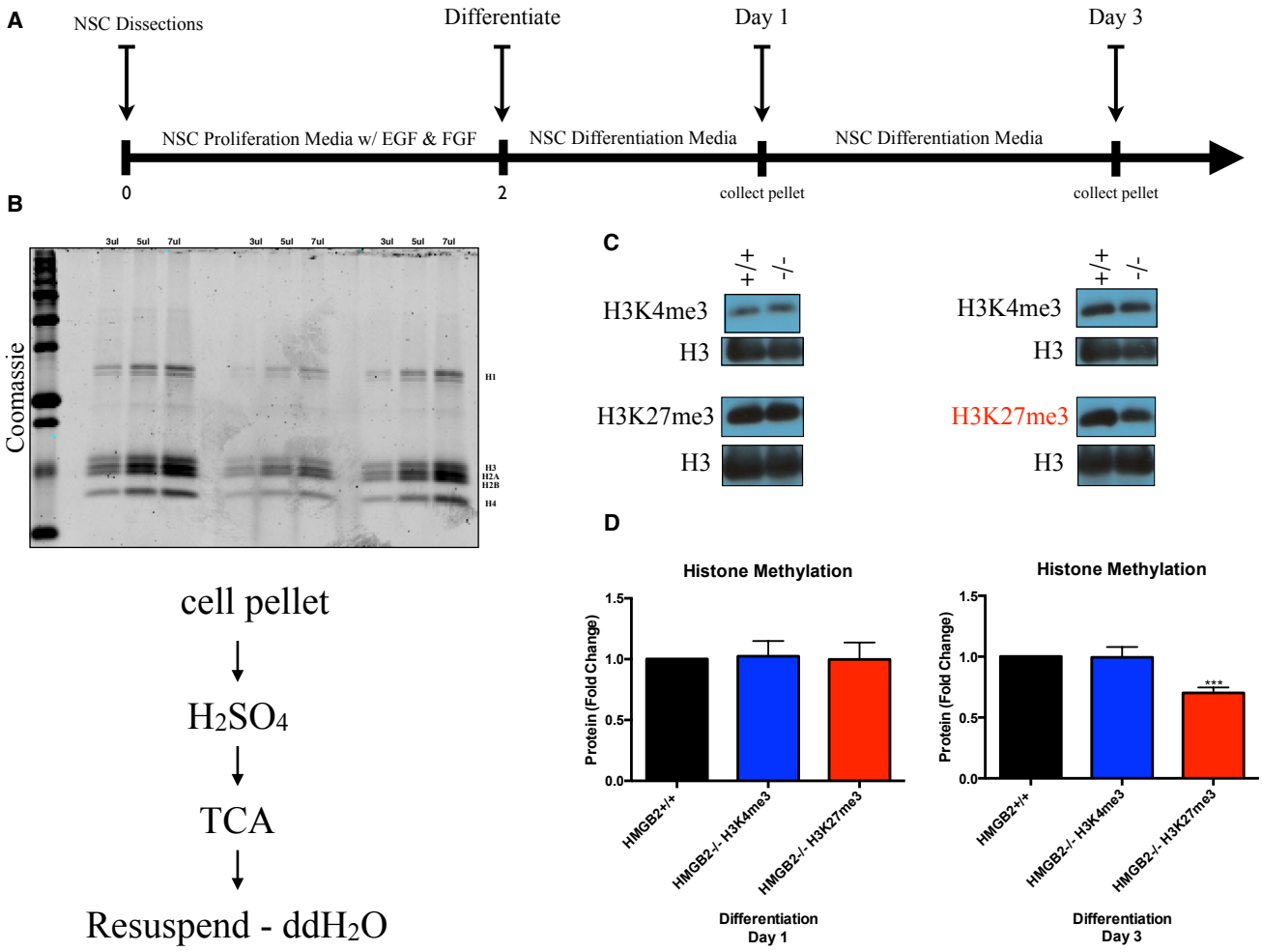
A
NSC Dissections
Differentiate
Day 1
Day 3
NSC Proliferation Media w/ EGF & FGF
NSC Differentiation Media
NSC Differentiation Media
0
2
collect pellet
collect pellet
B
3ul 5ul 7ul 3ul 5ul 7ul 3ul 5ul 7ul
Coomassie
H1
H3
H2A
H2B
H4
cell pellet
H2SO4
TCA
Resuspend - ddH2O
C
+/+
-/-
H3K4me3
H3
H3K27me3
H3
+/+
-/-
H3K4me3
H3
H3K27me3
H3
D
Histone Methylation
Protein (Fold Change)
1.5
1.0
0.5
0.0
HMGB2+/+
HMGB2-/- H3K4me3
HMGB2-/- H3K27me3
Differentiation Day 1
Histone Methylation
Protein (Fold Change)
1.5
1.0
0.5
0.0
***
HMGB2+/+
HMGB2-/- H3K4me3
HMGB2-/- H3K27me3
Differentiation Day 3

Figure IV-7: Changes in repressive histone modifications in differentiating NSCs. The purpose of the following figure is to assess the levels of certain permissive and repressive histone methylations in differentiating NSCs. **(A)** The experimental time course employed, with protein readouts coming at days one and three of NSC differentiation. **(B)** Histone proteins were purified with sulfuric acid (H_2SO_4) and subsequently precipitated using trichloroacetic acid (TCA), with quantification of protein quantities demonstrated on this coomassie stained acrylamide gel. **(C)** Western blots employing antibodies against the histone modifications H3K4me3 and H3K27me3 which are permissive and repressive, respectively. Total histone H3 represents the loading control. **(D)** Quantification of the histone methylation western blot results showing reduction in H3K27me3 at three days of NSC differentiation in the HMGB2-/- NSCs. n=3-4 biological replicates per genotype. ***H3K27me3 from HMGB2-/- at day three p= 0.0001

A

Day 1 Differentiation

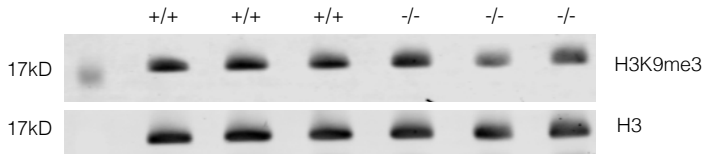

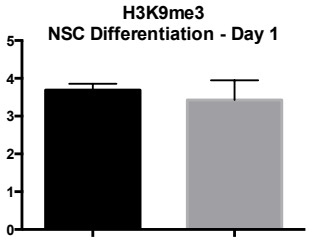

B

Day 3 Differentiation

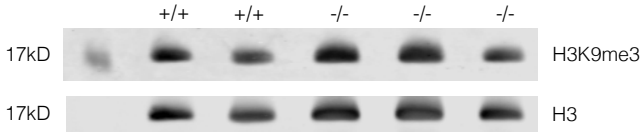

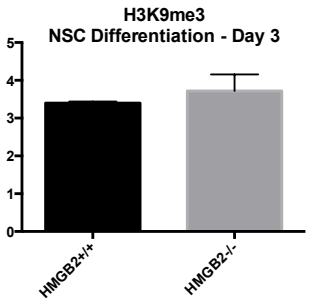

Figure IV-8: Histone modification H3K9me3 remains unchanged at days one and three of NSC differentiation. Depiction of another repressive histone modification H3K9me3 **(A)** Western blots employing antibodies against the histone modification H3K9me3, followed by quantification of the results. Total histone H3 represents the loading control. n=2-3 biological replicates per genotype.

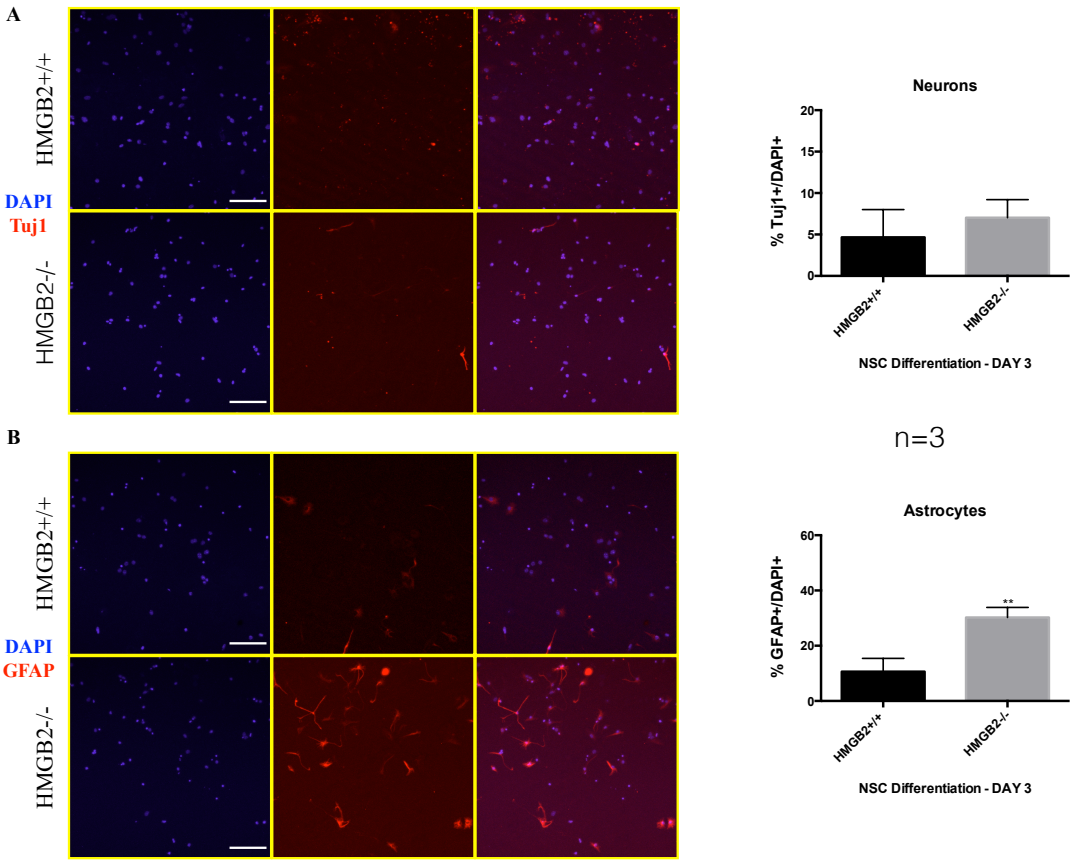
A
HMGB2+/+
DAPI
Tuj1
HMGB2-/-
Neurons
% Tuj1+/DAPI+
20
15
10
5
0
HMGB2+/+
HMGB2-/-
NSC Differentiation - DAY 3
n=3
B
HMGB2+/+
DAPI
GFAP
HMGB2-/-
Astrocytes
% GFAP+/DAPI+
60
40
20
0
**
HMGB2+/+
HMGB2-/-
NSC Differentiation - DAY 3

Figure IV-9: Ratios of neural and glial cell altered in HMGB2-/- SVZ cultures at day three of differentiation. NSCs were cultured in 8-well chamber slides with growth factor-free media and allowed to differentiate. **(A)** Chamber slides from HMGB2+/+ and HMGB2-/- NSCs stained for the immature neuronal marker Tuj1, all results represented as percentage of Tuj1+ (Red) cells to all 4',6-diamidino-2-phenylindole+(DAPI+)(Blue)nuclei. **(B)** Chamber slides from HMGB2+/+ and HMGB2-/- NSCs stained for the astrocyte marker GFAP, all results represented as percentage of GFAP+ (Red) cells to all DAPI+ (Blue) nuclei. n=3 biological replicates per genotype. **GFAP p=0.0049

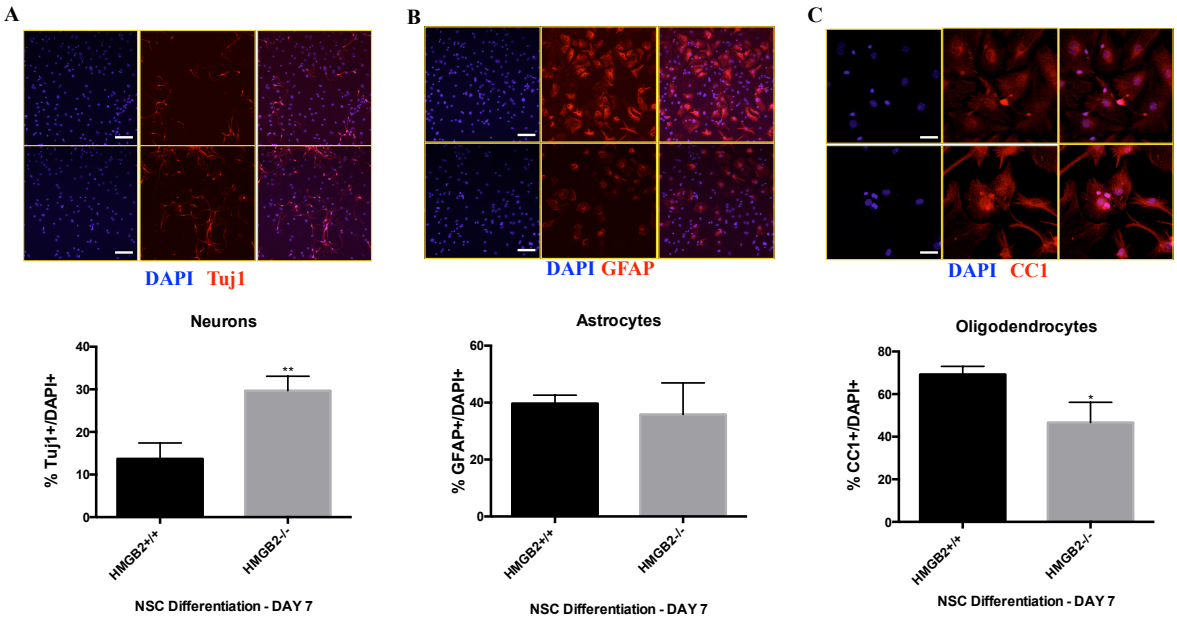
A
B
C
DAPI Tuj1
DAPI GFAP
DAPI CC1
Neurons
Astrocytes
Oligodendrocytes
% Tuj1+/DAPI+
% GFAP+/DAPI+
% CC1+/DAPI+
HMGB2+/+
HMGB2-/-
NSC Differentiation - DAY 7

Figure IV-10: Ratios of neural and glial cell altered in HMGB2-/- SVZ cultures at day seven of differentiation. NSCs were cultured in 8-well chamber slides with growth factor-free media and allowed to differentiate. **(A)** Chamber slides from HMGB2+/+ and HMGB2-/- NSCs stained for the immature neuronal marker Tuj1, all results represented as percentage of Tuj1+ (Red) cells to all DAPI+ (Blue) nuclei. **(B)** Chamber slides from HMGB2+/+ and HMGB2-/- NSCs stained for the astrocyte marker GFAP, all results represented as percentage of GFAP+ (Red) cells to all DAPI+ (Blue) nuclei. n=3 biological replicates per genotype. **(C)** Chamber slides from HMGB2+/+ and HMGB2-/- NSCs stained for the oligodendrocyte marker CC1, all results represented as percentage of CC1+ (Red) cells to all DAPI+ (Blue) nuclei. n=3 biological replicates per genotype. **Tuj1 p=0.0054 *CC1 p=0.0189

Chapter V

Thalamic Stroke

Introduction

Cerebral infarcts in the human thalamus generally occur due to small vessel disease, unlike the more common MCA territory strokes, which are predominantly caused by a dislodged thrombus in the CNS or periphery(Kausar and Antonios, 2013). These modestly sized strokes can sometimes occur bilaterally, with their presentation including the involvement of the artery of Percheron (AOP) and the posterior cerebral artery (PCA) (Papuć et al., 2012; 2014a). Unilateral infarcts of the thalamus are more common, involving vessels such as the paramedian artery (PA) and the tuberothalamic artery (TA) (Schmahmann, 2003). Disturbances following thalamic infarction can range from central post-stroke pain (CPSP), to aphasia and potential disruption in arousal and memory (Schmahmann, 2003). Thalamic infarcts involving ventromedial (VM) nuclei in humans can impose defects on motor programming and coordination – gravely affecting quality of life (Schmahmann, 2003). The thalamus is a central switch-board in the CNS, and as such has many feedback and feed forward connections with various cortical and subcortical structures (Cruikshank et al., 2012; 2010; Hooks et al., 2013). Thalamocortical (TC) axons stereotypically project to layer 4 of cerebral cortex, with layer 6 sending feedback connections to subcortical structures such as striatum, and finally back to thalamus (Clascá et al., 2012). The murine thalamic compartment is set up in a largely complementary fashion to that of humans, with discrete nuclei routing peripheral sensory and motor information to cortical and subcortical areas (Monconduit and Villanueva, 2005; Viaene et al., 2011). In the mouse, the VM thalamus has dense TC projections to primary and secondary motor cortices, in a largely ipsilateral fashion as well as weaker connections to somatosensory/barrel cortices (Clascá et al., 2012; 2007b). The TC axons are so called M-

type (multiareal), and primarily target layers 5a and 1a, with calbindin+ fibers (Clascá et al., 2012). The pial projections in layer 1a are quite unique, with long, branched arborizations targeting a wide swath of the superficial cortex (Clascá et al., 2012). Although cortical and closely sub-cortical infarcts are readily modeled in rodent systems using various methods such as tMCAO, photothrombosis as well as the injection of a physical thrombus into the vertebral arteries, many fewer models are able to apply focally ischemic lesions in the thalamic territory(Carmichael, 2005; Sozmen et al., 2012; 2009; 2015b).

The ET-1 stroke model was developed initially in the rat model system and uses the intracerebral injection of a vasoconstrictive peptide to transiently and focally disrupt blood flow in discrete brain regions (Horie et al., 2008; Macrae et al., 1993). This model is advantageous for studying small lacunar infarcts because unlike tMCAO it can be stereotaxically targeted, and unlike photothrombosis it closely recapitulates the physiology of human strokes – including temporary stoppage of blood flow and eventual reperfusion/injury (Horie et al., 2008). In mice ET-1 injections are commonly used as a model of white matter ischemia targeting structures such as the corpus callosum with memory impairments and interhemispheric disturbances a common outcome (Blasi et al., 2014). ET-1 has also recently been used in the thalamus to model central post-stroke pain (CPSP), with late-onset thermal hypersensitivity being a fairly accurate correlate of the late onset symptomology evident in cases of human thalamic stroke (2015b).

Results

We therefore sought to utilize the ET-1 experimental paradigm to model ET-1 ischemia in the VM thalamus and observe the cortical and behavioral readouts of such manipulations in WT and HMGB2-/- mice. The use of the HMGB2-/- model in this set of experiments was predicated on the fact that HMGB2 is a potent damage-associated molecular pattern (DAMP), and as such promotes cell death signaling in instances of ischemia (Hock et al., 2007; Lee et al., 2014; Malarkey and Churchill, 2012). We therefore were interested in determining whether the genetic ablation of HMGB2 would have any effect on cortical apoptotic signaling following ET-1 induced ischemia. We initiated these studies through the histopathological verification of stroke in VM thalamus via cresyl violet immunohistochemistry – and indeed we observed a localized infarct core with a clear hypoperfused penumbra (Figure V-1B). ET-1 in the CNS is primarily synthesized by microvascular endothelial cells and astrocytes, with cognate receptors ET-1A and ET-1B being expressed in a number of cell types including microglia, NG2+ cells and mature oligodendrocytes (Gadea et al., 2009). Prior to engaging in a comparative study of ET-1 ischemia in the animals we sought to confirm that the levels of ET-1 and its receptors in the thalamus did not differ in baseline conditions. RT-PCR demonstrated that the peptide ET-1 and its receptors ET-1A and ET-1B are indeed expressed at similar levels in both the HMGB2+/+ and HMGB2-/- thalamus (Figure V-1C). Human strokes are classified by a size ratio of penumbra to infarct core, with the outcome of this characterization often driving therapeutic decisions (2006). In our system ET-1 injected VM thalamic nuclei demonstrated a clear stroke core surrounded by a prominent penumbra made up of GFAP+ astrogliosis (Figure V-2A) indicating that the ET-1 model of murine ischemia at least

partially recapitulated the physiological features of human thalamic ischemia. Microglia are the resident immune cells in the CNS and as such function to remove apoptotic cells, clean up debris, as well as having a prominent role in the physiologically normal brain (Neumann et al., 2006; Sierra et al., 2010; Thiel and Heiss, 2011). Increased microgliosis is evident following any kind of injury and is a pathological hallmark of ischemic injury in particular (Neumann et al., 2006; 2008; Thiel and Heiss, 2011). We performed immunofluorescence for the microglial/macrophage maker Iba1 in the WT mouse brain following injection of ET-1 and observed considerable microgliosis around and within the lesion and penumbra (Figure V-3A). To assess the extent of neuronal death following the injection of ET-1, we used Fluoro-Jade C staining (positively stains degenerating neurons) on ET-1 injected brain sections from HMGB2+/+ mice and demonstrate a considerable number of apoptotic/necrotic neurons within the stroke core (Diaz et al., 2013) (Figure V-3A). Mini-strokes in the thalamus can result in inter and intrahemispheric circuit loss (Mohajerani et al., 2011). Since the VM thalamus contains large numbers of axonal projections to primary and secondary motor cortices it would be possible that ET-1 stroke would result in projection loss and affect cell death in the cortex. Following staining of coronal anterior HMGB2+/+ brain sections for the apoptotic marker cleaved caspase 3 and the neuronal marker NeuN, we indeed observed large numbers of apoptotic neurons in the primary and secondary motor cortices which were absent in the saline injected animals (Figure V-4B). Given the extracellular role HMGB2 serves as a DAMP (Malarkey and Churchill, 2012), cell death signalling in different cortical areas between the HMGB2+/+ and HMGB2-/- brains following ET-1 thalamic ischemia was evaluated (Figures V-5,6,7). Again, staining for NeuN and cleaved caspase 3 in the primary and secondary motor

cortex revealed large numbers of apoptotic neurons in the HMGB2+/+ mouse brain, while the HMGB2-/- brain sections revealed a trend towards lower numbers of apoptotic neurons in both of these areas (Figures V-5,6). Meanwhile the somatosensory/barrel cortex, which also receives feed forward input from VM thalamus exhibited no difference between genotypes (Figures V-7). Cortical apoptosis was not layer specific, however may present as such at earlier timepoints following ET-1 ischemia. Whether feed forward or feedback connections were responsible for the cortical apoptosis phenotype we observed will require further experimentation.

Observation of the animals following the ET-1 injections suggested that there may be a behavioral correlate of ET-1 ischemia in the VM thalamus following the focal and comparatively small ischemic insult. We recorded the free-moving activity of HMGB2+/+ and HMGB2-/- mice in their home cage from day two through day seven following ET-1 induced thalamic ischemia (Figure V-8). Mice commonly rear up on the walls of their cages to palpate and smell their surrounding environment (2010). We recorded each mouse for one minute in their home cage and calculated the number of times mice reared up on the side of the cage with the left paw, the right paw, or both paws (Figure V-8). Two experimental groups comprised of HMGB2+/+ mice with either saline or ET-1 injected cohorts with the same two groups for HMGB2-/- animals. While post-op days 2/3 contained relatively little variation between the four treatment groups, at later time points it became obvious that ET-1 injected animals reared up considerably less than those injected with into the VM thalamus with saline only (Figure V-8). This was true across both genotypes (Figure V-8). Other than this general trend which may reflect either anxiety-like behavior or actual motor impairments potentially linked to the apoptotic

neurons present in primary and secondary motor cortices a significant reduction in rearing was observed with only the left paw in the HMGB2-/- animals compared with saline injected controls five days following stereotactic surgery (Figure V-8).

To assess more quantitatively the motor characteristics of HMGB2+/+ and HMGB2 KO mice following ET-1 injections into the VM thalamus we utilized the Catwalk XT gait analysis system from Noldus (Chiang et al., 2014). This system allows for a video-based methodical dissection of many gait characteristics some of which may be perturbed in instances of thalamic ischemia(Chiang et al., 2014). The following treatment groups were utilized for this set of behavioral analyses (Figure V-9). We selected six distinct front and hind limb parameters for our analysis: (1) Stand – the time in seconds of paw contact with the glass device surface (Figure V-10), (2) Max Contact Area – a calculation of the maximum area of the paw coming into contact with the glass plate (Figure V-11), (3) Print Area – the surface area of the entire mouse print on the glass surface (Figure V-12), (4) Step Cycle – measurement of time between two consecutive initial contacts, with the glass plate, of the same paw (Figure V-13), (5) Duty Cycle – a percentage of the step cycle divided by stand + swing of the paws (Figure V-14), (6) Stride Length – distance between consecutive placement of the same paws (Figure V-15)(Chen et al., 2014; Chiang et al., 2014). In this analysis we employed the four experimental groups listed earlier, using primarily post-hoc analysis methods to uncover subtle differences between the groups. HMGB2+/+ injected with ET-1 in the VM thalamus all had significant reductions in the six distinct gait parameters listed above as compared with saline injected HMGB2+/+ animals; these changes were not observed between the comparable HMGB2-/- treatment groups (Figure V-10,11,12,13,14,15). The left hind limb in the HMGB2+/+ ET-1 injected

animals was primarily affected across all limb characteristics measured, with the right and front limbs exhibiting little to change from saline baseline (Figure V-10,11,12,13,14,15). Left hind limb max contact area in the ET-1 injected HMGB2+/+ mice, as compared with saline injected HMGB2+/+, exhibited the largest statistically significant swing (Figure V-11).

Discussion

We have demonstrated the development and refinement of a model of focal stroke in the VM thalamus, specifically aimed at recapitulating small lacunar infarcts occurring in humans as a result of small vessel disease and uncontrolled hypertension (Bailey et al., 2009; Hainsworth et al., 2012; He et al., 1999). The vast majority of stroke models target cortical and closely sub-cortical structures such as the caudate/putamen – however the thalamus is often omitted from the target list due to its relative inaccessibility and large variety of axonal projections, which potentially complicate analysis of outcomes (Clascá et al., 2012). Stereotaxic injections of the vasoconstrictive peptide ET-1 allows specific deep area targeting in the brain, and maintains the stroke hallmarks of reperfusion injury, and substantial edema (Huang et al., 2013). The focus on the VM thalamus because of its stereotypic and dense projections to primary and secondary motor cortices allowed exploration of different aspects of motor programming (Clascá et al., 2012). Specificity of stereotaxic injections fully depends on the agent being injected, and although viral injections which do little damage are extremely specific, damaging agents such as ET-1 and others do affect adjoining brain regions potentially muddling the behavioral analysis. However the saline controls can adequately offset such confounders. There has been some debate in the field about the robustness of the ET-1 stroke model in the mouse system

(Horie et al., 2008), with a variety of genetic backgrounds demonstrating different susceptibility to the vasoconstrictive agent – however our data indicate reproducible focal infarcts in the VM thalamus, potentially due to the large numbers of ET-1 receptors present in the thalamic microvasculature. Overall, ET-1 ischemia, at least in the context of the VM thalamus in the C57Bl6/J background, has proven to be a robust model of lacunar ischemia in a critical sub-cortical structure.

A

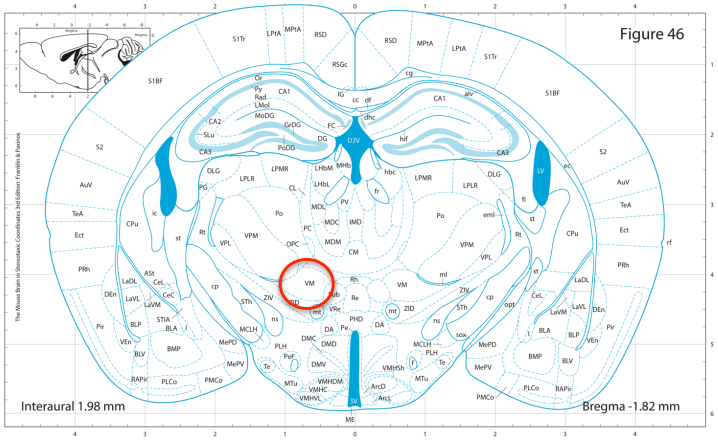
Figure 46
Interaural 1.98 mm
Bregma -1.82 mm

B

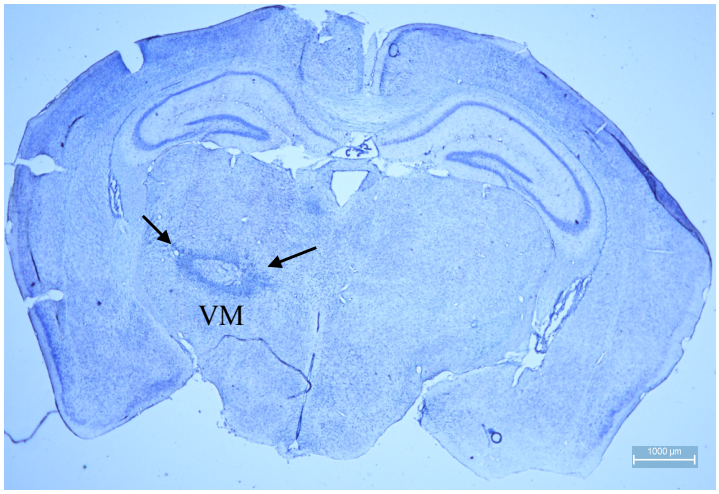
VM
1000 µm

C

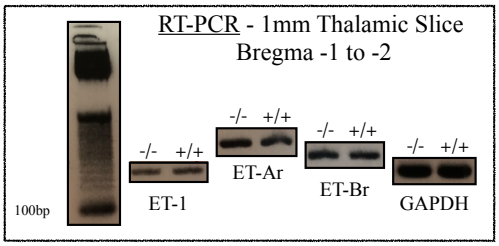
RT-PCR - 1mm Thalamic Slice
Bregma -1 to -2
100bp
-/- +/+
ET-1
-/- +/+
ET-Ar
-/- +/+
ET-Br
-/- +/+
GAPDH

Figure V-1: Targeting of ET-1 ischemic lesion to VM nucleus of thalamus in a WT mouse brain. Verification of VM thalamic stroke location and morphology. **(A)** Slide from (2004c), mouse brain in stereotaxic coordinates indicating VM as target for ET-1 injections. **(B)** Cresyl violet stained tissue section demonstrating unilateral injection of 1μgof ET-1 into the VM murine thalamus, with evident stroke core and hypoperfused penumbra. **(C)** RT-PCR employing primers for ET-1 and its cognate receptors ET-1A and ET-1B in a 1mm brain slice encompassing the VM thalamus, cut on a coronal brain matrix. Cresyl Violet n=2. RT-PCR n=2.

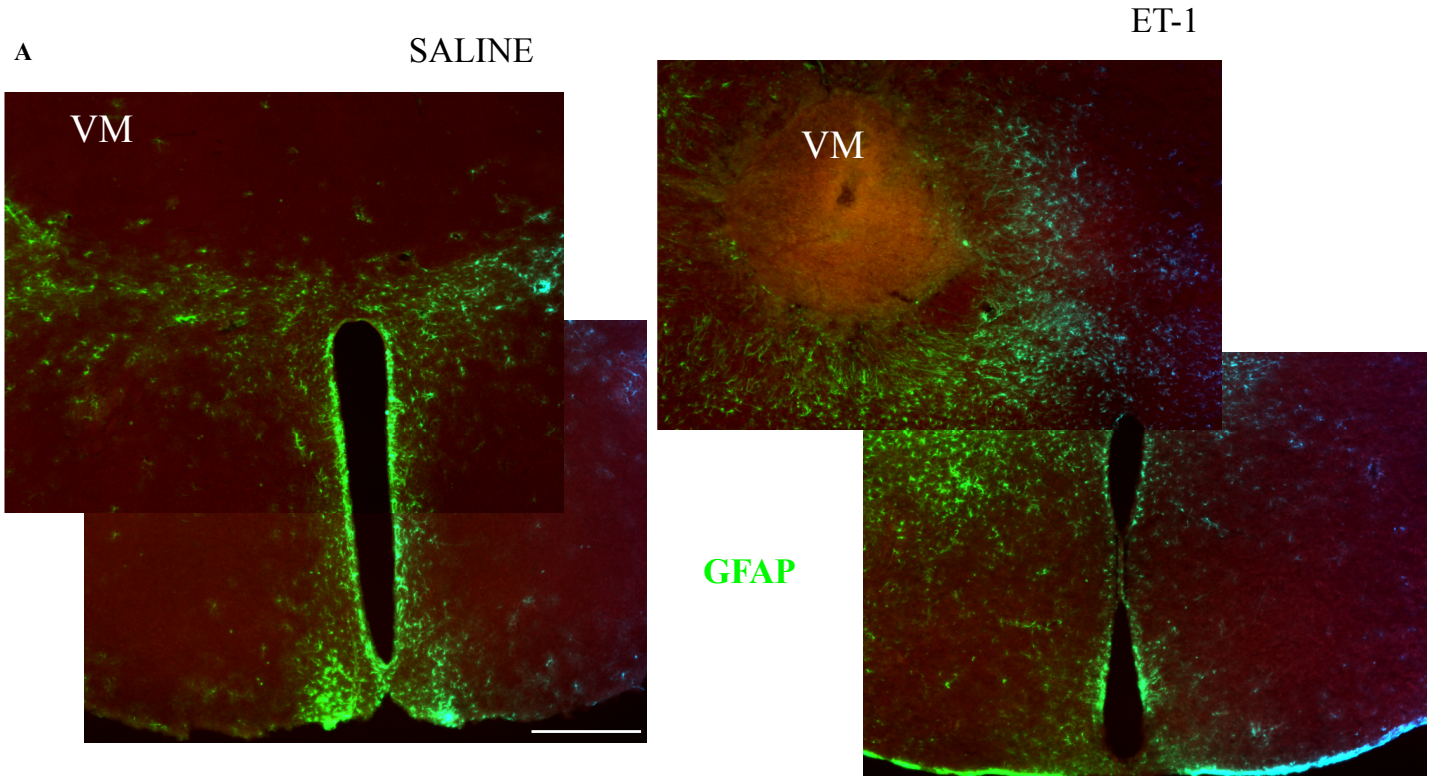
A
SALINE
ET-1
VM
VM
GFAP

Figure V-2: Pronounced stroke core presence and glial scar formation in ET-1 injected VM thalamus. (A) Saline and ET-1 injected VM thalamic nuclei demonstrating clear stroke morphology in the ET-1 injected section, with large core and GFAP+ cells encompassing the glial scar/penumbra of the infarct. Normal GFAP+ staining also present along the 3rd ventricle NSC niche in both the saline and ET-1 injected brains. n=2 per saline and ET-1 injections.

A

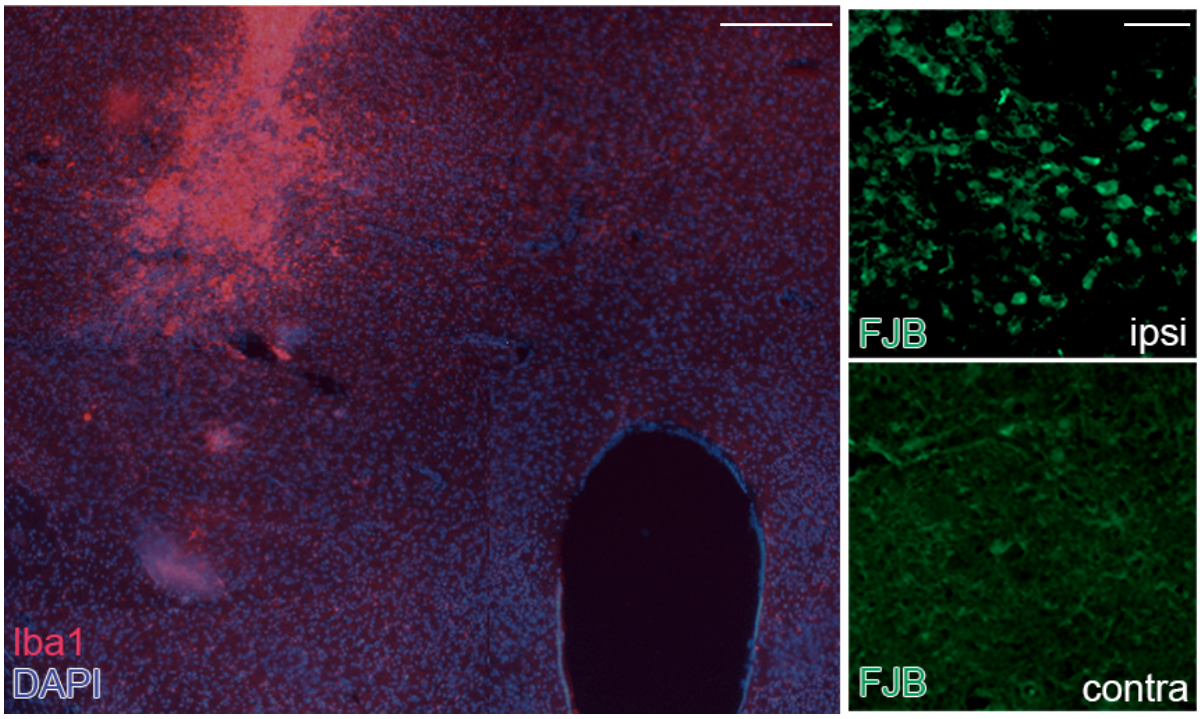

Figure V-3: Microgliosis and neuronal death in VM thalamus following ET-1 stroke. Staining to demonstrate immunological response to stroke and cell death outcomes. **(A)** Left panel depicts unilateral ET-1 induced ischemia, with staining for the microglial marker Iba1 and DAPI, pointing to ample microgliosis in within and around the stroke center, including along the injection tract more dorsally. Right side of the panel shows FJB staining of neuronal death in the VM thalamus ipsilateral to the ET-1 injection with little to no FJB+ cells contralateral. n=1 Iba1 staining. n=2 FJB staining.

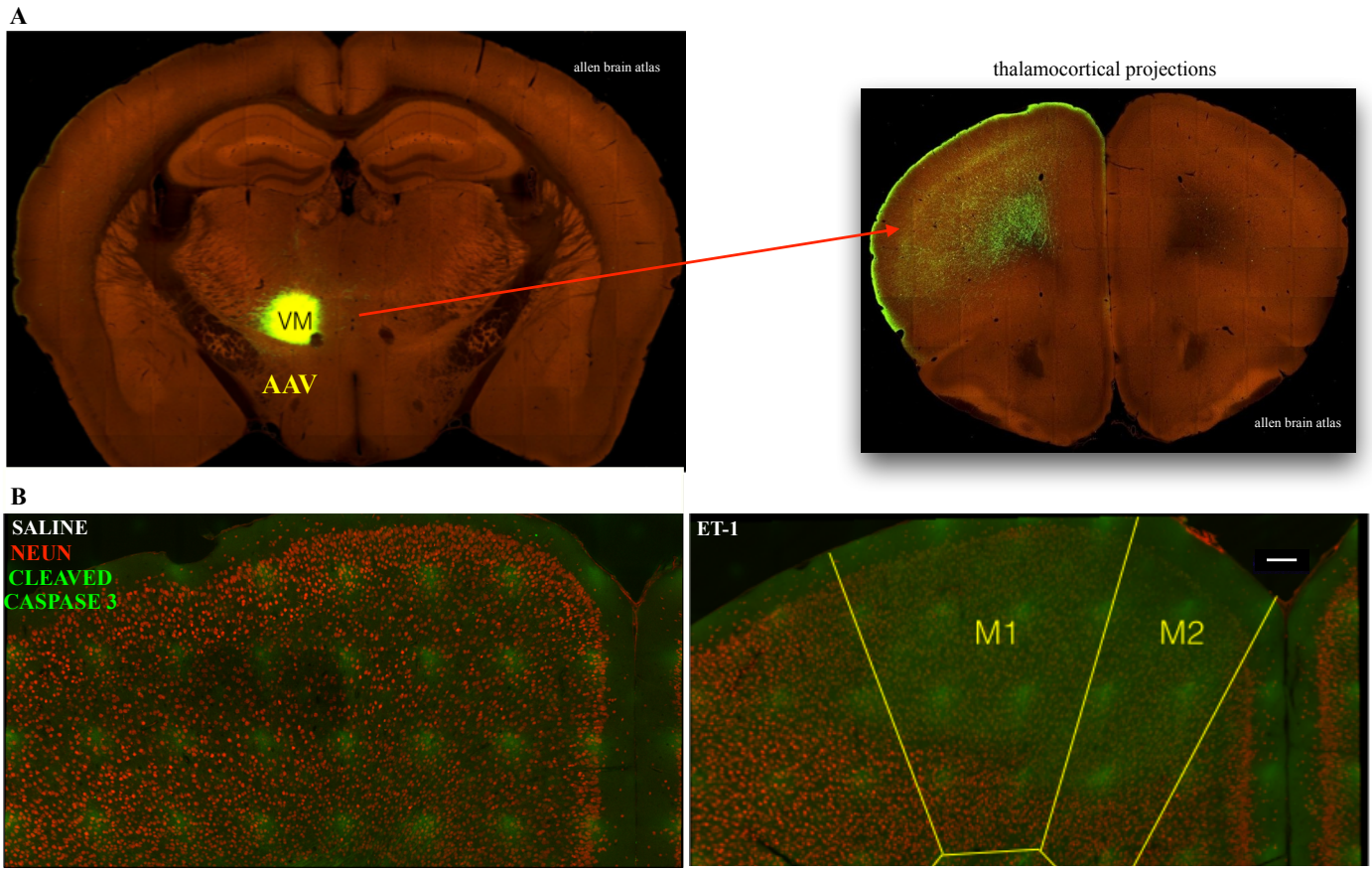
A
allen brain atlas
VM
AAV
thalamocortical projections
allen brain atlas
B
SALINE
NEUN
CLEAVED
CASPASE 3
ET-1
M1
M2

Figure V-4: VM thalamic projections target motor cortex and display apoptotic cell death in ET-1 injected brains. Confocal tile scans of anterior WT mouse brain following injection of ET-1 into the VM thalamus under a 20X objective. **(A)** Tracing of VM projections to primary and secondary motor cortices via AAV injections (Allen Brain Connectivity Atlas). **(B)** WT mouse primary and secondary motor cortices following injection of either saline or ET-1 into the VM thalamus respectively. Sections were stained for NeuN (Red), cleaved caspase 3 (Green), DAPI (Blue) demonstrating increased apoptotic neuronal cell death in the cortex following thalamic injection of ET-1, but not saline. n=2

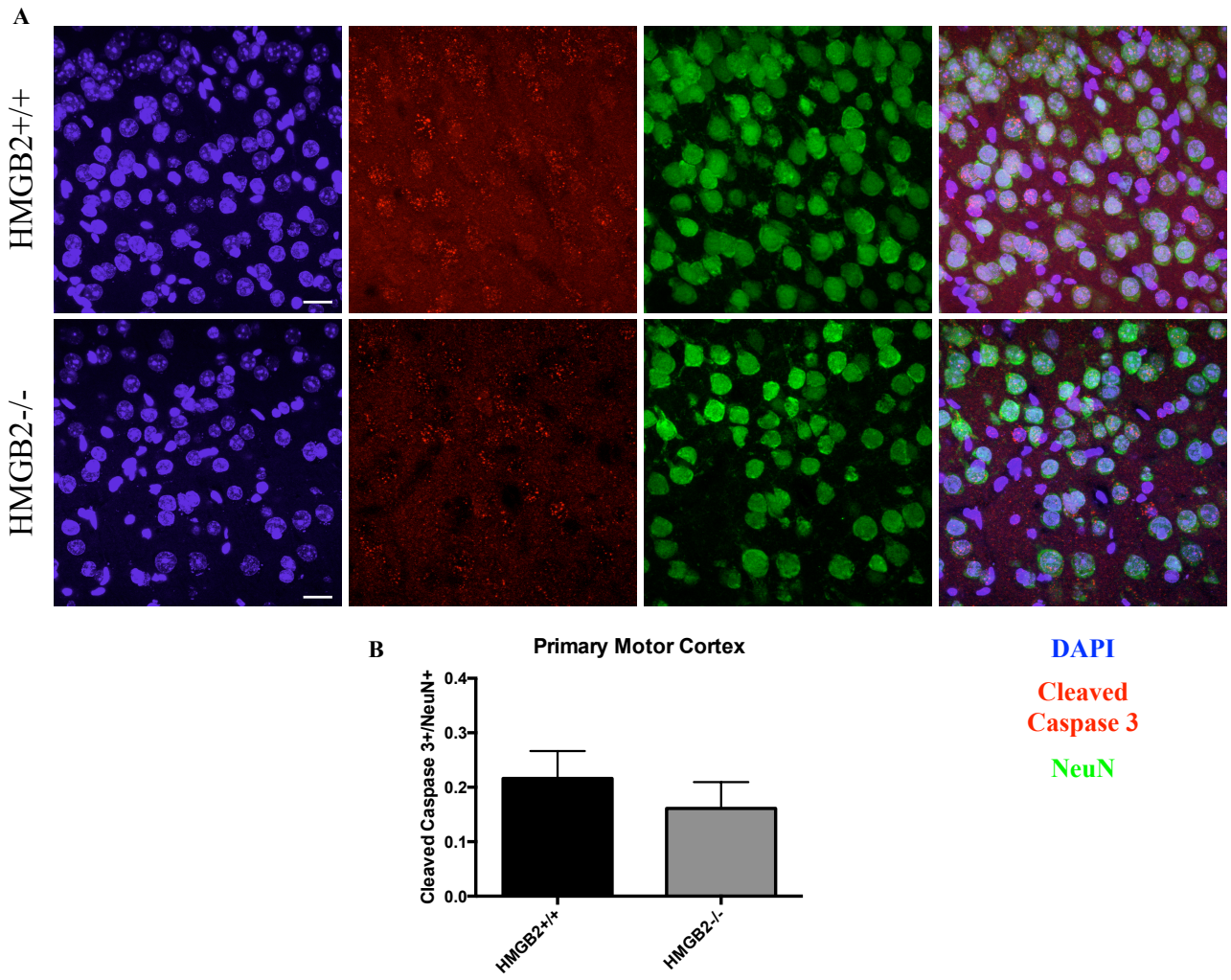
A
HMGB2+/+
HMGB2-/-
B
Primary Motor Cortex
Cleaved Caspase 3+/NeuN+
0.4
0.3
0.2
0.1
0.0
HMGB2+/+
HMGB2-/-
DAPI
Cleaved Caspase 3
NeuN

Figure V-5: Modestly abridged cell death in primary motor cortex of HMGB2 KO mouse after ET-1 stroke. Confocal imaging with 63X objective. **(A)** Comparison of WT and HMGB2-/- brain sections stained for the apoptotic cell death marker cleaved caspase 3 (Red), neuronal marker NeuN (Green), and DAPI (Blue). **(B)** Quantification obtained from six randomly selected 25um Z-stacks per brain section, showing the ratio of cleaved caspase 3+ cells to all NeuN+ neurons. n=3 per genotype.

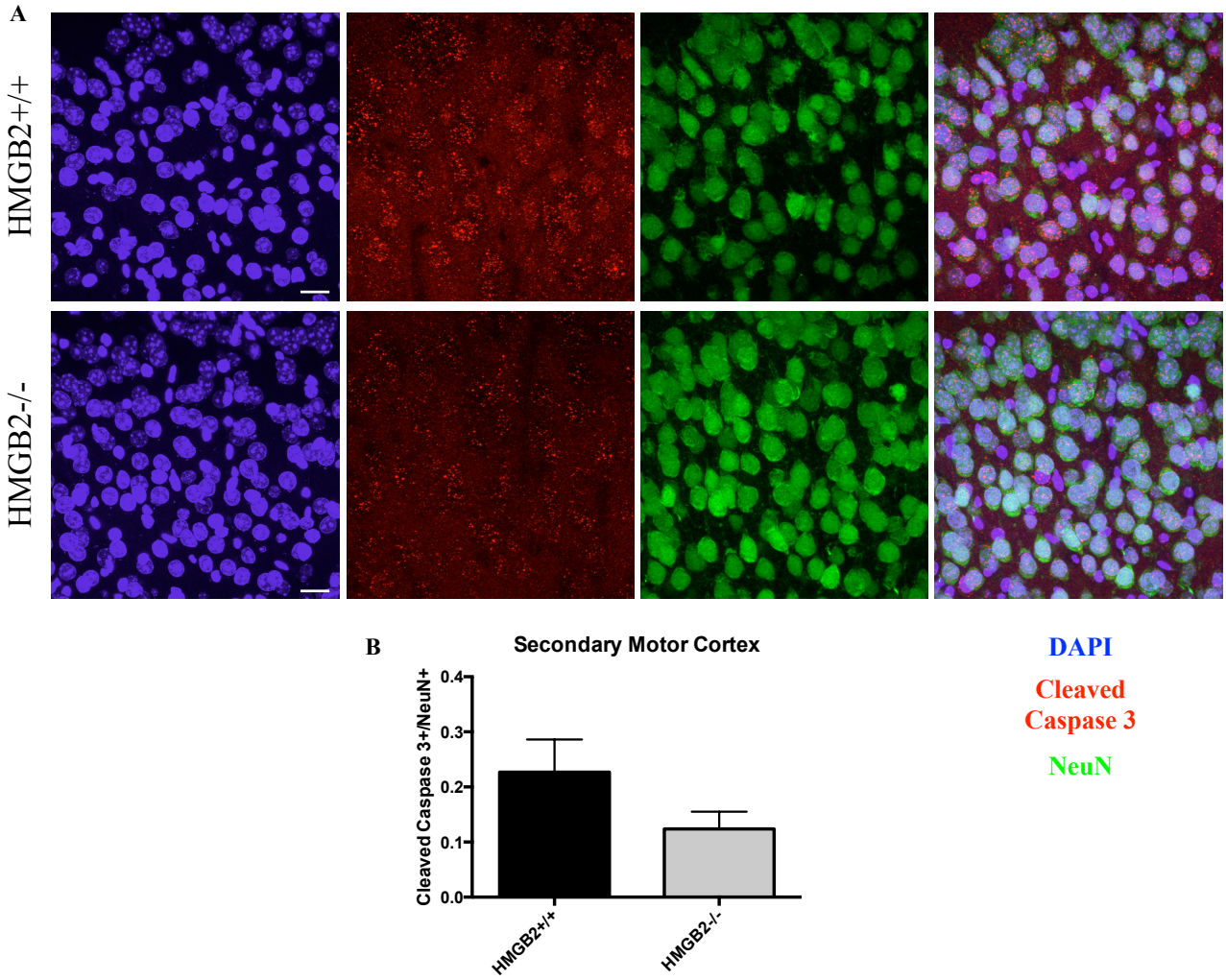
A
HMGB2+/+
HMGB2-/-
B
Secondary Motor Cortex
Cleaved Caspase 3+/NeuN+
0.4
0.3
0.2
0.1
0.0
HMGB2+/+
HMGB2-/-
DAPI
Cleaved Caspase 3
NeuN

Figure V-6: Modestly reduced cell death in secondary motor cortex of HMGB2 KO mouse after ET-1 stroke. Confocal imaging with 63X objective. **(A)** Comparison of WT and HMGB2-/- brain sections stained for the apoptotic cell death marker cleaved caspase 3 (Red), neuronal marker NeuN (Green), and DAPI (Blue). **(B)** Quantification obtained from six randomly selected 25um Z-stacks per brain section, showing the ratio of cleaved caspase 3+ cells to all NeuN+ neurons. n=3 per genotype.

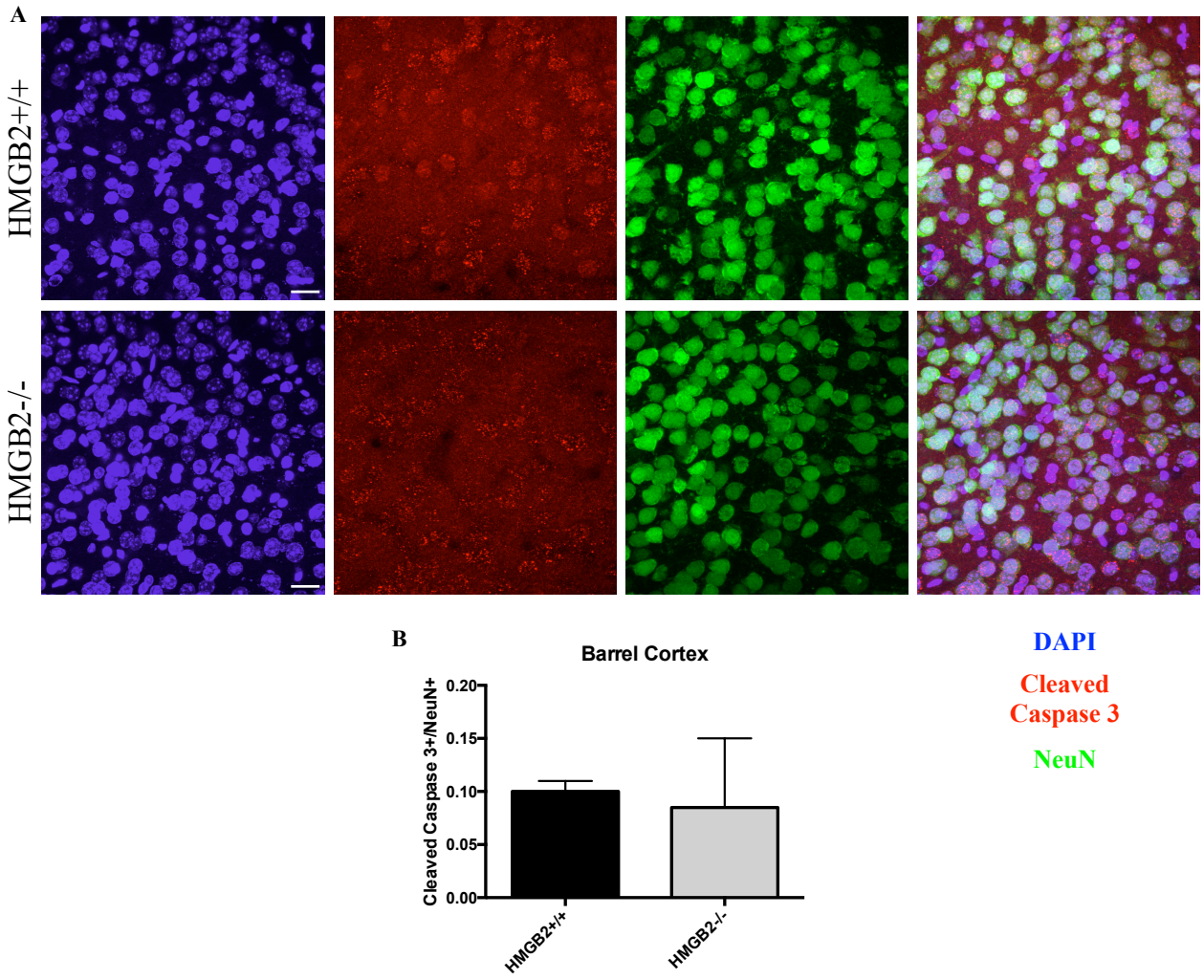
A
HMGB2+/+
HMGB2-/-
B
Barrel Cortex
Cleaved Caspase 3+/NeuN+
0.20
0.15
0.10
0.05
0.00
HMGB2+/+
HMGB2-/-
DAPI
Cleaved Caspase 3
NeuN

Figure V-7: Somatosensory cortex displays no differences in apoptosis between WT and HMGB2 KO mice after ET-1 ischemia. Confocal imaging with 63X objective. **(A)** Comparison of WT and HMGB2-/- brain sections stained for the apoptotic cell death marker cleaved caspase 3 (Red), neuronal marker NeuN (Green), and DAPI (Blue). **(B)** Quantification obtained from six randomly selected 25um Z-stacks per brain section, showing the ratio of cleaved caspase 3+ cells to all NeuN+ neurons. n=3 per genotype.

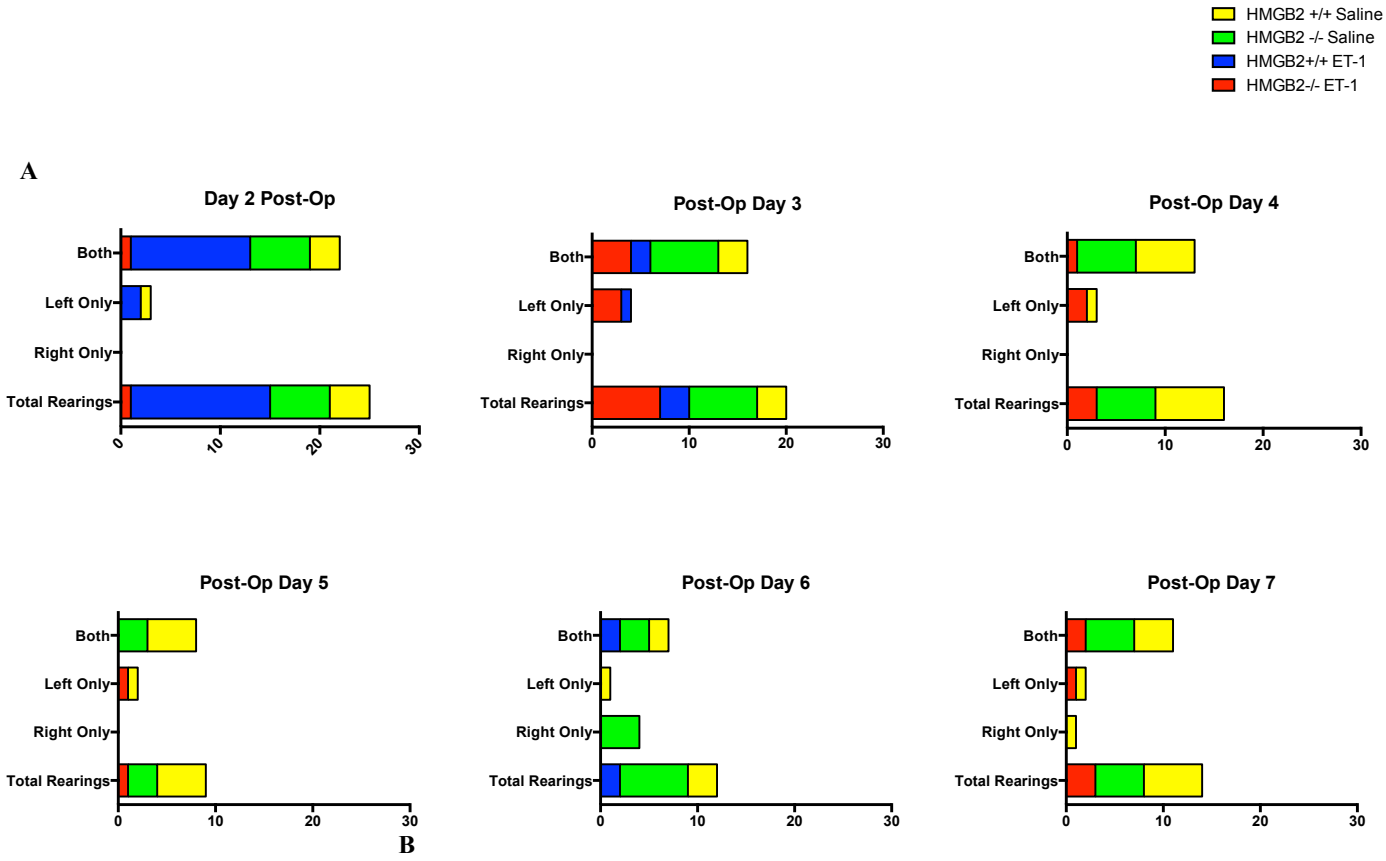
HMGB2 +/+ Saline
HMGB2 -/- Saline
HMGB2+/+ ET-1
HMGB2-/- ET-1
A
Day 2 Post-Op
Post-Op Day 3
Post-Op Day 4
Post-Op Day 5
Post-Op Day 6
Post-Op Day 7
Both
Left Only
Right Only
Total Rearings
0
10
20
30
B

Figure V-8: Reduction in activity/front limb mobility in HMGB2+/+ and HMGB2-/- mice following ET-1 stroke. (A) We video recorded one minute of activity in freely moving mice in their home cages every day from day two to day seven following ET-1/saline injections into the VM thalamus and quantified the number of times the mice reared up on the side of the cage with only the left or right front limbs, or both front limbs. n=2-4 mice per group/genotype.

A

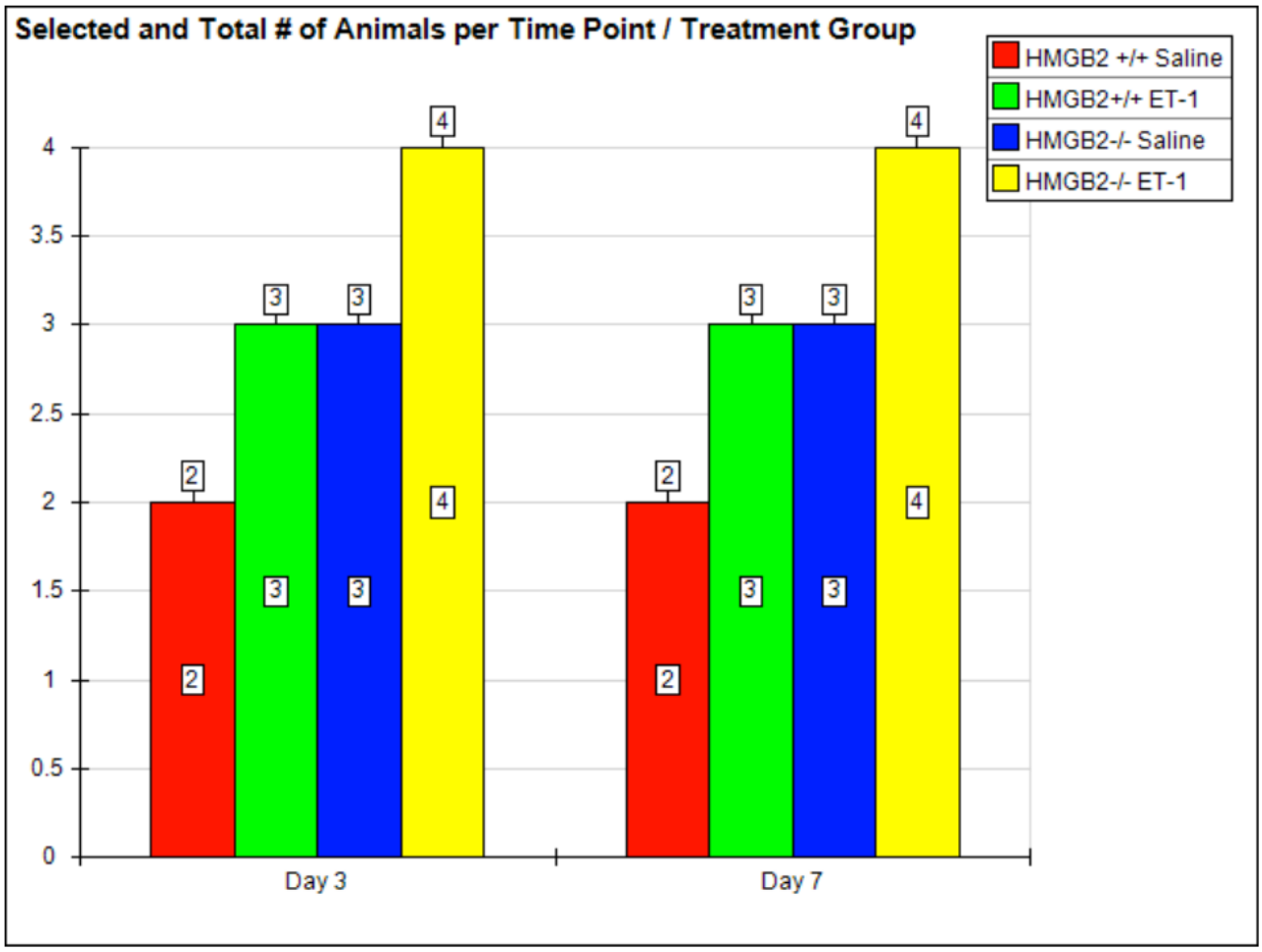
Selected and Total # of Animals per Time Point / Treatment Group
HMGB2 +/+ Saline
HMGB2+/+ ET-1
HMGB2-/- Saline
HMGB2-/- ET-1
4
3.5
3
2.5
2
1.5
1
0.5
0
Day 3
Day 7

Figure V-9: Treatment groups utilized in the Catwalk XT behavioral analyses. **(A)** At day three and day seven the following stereotaxic ET-1 and saline injections into the VM thalamus, the following animals were employed in assessment of front and hind limb biomechanics.

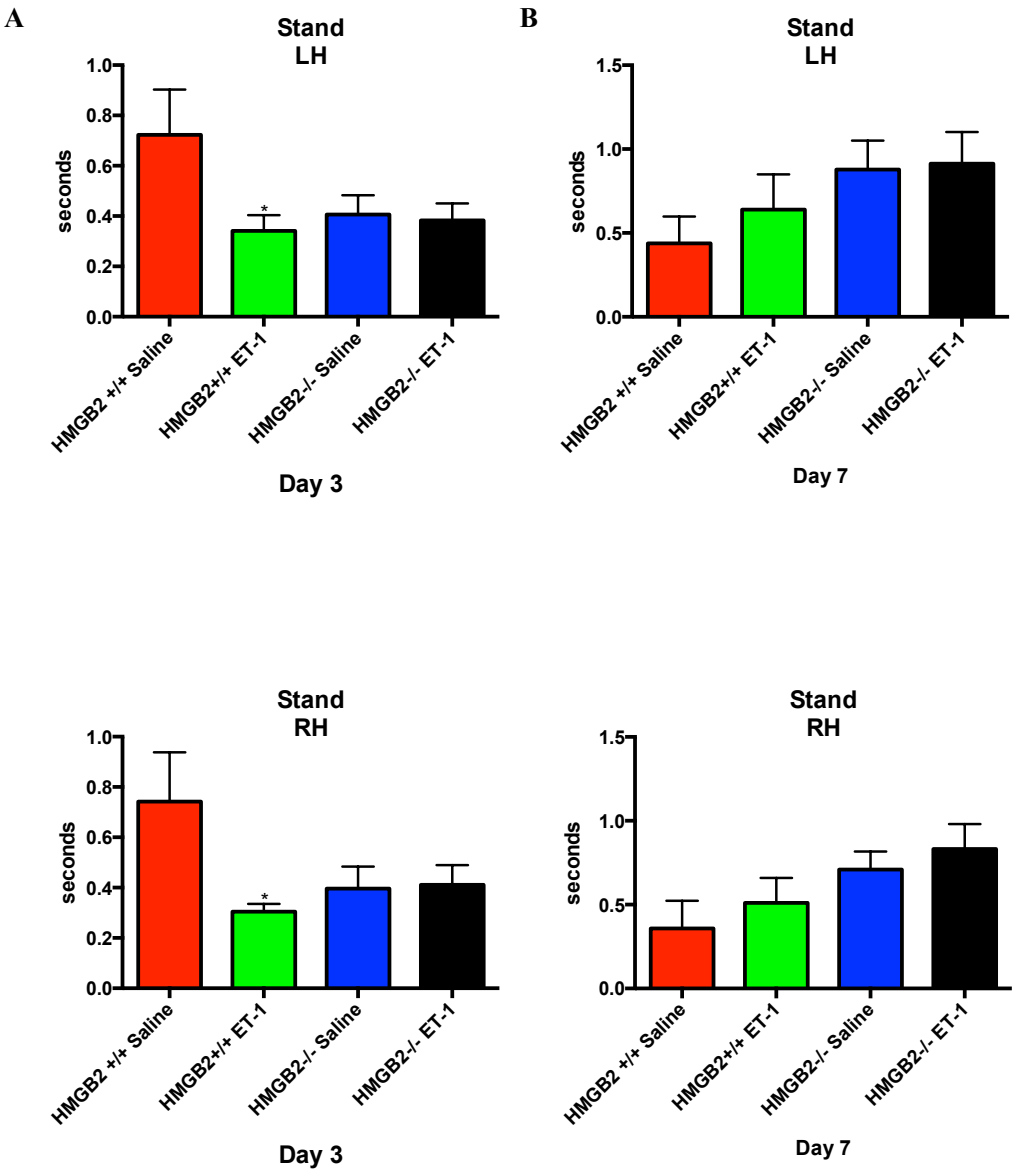
A
Stand
LH
seconds
1.0
0.8
0.6
0.4
0.2
0.0
*
HMGB2 +/+ Saline
HMGB2+/+ ET-1
HMGB2-/- Saline
HMGB2-/- ET-1
Day 3
B
Stand
LH
seconds
1.5
1.0
0.5
0.0
HMGB2 +/+ Saline
HMGB2+/+ ET-1
HMGB2-/- Saline
HMGB2-/- ET-1
Day 7
Stand
RH
seconds
1.0
0.8
0.6
0.4
0.2
0.0
*
HMGB2 +/+ Saline
HMGB2+/+ ET-1
HMGB2-/- Saline
HMGB2-/- ET-1
Day 3
Stand
RH
seconds
1.5
1.0
0.5
0.0
HMGB2 +/+ Saline
HMGB2+/+ ET-1
HMGB2-/- Saline
HMGB2-/- ET-1
Day 7

Figure V-10: Altered stand characteristics in hind limbs of WT mice, but not HMGB2-/- mice, following thalamic ischemia. (A) The time in seconds of paw contact with the glass device surface across all four treatment groups at three days following ET-1 stroke induction. **(B)** The time in seconds of paw contact with the glass device surface across all four treatment groups at seven days following ET-1 stroke induction. n=2-4 per genotype and experimental group. Holm-Sidak's post-hoc multiple comparisons test. *Left Hind Limb WT Mean Difference 0.3814 *Right Hind Limb WT Mean Difference 0.4369

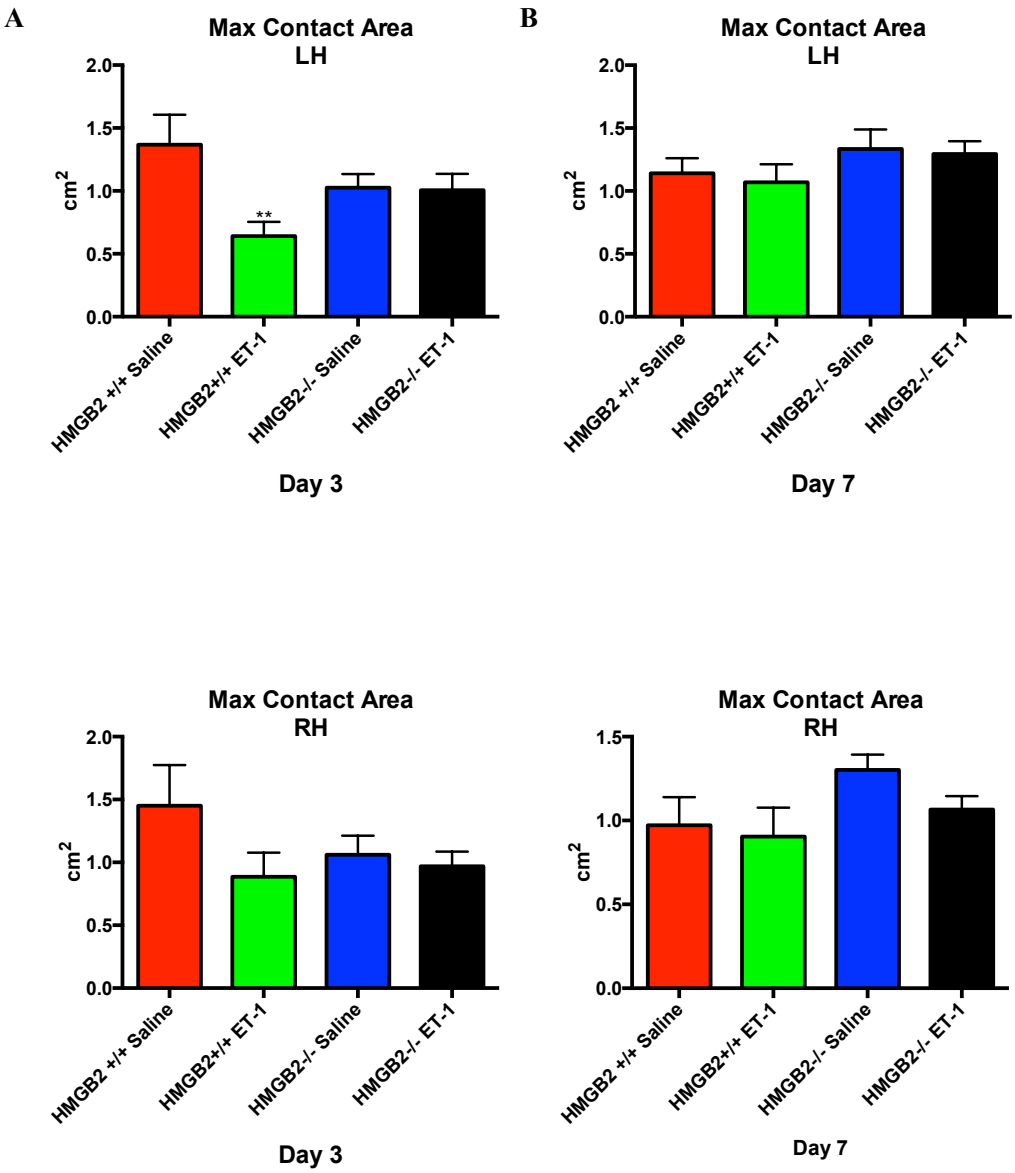
A
Max Contact Area
LH
2.0
1.5
1.0
0.5
0.0
cm2
**
HMGB2 +/+ Saline
HMGB2+/+ ET-1
HMGB2-/- Saline
HMGB2-/- ET-1
Day 3
B
Max Contact Area
LH
2.0
1.5
1.0
0.5
0.0
cm2
HMGB2 +/+ Saline
HMGB2+/+ ET-1
HMGB2-/- Saline
HMGB2-/- ET-1
Day 7
Max Contact Area
RH
2.0
1.5
1.0
0.5
0.0
cm2
HMGB2 +/+ Saline
HMGB2+/+ ET-1
HMGB2-/- Saline
HMGB2-/- ET-1
Day 3
Max Contact Area
RH
1.5
1.0
0.5
0.0
cm2
HMGB2 +/+ Saline
HMGB2+/+ ET-1
HMGB2-/- Saline
HMGB2-/- ET-1
Day 7

Figure V-11: Reduction in max contact area of hind limbs in WT mice, but not HMGB2-/- mice, following thalamic ischemia. (A) A calculation of the maximum area of the paw coming into contact with the glass plate across all four treatment groups at three days following ET-1 stroke induction. **(B)** A calculation of the maximum area of the paw coming into contact with the glass plate across all four treatment groups at seven days following ET-1 stroke induction. n=2-4 per genotype and experimental group. Holm-Sidak's post-hoc multiple comparisons test. **Left Hind Limb WT Mean Difference 0.7261

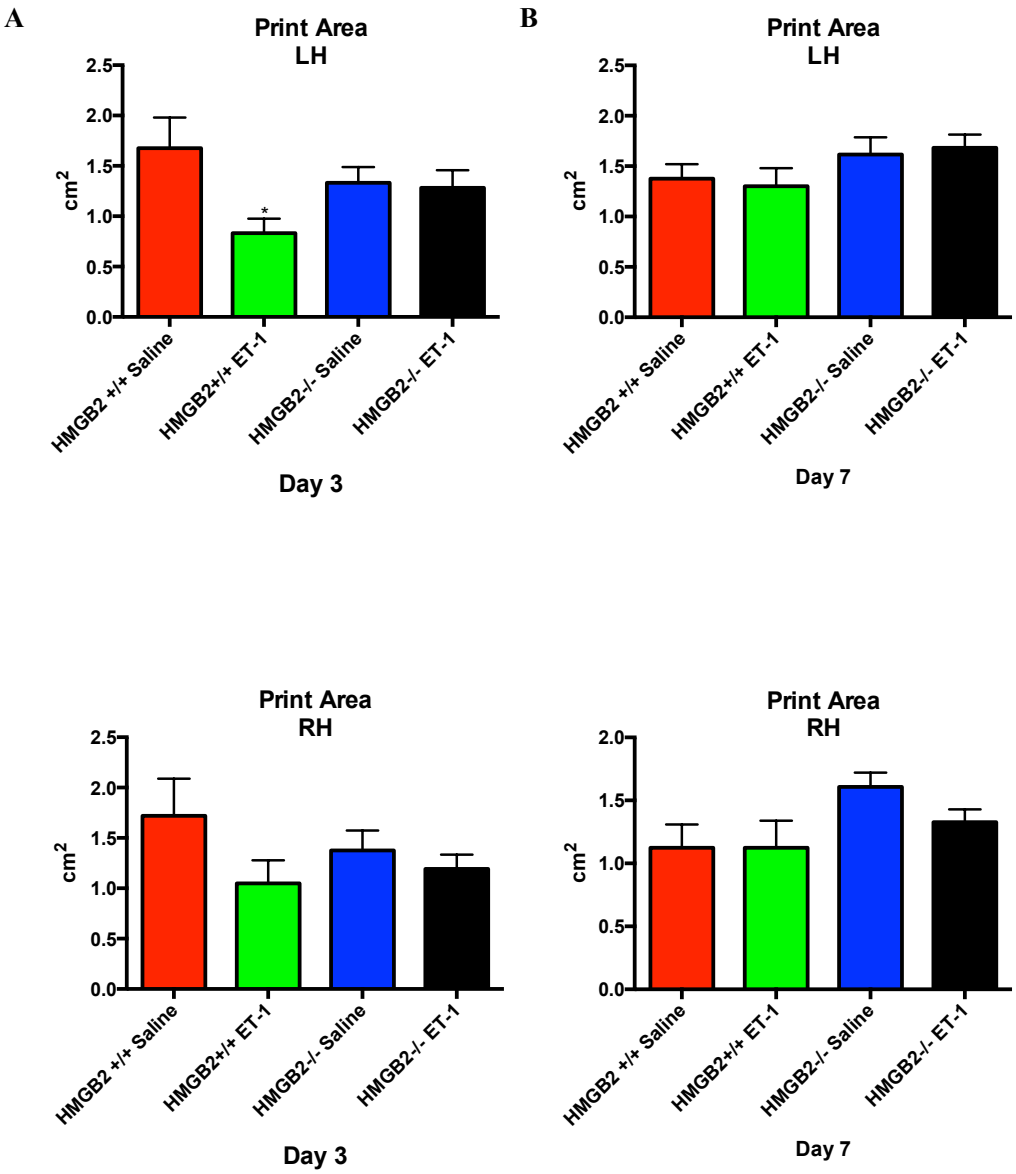
A
Print Area
LH
2.5
2.0
1.5
1.0
0.5
0.0
cm2
*
HMGB2 +/+ Saline
HMGB2+/+ ET-1
HMGB2-/- Saline
HMGB2-/- ET-1
Day 3
B
Print Area
LH
Day 7
Print Area
RH
Day 3
Print Area
RH
Day 7

Figure V-12: Reduction in print area of hind limbs in WT mice, but not HMGB2-/- mice, following thalamic ischemia. (A) The surface area of the entire mouse print on the glass surface across all four treatment groups at three days following ET-1 stroke induction. **(B)** The surface area of the entire mouse print on the glass surface across all four treatment groups at seven days following ET-1 stroke induction. n=2-4 per genotype and experimental group. Holm-Sidak's post-hoc multiple comparisons test. *Left Hind Limb WT Mean Difference 0.8443

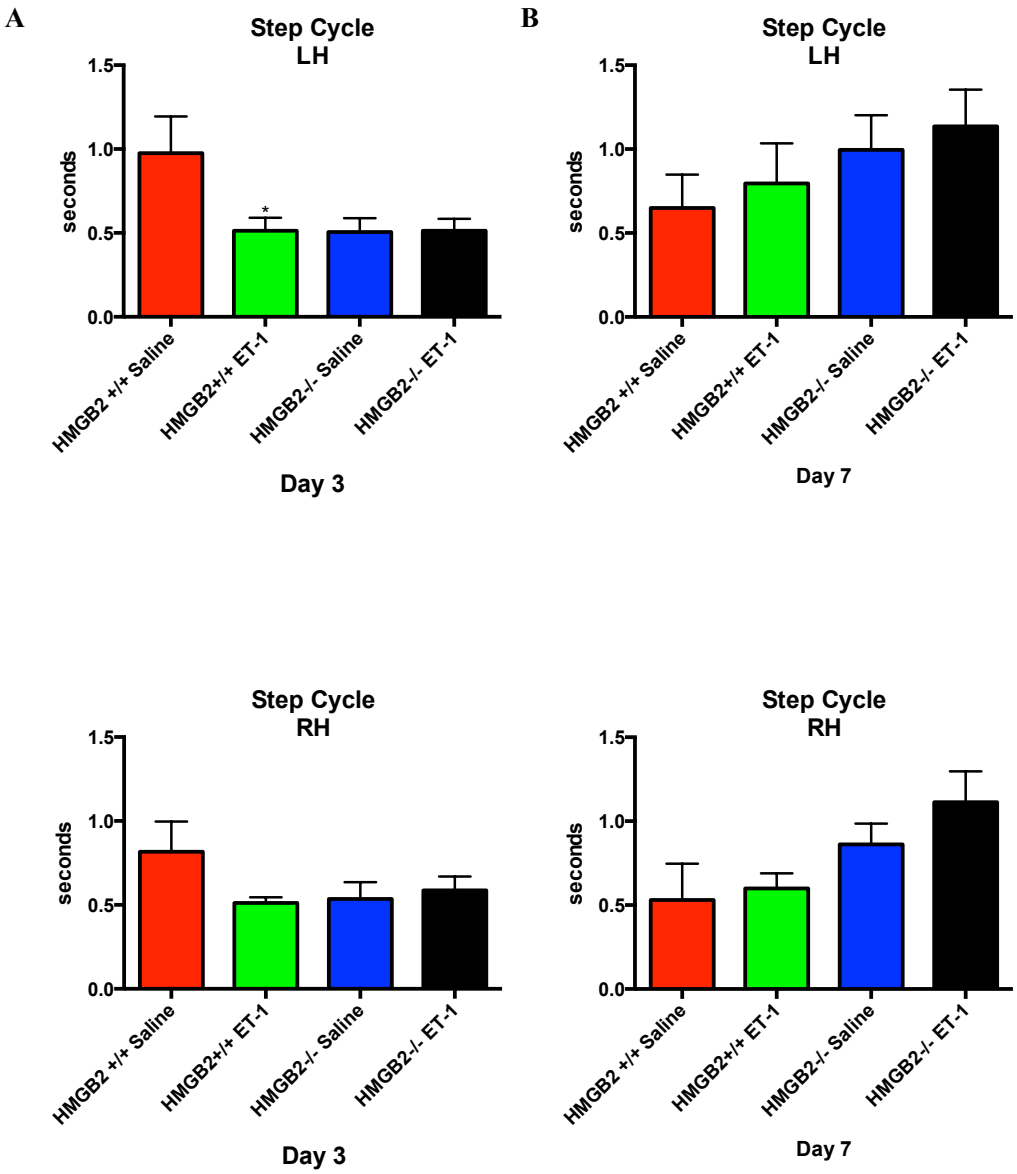
A
Step Cycle
LH
seconds
1.5
1.0
0.5
0.0
*
HMGB2 +/+ Saline
HMGB2+/+ ET-1
HMGB2-/- Saline
HMGB2-/- ET-1
Day 3
B
Step Cycle
LH
seconds
1.5
1.0
0.5
0.0
HMGB2 +/+ Saline
HMGB2+/+ ET-1
HMGB2-/- Saline
HMGB2-/- ET-1
Day 7
Step Cycle
RH
seconds
1.5
1.0
0.5
0.0
HMGB2 +/+ Saline
HMGB2+/+ ET-1
HMGB2-/- Saline
HMGB2-/- ET-1
Day 3
Step Cycle
RH
seconds
1.5
1.0
0.5
0.0
HMGB2 +/+ Saline
HMGB2+/+ ET-1
HMGB2-/- Saline
HMGB2-/- ET-1
Day 7

Figure V-13: Reduction in the step cycle of hind limbs in WT mice, but not HMGB2-/- mice, following thalamic ischemia. (A) Measurement of time between two consecutive initial contacts, with the glass plate, of the same paw across all four treatment groups at three days following ET-1 stroke induction. **(B)** Measurement of time between two consecutive initial contacts, with the glass plate, of the same paw across all four treatment groups at seven days following ET-1 stroke induction. n=2-4 per genotype and experimental group. Holm-Sidak's post-hoc multiple comparisons test. *Left Hind Limb WT Mean Difference 0.4626

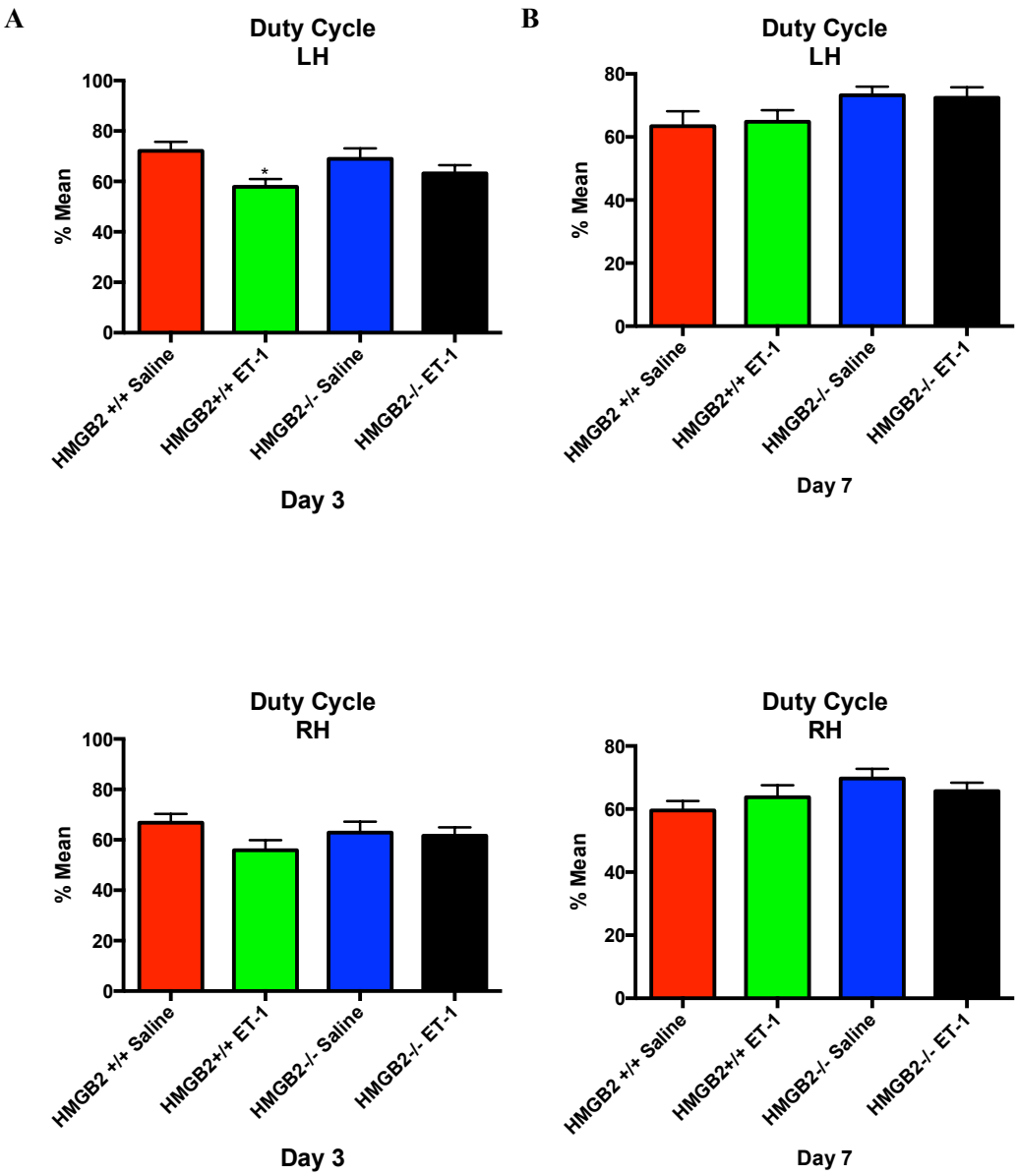
A
Duty Cycle
LH
% Mean
100
80
60
40
20
0
*
HMGB2 +/+ Saline
HMGB2+/+ ET-1
HMGB2-/- Saline
HMGB2-/- ET-1
Day 3
B
Duty Cycle
LH
% Mean
80
60
40
20
0
HMGB2 +/+ Saline
HMGB2+/+ ET-1
HMGB2-/- Saline
HMGB2-/- ET-1
Day 7
Duty Cycle
RH
% Mean
100
80
60
40
20
0
HMGB2 +/+ Saline
HMGB2+/+ ET-1
HMGB2-/- Saline
HMGB2-/- ET-1
Day 3
Duty Cycle
RH
% Mean
80
60
40
20
0
HMGB2 +/+ Saline
HMGB2+/+ ET-1
HMGB2-/- Saline
HMGB2-/- ET-1
Day 7

Figure V-14: Reduction in the duty cycle of hind limbs in WT mice, but not HMGB2-/- mice, following thalamic ischemia. (A) A percentage of the step cycle divided by stand + swing of the paws across all four treatment groups at three days following ET-1 stroke induction. **(B)** A percentage of the step cycle divided by stand + swing of the paws across all four treatment groups at seven days following ET-1 stroke induction. n=2-4 per genotype and experimental group. Holm-Sidak's post-hoc multiple comparisons test. **Left Hind Limb WT Mean Difference 14.26

A

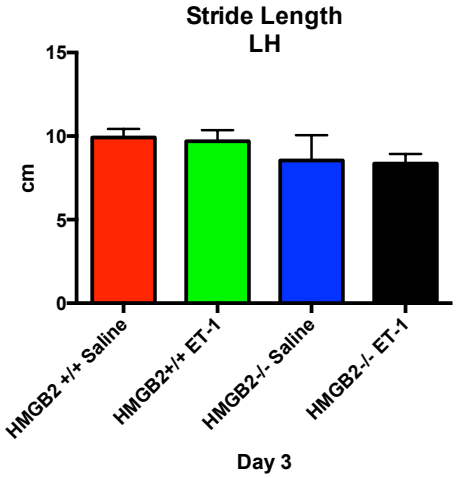
Stride Length
LH
15
10
5
0
cm
HMGB2 +/+ Saline
HMGB2+/+ ET-1
HMGB2-/- Saline
HMGB2-/- ET-1
Day 3

B

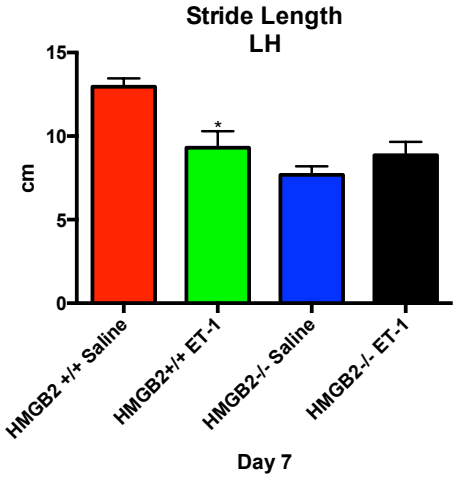
Stride Length
LH
15
10
5
0
cm
*
HMGB2 +/+ Saline
HMGB2+/+ ET-1
HMGB2-/- Saline
HMGB2-/- ET-1
Day 7

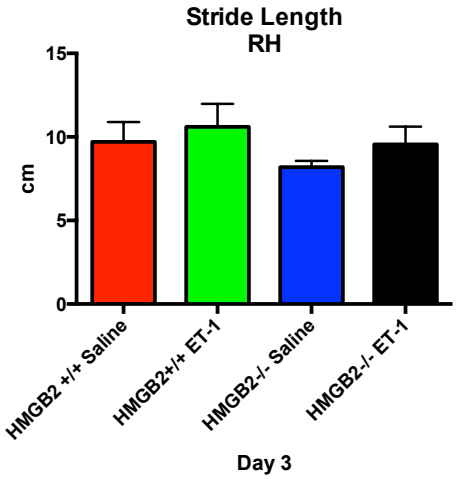
Stride Length
RH
15
10
5
0
cm
HMGB2 +/+ Saline
HMGB2+/+ ET-1
HMGB2-/- Saline
HMGB2-/- ET-1
Day 3

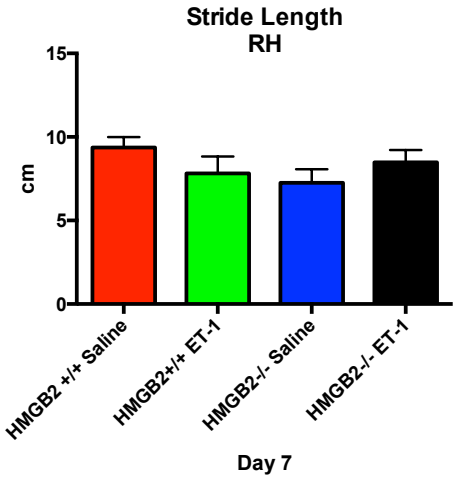
Stride Length
RH
15
10
5
0
cm
HMGB2 +/+ Saline
HMGB2+/+ ET-1
HMGB2-/- Saline
HMGB2-/- ET-1
Day 7

Figure V-15: Reduction in the stride length of hind limbs in WT mice, but not HMGB2-/- mice, following thalamic ischemia. (A) The distance between consecutive placement of the same paws across all four treatment groups at three days following ET-1 stroke induction. **(B)** The distance between consecutive placement of the same paws across all four treatment groups at seven days following ET-1 stroke induction. n=2-4 per genotype and experimental group. Holm-Sidak's post-hoc multiple comparisons test. *Left Hind Limb WT Mean Difference 3.644

Chapter VI

General Conclusions and Future Directions

Conclusions

HMGB2 maintains numerous roles in the physiological and pathological murine CNS, from acting on the gene expression patterns of key epigenetic modulators, to maintaining robust and fully functional apoptotic cell signalling pathways.

What are the effector pathway changes in the adult murine SVZ following genetic ablation of HMGB2 and what is the consequence of such alterations?

Following a shotgun proteomics screen comparison of SVZ wholemount tissue from adult HMGB2+/+ and HMGB2-/- mice, a number of important molecular players were identified that are altered in the HMGB2 KO animals. Factors upregulated in the SVZ of the HMGB KO mouse cluster rationally alongside WT, except in a cluster enriched for migratory and synaptic proteins such as CamkII, L1Cam and NCAM. This greater propensity for expression of such factors points to potentially altered cell cycle dynamics in the NSPCs which serve as the foundation and glue of the SVZ niche. NCAM is a molecule critical to extracellular signalling as well as migration of NSCs; significant increases in NCAM 140, which is an isoform specifically expressed on neuroblasts and immature neurons (Abraham et al., 2013b), were documented. In addition changes in Oct4, a transcription factor present in ESCs and NSCs and critical to the maintenance of stem cell pluripotency, were evident: a reduction in protein levels with concomitant changes in its upstream signalling partner pAkt (Campbell and Rudnicki, 2013b). In addition, the levels of the tumor suppressor protein p21 were quantified in HMGB2-/- SVZ tissue extracts and were found to be slightly increased (Abraham et al., 2013b; Lian

et al., 2012; Molofsky et al., 2005). Altogether these changes point to an SVZ stem cell compartment with altered cell cycle/differentiation dynamics in the adult HMGB2-/- mouse CNS.

Does the global absence of HMGB2 affect perinatal SVZ neurogenesis?

It has been demonstrated that epigenetic modifiers can have profound effects on the fate transitions of cell including NSCs in the perinatal SVZ (Egan et al., 2013a; Hirabayashi et al., 2009a; Hwang et al., 2014; Ming and Song, 2011). Considering the role ascribed to mammalian HMGB2 and its homologs, we sought to determine whether the global genetic deletion of HMGB2 affects the stereotypic neurogenesis to gliogenesis fate transitions perinatally, and which molecular players potentially drive those differences in a cell culture NSC monolayer model. We identified that the key PcG gene EED is significantly downregulated during NSC differentiation, with a subsequent reduction in the repressive histone mark H3K27me3. EED is critically important for catalyzing this methylation modification, especially affecting the HMGB2-/- cells. These changes were accompanied by greater numbers of neuronal cells being present in the HMGB2-/- cultures at day seven of differentiation as compared with HMGB+/+. It has recently been demonstrated that reducing levels of the gene EED and thereby the accompanying PcG core subunit it encodes prolongs neurogenesis, and delays gliogenesis, and indeed we also observed a leveling out of astrocyte differentiation at day seven and a significant reduction in oligodendrocyte differentiation (Egan et al., 2013b; Sparmann et al., 2013b; Testa,

2011). Therefore it seems reasonable to consider that HMGB2 absence in NSCs, and the subsequent downregulation of EED gene expression can have similar downstream effects on perinatal cell fate choice. A number of other epigenetic factors can also be contributors to this overall process such as DNMT complexes and trxG elements, which together constitute major drivers of mammalian neurogenesis (Gabriel Gonzales-Roybal, 2013).

Can ET-1 be used as a reliable model of thalamic stroke and are there different stroke responses between the HMGB2+/+ and HMGB2-/- genotypes?

We have characterized cellular and histologically ET-1 driven VM thalamic ischemia, which can robustly model lacunar infarcts common in the human thalamus (Bailey et al., 2009). ET-1 thalamic stroke in the WT mouse presents as a dense core accompanied by a prominent hypoperfused penumbra, as well as considerable astrogliosis and microgliosis common to other murine stroke models (Bailey et al., 2009) (Fig. 17). Considerable apoptotic neuronal cell death in the primary and secondary motor cortices of ET-1 injected HMGB2+/+ mice is blunted in the HMGB2-/- animals, pointing to potentially augmented apoptotic signalling given the role HMGB2 serves in the CNS as a potent DAMP (Hock et al., 2007). In addition we have uncovered that HMGB2+/+ animals display significantly altered left hind limb biomechanics following ET-1 injections into the ipsilateral VM thalamus, and this effect is not seen in the HMGB2-/- genotype (Chen et al., 2014). In totality, HMGB2 may serve to underpin the normal physiological response to ischemic brain injury through its toll-like receptor signalling and

DAMP functions, and the absence of these signalling partners could confer the molecular and behavioral phenotype we have uncovered in our experiments.

Future Directions

Determining a precise epigenetic role for HMGB2 in perinatal NSCs.

Although we have demonstrated that germline loss of HMGB2 can have profound effects on the biology of perinatal SVZ stem cells, in the future this project aims to uncover the precise functioning of HMGB2 in the epigenetic NSC landscape. In Chapter IV we outlined changes in the repressive histone mark H3K27me3 is total NSC lysates from a monolayer cell culture preparation, however this analysis only demonstrates the global levels of this histone modification – at all genomic loci. In the future we will perform native chromatin immunoprecipitation (nChIP) (Orsi et al., 2015; 2014b) at specific loci affiliated with the transition from neurogenesis to gliogenesis such as: STAT1, STAT3, GFAP, NEUROG1 – since epigenetic repression or facilitation at their gene promoters drives this critical transition (Burney et al., 2013; Gabriel Gonzales-Roybal, 2013; Juliandi et al., 2010; Ma et al., 2010). The precise DNA localization, of the specific histone modifications we looked at globally, is critical since their abundance within the promoter/transcription start site (TSS), the gene body, or the transcription termination site (TTS) can have dramatically different effects on gene regulation – therefore we will design our nChIP primers in the future to fully encapsulate all of these genetic elements (Black et al., 2012; Shen et al., 2009). In addition, as we indicated in the introduction, the *Drosophila* HMGB2 homolog DSP1 acts not in the control of the gene

expression patterns of key PcG complex genes but physically recruits PcG complexes to chromatin where they can silence key developmental gene expression programs, for instance those critical to position-effect variegation (Decoville et al., 2001; Déjardin et al., 2005; Janke et al., 2003; Lanzuolo and Orlando, 2012; Ringrose and Paro, 2007). We have generated and expressed his-tagged recombinant mouse HMGB2 proteins and will employ these in pull-down assays with nuclear lysates from perinatal NSCs cell culture preps in an effort to potentially uncover possible physical interactions between HMGB2 and PcG core subunits and complexes such as PRC1 and PRC2 and its member proteins (EED, SUZ12, BMI1, EZH2, CBX3/4, RING1B, RING1A). Due to the fact that we employ a germline HMGB2 KO model, where compensation from other HMG(B) family members may blunt the effect its loss has on perinatal NSCs, we would like to perform the above analyses following *in-utero* electroporation of short-hairpin RNAs targeting HMGB2 in the VZ of WT mice just before the onset of astrogliogenesis, around embryonic day 17.5 (Ishino et al., 2014; Kusek et al., 2012). This acute knock-down of HMGB2 may amplify the changes we see in the fate transitions of perinatal NSCs. Finally, following on the heels of these additional acute knockdown experiments we will assess the *in-vivo* effects by looking for potential differences in early postnatal cortical development and gliogenesis using layer specific markers such as Cux1, Satb1 and Tbr1 as well as glial markers such as S100B and CC1. In totality, these additional experiments should provide us with ample evidence as to which epigenetic cog HMGB2 fits within (Bukhari et al., 2011; Close et al., 2012; Cubelos et al., 2010; Englund et al., 2005; Raponi et al., 2007).

How does ET-1 induced VM thalamic ischemia modulate microglial activation states in HMGB2-/- mice?

We have demonstrated a modified apoptotic cell death program in the primary and secondary motor cortices of HMGB2-/- mice following ischemic lesion of the VM thalamus (Fig. 21-22). Given the role HMGB2 serves as a DAMP in the CNS and periphery, in the future we would like to assess the microglial response to ET-1 stroke within the thalamus, as well as any areas VM thalamus sends strong projections (feedback and feed forward) (Lee et al., 2014). To accomplish this, seven and fourteen days following stereotaxic injection of ET-1 into the VM thalamus we will perform immunofluorescence for the microglial M1 and M2 markers, indicating classically and alternatively activated states respectively – with the M1/M2 ratio being the final readout of how HMGB2 loss affects microglial polarization (Mikita et al., 2011; Wu et al., 2012). In addition, since VM thalamic projections to primary and secondary motor cortices target both GABAergic and glutamatergic neuronal populations we can assess at what ratio neuronal death, following ET-1 ischemia, occurs within the inhibitory or excitatory classes of cortical neurons and if this is at all modified in the HMGB2-/- animals(Dufour et al., 2003; Janz and Illing, 2014). Finally, given the specific changes we observed in left hind limb biomechanics following ET-1 stroke in the thalamus, we will include a number of other behavioral measures, such as the rotorod and pasta matrix reaching test, which together will provide a fuller picture of the strength and dexterity effects of lacunar ischemia in the VM thalamus across both genotypes (Jeljeli et al., 2003; Tennant and Jones, 2009).

Abraham, A.B., Bronstein, R., Chen, E.I., Koller, A., Ronfani, L., Maletic-Savatic, M., and Tsirka, S.E. (2013a). Members of the high mobility group B protein family are dynamically expressed in embryonic neural stem cells. Proteome Sci *11*, 18.

Abraham, A.B., Bronstein, R., Reddy, A.S., Maletic-Savatic, M., Aguirre, A., and Tsirka, S.E. (2013b). Aberrant Neural Stem Cell Proliferation and Increased Adult Neurogenesis in Mice Lacking Chromatin Protein HMGB2. PLoS ONE *8*, e84838.

Aguirre, A.A., Chittajallu, R., Belachew, S., and Gallo, V. (2004). NG2-expressing cells in the subventricular zone are type C-like cells and contribute to interneuron generation in the postnatal hippocampus. J Cell Biol *165*, 575–589.

Akers, K.G., Martinez-Canabal, A., Restivo, L., Yiu, A.P., De Cristofaro, A., Hsiang, H.-L.L., Wheeler, A.L., Guskjolen, A., Niibori, Y., Shoji, H., et al. (2014). Hippocampal neurogenesis regulates forgetting during adulthood and infancy. Science *344*, 598–602.

Aloia, L., Di Stefano, B., and Di Croce, L. (2013). Polycomb complexes in stem cells and embryonic development. Development *140*, 2525–2534.

Altman, J. (1962). Are New Neurons Formed in the 'Brains Of Adult Mammals?

. Science *135*, 1127–1128.

Altman, J. (1963). Autoradiographic Investigation of Cell Proliferation in the Brains of Rats and Cats. The Anatomical Record *145*, 573–591.

Altman, J., and Bayer, S. (1975). Postnatal Development of the Hippocampal Dentate Gyrus Under Normal and Experimental Conditions. The Hippocampus *1*, 95–122.

Altman, J., and Das, G. (1965). Autoradiographic and Histological Evidence of Postnatal Hippocampal Neurogenesis in Rats. J Comp Neurol *124*, 319–335.

Alvarez-Buylla, A., and Doetsch, F. (1999). Subventricular Zone Astrocytes Are Neural Stem Cells in the Adult Mammalian Brain. 1–14.

Ansari, S., Azari, H., McConnell, D.J., Afzal, A., and Mocco, J. (2011). Intraluminal middle cerebral artery occlusion (MCAO) model for ischemic stroke with laser doppler flowmetry guidance in mice. J Vis Exp.

Atchison, M.L. (2014). Function of YY1 in Long-Distance DNA Interactions. Front Immunol *5*, 45.

Bacigaluppi, M., Pluchino, S., Jametti, L.P., Kilic, E., Kilic, U., Salani, G., Brambilla, E., West, M.J., Comi, G., Martino, G., et al. (2009). Delayed post-ischaemic neuroprotection following systemic neural stem cell transplantation involves multiple mechanisms. Brain *132*, 2239–2251.

Bailey, E.L., McCulloch, J., Sudlow, C., and Wardlaw, J.M. (2009). Potential animal models of lacunar stroke: a systematic review. Stroke *40*, e451–e458.

Basu, A., Wilkinson, F.H., Colavita, K., Fennelly, C., and Atchison, M.L. (2013). YY1 DNA binding and interaction with YAF2 is essential for Polycomb recruitment. Nucleic Acids Res.

Bennett, L., Yang, M., Enikolopov, G., and Iacovitti, L. (2009). Circumventricular organs: A novel site of neural stem cells in the adult brain. Molecular and Cellular ….

Black, J.C., Van Rechem, C., and Whetstine, J.R. (2012). Histone Lysine Methylation Dynamics: Establishment, Regulation, and Biological Impact. Mol Cell *48*, 491–507.

Blasi, F., Wei, Y., Balkaya, M., Tikka, S., Mandeville, J.B., Waeber, C., Ayata, C., and Moskowitz, M.A. (2014). Recognition memory impairments after subcortical white matter stroke in mice. Stroke *45*, 1468–1473.

Bolborea, M., and Dale, N. (2013). Hypothalamic tanycytes: potential roles in the control of feeding and energy balance. Trends Neurosci.

Borrell, V., Cárdenas, A., Ciceri, G., Galcerán, J., Flames, N., Pla, R., Nóbrega-Pereira, S., García-Frigola, C., Peregrín, S., Zhao, Z., et al. (2012). Slit/Robo signaling modulates the proliferation of central nervous system progenitors. Neuron *76*, 338–352.

Boutin, C., Schmitz, B., Cremer, H., and Diestel, S. (2009). NCAM expression induces neurogenesis in vivo. European Journal of Neuroscience *30*, 1209–1218.

Bukhari, N., Torres, L., Robinson, J.K., and Tsirka, S.E. (2011). Axonal regrowth after spinal cord injury via chondroitinase and the tissue plasminogen activator (tPA)/plasmin system. Journal of Neuroscience *31*, 14931–14943.

Burney, M.J., Johnston, C., Wong, K.-Y., Teng, S.-W., Beglopoulos, V., Stanton, L.W., Williams, B.P., Bithell, A., and Buckley, N.J. (2013). An epigenetic signature of developmental potential in neural stem cells and early neurons. Stem Cells *31*, 1868–1880.

Campbell, P.A., and Rudnicki, M.A. (2013a). Oct4 Interaction with Hmgb2 Regulates Akt Signaling and Pluripotency - Campbell - 2013 - STEM CELLS - Wiley Online Library. Stem Cells.

Campbell, P.A., and Rudnicki, M.A. (2013b). Oct4 Interaction with Hmgb2 Regulates Akt Signaling and Pluripotency. Stem Cells.

Cao, Q., Wang, X., Zhao, M., Yang, R., Malik, R., Qiao, Y., Poliakov, A., Yocum, A.K., Li, Y., Chen, W., et al. (2014). The central role of EED in the orchestration of

polycomb group complexes. Nat Comms *5*.

Carmichael, S.T. (2005). Rodent models of focal stroke: size, mechanism, and purpose. NeuroRx *2*, 396–409.

Carrera, E., Caplan, L.R., and Michel, P. (2012). Stroke Syndromes, 3ed - Google Books. Stroke Syndromes.

Chen, E.I., McClatchy, D., Park, S.K., and Yates, J.R. (2008). Comparisons of mass spectrometry compatible surfactants for global analysis of the mammalian brain proteome. Anal. Chem. *80*, 8694–8701.

Chen, Y.-J., Cheng, F.-C., Sheu, M.-L., Su, H.-L., Chen, C.-J., Sheehan, J., and Pan, H.-C. (2014). Detection of subtle neurological alterations by the Catwalk XT gait analysis system. J Neuroeng Rehabil *11*, 62.

Cheng, M.-F. (2013). Hypothalamic neurogenesis in the adult brain. Front Neuroendocrinol *34*, 167–178.

Chiang, C.-Y., Sheu, M.-L., Cheng, F.-C., Chen, C.-J., Su, H.-L., Sheehan, J., and Pan, H.-C. (2014). Comprehensive analysis of neurobehavior associated with histomorphological alterations in a chronic constrictive nerve injury model through use of the CatWalk XT system. J. Neurosurg. *120*, 250–262.

Clascá, F.F., Rubio-Garrido, P.P., and Jabaudon, D.D. (2012). Unveiling the diversity of thalamocortical neuron subtypes. Eur. J. Neurosci. *35*, 1524–1532.

Close, J., Xu, H., De Marco Garcia, N., Batista-Brito, R., Rossignol, E., Rudy, B., and Fishell, G. (2012). Satb1 Is an Activity-Modulated Transcription Factor Required for the Terminal Differentiation and Connectivity of Medial Ganglionic Eminence-Derived Cortical Interneurons. Journal of Neuroscience *32*, 17690–17705.

Covacu, R., Perez Estrada, C., Arvidsson, L., Svensson, M., and Brundin, L. (2014). Change of fate commitment in adult neural progenitor cells subjected to chronic inflammation. Journal of Neuroscience *34*, 11571–11582.

Cruikshank, S.J., Ahmed, O.J., Stevens, T.R., Patrick, S.L., Gonzalez, A.N., Elmaleh, M., and Connors, B.W. (2012). Thalamic control of layer 1 circuits in prefrontal cortex. Journal of Neuroscience *32*, 17813–17823.

Cruikshank, S.J., Urabe, H., Nurmikko, A.V., and Connors, B.W. (2010). Pathway-specific feedforward circuits between thalamus and neocortex revealed by selective optical stimulation of axons. Neuron *65*, 230–245.

Cubelos, B., Sebastián-Serrano, A., Beccari, L., Calcagnotto, M.E., Cisneros, E., Kim, S., Dopazo, A., Alvarez-Dolado, M., Redondo, J.M., Bovolenta, P., et al. (2010). Cux1 and Cux2 regulate dendritic branching, spine morphology, and

synapses of the upper layer neurons of the cortex. Neuron *66*, 523–535.

Decoville, M., Giacomello, E., Leng, M., and Locker, D. (2001). DSP1, an HMG-like protein, is involved in the regulation of homeotic genes. Genetics *157*, 237–244.

Déjardin, J., Rappailles, A., Cuvier, O., Grimaud, C., Decoville, M., Locker, D., and Cavalli, G. (2005). Recruitment of Drosophila Polycomb group proteins to chromatin by DSP1. Nature *434*, 533–538.

Diaz, F., McKeehan, N., Kang, W., and Hébert, J.M. (2013). Apoptosis of glutamatergic neurons fails to trigger a neurogenic response in the adult neocortex. Journal of Neuroscience *33*, 6278–6284.

Dufour, A., Seibt, J., Passante, L., Depaepe, V., Ciossek, T., Frisén, J., Kullander, K., Flanagan, J.G., Polleux, F., and Vanderhaeghen, P. (2003). Area Specificity and Topography of Thalamocortical Projections Are Controlled by ephrin/Eph Genes. Neuron *39*, 453–465.

Egan, C.M., Nyman, U., Skotte, J., Streubel, G., and Turner, S. (2013a). CHD5 Is Required for Neurogenesis and Has a Dual Role in Facilitating Gene Expression and Polycomb Gene Repression. Dev. Cell.

Egan, C.M., Nyman, U., Skotte, J., Streubel, G., Turner, S., O'Connell, D.J., Rraklli, V., Dolan, M.J., Chadderton, N., Hansen, K., et al. (2013b). CHD5 is required for neurogenesis and has a dual role in facilitating gene expression and polycomb gene repression. Dev. Cell *26*, 223–236.

Encinas, J.M., Michurina, T.V., Peunova, N., Park, J.-H., Tordo, J., Peterson, D.A., Fishell, G., Koulakov, A., and Enikolopov, G. (2011). Division-coupled astrocytic differentiation and age-related depletion of neural stem cells in the adult hippocampus. Cell Stem Cell *8*, 566–579.

Englund, C., Fink, A., Lau, C., Pham, D., Daza, R.A.M., Bulfone, A., Kowalczyk, T., and Hevner, R.F. (2005). Pax6, Tbr2, and Tbr1 are expressed sequentially by radial glia, intermediate progenitor cells, and postmitotic neurons in developing neocortex. Journal of Neuroscience *25*, 247–251.

Franceschini, A., Szklarczyk, D., Frankild, S., Kuhn, M., Simonovic, M., Roth, A., Lin, J., Minguez, P., Bork, P., Mering, von, C., et al. (2013). STRING v9.1: protein-protein interaction networks, with increased coverage and integration. Nucleic Acids Res. *41*, D808–D815.

Fujioka, M., Yusibova, G.L., Zhou, J., and Jaynes, J.B. (2008). The DNA-binding Polycomb-group protein Pleiohomeotic maintains both active and repressed transcriptional states through a single site. Development *135*, 4131–4139.

Gabellini, D., Green, M.R., and Tupler, R. (2002). Inappropriate gene activation in FSHD: a repressor complex binds a chromosomal repeat deleted in dystrophic

muscle. Cell *110*, 339–348.

Gabriel Gonzales-Roybal, D.A.L. (2013). Chromatin-based epigenetics of adult subventricular zone neural stem cells. Front Genet *4*.

Gadea, A., Aguirre, A., Haydar, T.F., and Gallo, V. (2009). Endothelin-1 regulates oligodendrocyte development. J Neurosci *29*, 10047–10062.

Ge, S., Yang, C.-H., Hsu, K.-S., Ming, G.-L., and Song, H. (2007). A critical period for enhanced synaptic plasticity in newly generated neurons of the adult brain. Neuron *54*, 559–566.

Haan, N., Goodman, T., Najdi-Samiei, A., Stratford, C.M., Rice, R., Agha, El, E., Bellusci, S., and Hajihosseini, M.K. (2013). Fgf10-expressing tanycytes add new neurons to the appetite/energy-balance regulating centers of the postnatal and adult hypothalamus. Journal of Neuroscience *33*, 6170–6180.

Hainsworth, A.H., Brittain, J.F., and Khatun, H. (2012). Pre-clinical models of human cerebral small vessel disease: Utility for clinical application. J Neurol Sci.

He, F., Ge, W., Martinowich, K., Becker-Catania, S., Coskun, V., Zhu, W., Wu, H., Castro, D., Guillemot, F., Fan, G., et al. (2005). A positive autoregulatory loop of Jak-STAT signaling controls the onset of astrogliogenesis. Nat Neurosci *8*, 616–625.

He, Z., Yamawaki, T., Yang, S., Day, A.L., Simpkins, J.W., and Naritomi, H. (1999). Experimental model of small deep infarcts involving the hypothalamus in rats: changes in body temperature and postural reflex. Stroke *30*, 2743–51– discussion2751.

Hirabayashi, Y., and Gotoh, Y. (2010). Epigenetic control of neural precursor cell fate during development. Nat Rev Neurosci *11*, 377–388.

Hirabayashi, Y., Suzki, N., Tsuboi, M., Endo, T.A., Toyoda, T., Shinga, J., Koseki, H., Vidal, M., and Gotoh, Y. (2009a). Polycomb limits the neurogenic competence of neural precursor cells to promote astrogenic fate transition. Neuron *63*, 600–613.

Hirabayashi, Y., Suzki, N., Tsuboi, M., Endo, T.A., Toyoda, T., Shinga, J., Koseki, H., Vidal, M., and Gotoh, Y. (2009b). Polycomb Limits the Neurogenic Competence of Neural Precursor Cells to Promote Astrogenic Fate Transition. Neuron *63*, 600–613.

Ho, L., and Crabtree, G.R. (2010). Chromatin remodelling during development. Nature *463*, 474–484.

Hock, R., Furusawa, T., Ueda, T., and Bustin, M. (2007). HMG chromosomal proteins in development and disease. Trends Cell Biol *17*, 72–79.

Hooks, B.M., Mao, T., Gutnisky, D.A., Yamawaki, N., Svoboda, K., and Shepherd,

G.M.G. (2013). Organization of cortical and thalamic input to pyramidal neurons in mouse motor cortex. Journal of Neuroscience *33*, 748–760.

Horie, N., Maag, A.-L., Hamilton, S.A., Shichinohe, H., Bliss, T.M., and Steinberg, G.K. (2008). Mouse model of focal cerebral ischemia using endothelin-1. J Neurosci Methods *173*, 286–290.

Hu, X.-L., Wang, Y., and Shen, Q. (2012). Epigenetic control on cell fate choice in neural stem cells. Protein Cell *3*, 278–290.

Huang, J., Li, Y., Tang, Y., Tang, G., Yang, G.-Y., and Wang, Y. (2013). CXCR4 Antagonist AMD3100 Protects Blood-Brain Barrier Integrity and Reduces Inflammatory Response After Focal Ischemia in Mice. Stroke *44*, 190–197.

Huang, Z.J. (2014). Toward a genetic dissection of cortical circuits in the mouse. Neuron *83*, 1284–1302.

Hwang, W.W., Salinas, R.D., Siu, J.J., Kelley, K.W., Delgado, R.N., Paredes, M.F., Alvarez-Buylla, A., Oldham, M.C., and Lim, D.A. (2014). Distinct and separable roles for EZH2 in neurogenic astroglia. Elife *3*, e02439.

Ishino, Y., Hayashi, Y., Naruse, M., Tomita, K., Sanbo, M., Fuchigami, T., Fujiki, R., Hirose, K., Toyooka, Y., Fujimori, T., et al. (2014). Bre1a, a histone H2B ubiquitin ligase, regulates the cell cycle and differentiation of neural precursor cells. Journal of Neuroscience *34*, 3067–3078.

Jacquet, B.V., Muthusamy, N., Sommerville, L.J., Xiao, G., Liang, H., Zhang, Y., Holtzman, M.J., and Ghashghaei, H.T. (2011). Specification of a Foxj1-dependent lineage in the forebrain is required for embryonic-to-postnatal transition of neurogenesis in the olfactory bulb. Journal of Neuroscience *31*, 9368–9382.

Jacquet, B.V., Salinas-Mondragon, R., Liang, H., Therit, B., Buie, J.D., Dykstra, M., Campbell, K., Ostrowski, L.E., Brody, S.L., and Ghashghaei, H.T. (2009). FoxJ1-dependent gene expression is required for differentiation of radial glia into ependymal cells and a subset of astrocytes in the postnatal brain. Development *136*, 4021–4031.

Janke, C., Martin, D., Giraud-Panis, M.-J., Decoville, M., and Locker, D. (2003). Drosophila DSP1 and rat HMGB1 have equivalent DNA binding properties and share a similar secondary fold. J. Biochem. *133*, 533–539.

Janz, P., and Illing, R.-B. (2014). A role for microglial cells in reshaping neuronal circuitry of the adult rat auditory brainstem after its sensory deafferentation. J Neurosci Res *92*, 432–445.

Jeljeli, M., Strazielle, C., Caston, J., and Lalonde, R. (2003). Effects of ventrolateral-ventromedial thalamic lesions on motor coordination and spatial orientation in rats. Neurosci. Res. *47*, 309–316.

Jin, K., Wang, X., Xie, L., Mao, X.O., Zhu, W., Wang, Y., Shen, J., Mao, Y., Banwait, S., and Greenberg, D.A. (2006). Evidence for stroke-induced neurogenesis in the human brain. Proc Natl Acad Sci USA *103*, 13198–13202.

Jobe, E.M., McQuate, A.L., and Zhao, X. (2012). Crosstalk among Epigenetic Pathways Regulates Neurogenesis. Front Neurosci *6*, 59.

Juliandi, B., Abematsu, M., and Nakashima, K. (2010). Epigenetic regulation in neural stem cell differentiation. Development, Growth & Differentiation *52*, 493–504.

Kausar, H., and Antonios, N. (2013). Combined thalamic ptosis and astasia. J Clin Neurosci *20*, 1471–1474.

Kim, J., and Kim, H. (2012). Recruitment and biological consequences of histone modification of H3K27me3 and H3K9me3. Ilar J *53*, 232–239.

Kishi, Y., Fujii, Y., Hirabayashi, Y., and Gotoh, Y. (2012). HMGA regulates the global chromatin state and neurogenic potential in neocortical precursor cells. Nat Neurosci *15*, 1127–1133.

Kokoeva, M.V., Yin, H., and Flier, J.S. (2005). Neurogenesis in the hypothalamus of adult mice: potential role in energy balance. Science *310*, 679–683.

Kokovay, E., Goderie, S., Wang, Y., Lotz, S., Lin, G., Sun, Y., Roysam, B., Shen, Q., and Temple, S. (2010). Adult SVZ Lineage Cells Home to and Leave the Vascular Niche via Differential Responses to SDF1/CXCR4 Signaling. Cell Stem Cell *7*, 163–173.

Kokovay, E., Wang, Y., Kusek, G., Wurster, R., Lederman, P., Lowry, N., Shen, Q., and Temple, S. (2012). VCAM1 Is Essential to Maintain the Structure of the SVZ Niche and Acts as an Environmental Sensor to Regulate SVZ Lineage Progression. Cell Stem Cell *11*, 220–230.

Kreuzberg, M., Kanov, E., Timofeev, O., Schwaninger, M., Monyer, H., and Khodosevich, K. (2010). Increased subventricular zone-derived cortical neurogenesis after ischemic lesion. Exp Neurol *226*, 90–99.

Kriegstein, A., and Alvarez-Buylla, A. (2009). The glial nature of embryonic and adult neural stem cells. Annu. Rev. Neurosci. *32*, 149–184.

Kusek, G., Campbell, M., Doyle, F., Tenenbaum, S.A., Kiebler, M., and Temple, S. (2012). Asymmetric segregation of the double-stranded RNA binding protein Staufen2 during mammalian neural stem cell divisions promotes lineage progression. Cell Stem Cell *11*, 505–516.

Lanzuolo, C., and Orlando, V. (2012). Memories from the Polycomb Group Proteins. Annu. Rev. Genet. *46*, 561–589.

Lee, S., Nam, Y., Koo, J.Y., Lim, D., Park, J., Ock, J., Kim, J., Suk, K., and Park, S.B. (2014). A small molecule binding HMGB1 and HMGB2 inhibits microglia-mediated neuroinflammation. Nat Chem Biol *10*, 1055–1060.

Li, J., Tang, Y., Purkayastha, S., Yan, J., and Cai, D. (2014). Control of obesity and glucose intolerance via building neural stem cells in the hypothalamus. Mol Metab *3*, 313–324.

Lian, G., Lu, J., Hu, J., Zhang, J., Cross, S.H., Ferland, R.J., and Sheen, V.L. (2012). Filamin A Regulates Neural Progenitor Proliferation and Cortical Size through Wee1-Dependent Cdk1 Phosphorylation.

Lim, D.A., and Alvarez-Buylla, A. (2014). Adult neural stem cells stake their ground. Trends Neurosci *37*, 563–571.

Lim, D.A., Huang, Y.-C., Swigut, T., Mirick, A.L., Garcia-Verdugo, J.M., Wysocka, J., Ernst, P., and Alvarez-Buylla, A. (2009). Chromatin remodelling factor Mll1 is essential for neurogenesis from postnatal neural stem cells. Nature *458*, 529–533.

Ma, D.K., Marchetto, M.C., Guo, J.U., Ming, G.-L., Gage, F.H., and Song, H. (2010). Epigenetic choreographers of neurogenesis in the adult mammalian brain. Nat Neurosci *13*, 1338–1344.

Macrae, I.M., Robinson, M.J., Graham, D.I., Reid, J.L., and McCulloch, J. (1993). Endothelin-1-Induced Reductions in Cerebral Blood Flow: Dose Dependency, Time Course, and Neuropathological Consequences. Journal of Cerebral Blood Flow & Metabolism *13*, 276–284.

Malarkey, C.S., and Churchill, M.E.A. (2012). The high mobility group box: the ultimate utility player of a cell. Trends in Biochemical Sciences *37*, 553–562.

Margueron, R., and Reinberg, D. (2011). The Polycomb complex PRC2 and its mark in life. Nature *469*, 343–349.

Marin, O., Valiente, M., Ge, X., and Tsai, L.-H. (2010). Guiding neuronal cell migrations. Cold Spring Harb Perspect Biol *2*, a001834.

McClatchy, D.B., Liao, L., Park, S.K., Xu, T., Lu, B., and Yates Iii, J.R. (2011). Differential proteomic analysis of mammalian tissues using SILAM. PLoS ONE *6*, e16039.

Mellén, M., Ayata, P., Dewell, S., Kriaucionis, S., and Heintz, N. (2012). MeCP2 binds to 5hmC enriched within active genes and accessible chromatin in the nervous system. Cell *151*, 1417–1430.

Mikita, J., Dubourdieu-Cassagno, N., Deloire, M.S., Vekris, A., Biran, M., Raffard, G., Brochet, B., Canron, M.-H., Franconi, J.-M., Boiziau, C., et al. (2011). Altered

M1/M2 activation patterns of monocytes in severe relapsing experimental rat model of multiple sclerosis. Amelioration of clinical status by M2 activated monocyte administration. Mult Scler *17*, 2–15.

Ming, G.-L., and Song, H. (2011). Adult neurogenesis in the mammalian brain: significant answers and significant questions. Neuron *70*, 687–702.

Mirzadeh, Z., Doetsch, F., Sawamoto, K., Wichterle, H., and Alvarez-Buylla, A. (2010). The subventricular zone en-face: wholemount staining and ependymal flow. J Vis Exp.

Mirzadeh, Z., Merkle, F.T., Soriano-Navarro, M., Garcia-Verdugo, J.M., and Alvarez-Buylla, A. (2008). Neural stem cells confer unique pinwheel architecture to the ventricular surface in neurogenic regions of the adult brain. Cell Stem Cell *3*, 265–278.

Mohajerani, M.H., Aminoltejari, K., and Murphy, T.H. (2011). Targeted mini-strokes produce changes in interhemispheric sensory signal processing that are indicative of disinhibition within minutes. Proc Natl Acad Sci USA *108*, E183–E191.

Molofsky, A.V., He, S., Bydon, M., Morrison, S.J., and Pardal, R. (2005). Bmi-1 promotes neural stem cell self-renewal and neural development but not mouse growth and survival by repressing the p16Ink4a and p19Arf senescence pathways. Genes Dev *19*, 1432–1437.

Monconduit, L., and Villanueva, L. (2005). The lateral ventromedial thalamic nucleus spreads nociceptive signals from the whole body surface to layer I of the frontal cortex. Eur. J. Neurosci. *21*, 3395–3402.

Mozaffarian, D., Benjamin, E.J., Go, A.S., Arnett, D.K., Blaha, M.J., Cushman, M., de Ferranti, S., Després, J.-P., Fullerton, H.J., Howard, V.J., et al. (2015a). Executive summary: heart disease and stroke statistics-2015 update: a report from the american heart association. Circulation *131*, 434–441.

Mozaffarian, D., Benjamin, E.J., Go, A.S., Arnett, D.K., Blaha, M.J., Cushman, M., de Ferranti, S., Després, J.-P., Fullerton, H.J., Howard, V.J., et al. (2015b). Heart disease and stroke statistics-2015 update: a report from the american heart association. Circulation *131*, e29–e322.

Neumann, J., Gunzer, M., Gutzeit, H.O., Ullrich, O., Reymann, K.G., and Dinkel, K. (2006). Microglia provide neuroprotection after ischemia. Faseb J. *20*, 714–716.

Neumann, J., Sauerzweig, S., Rönicke, R., Gunzer, F., Dinkel, K., Ullrich, O., Gunzer, M., and Reymann, K.G. (2008). Microglia cells protect neurons by direct engulfment of invading neutrophil granulocytes: a new mechanism of CNS immune privilege. Journal of Neuroscience *28*, 5965–5975.

Nishino, J., Kim, I., Chada, K., and Morrison, S.J. (2008). Hmga2 promotes neural stem cell self-renewal in young but not old mice by reducing p16Ink4a and p19Arf Expression. Cell *135*, 227–239.

Niv, F., Keiner, S., Krishna, K., Witte, O.W., Lie, D.C., and Redecker, C. (2012). Aberrant Neurogenesis After Stroke: A Retroviral Cell Labeling Study. Stroke *43*, 2468–2475.

Ohab, J.J., and Carmichael, S.T. (2008). Poststroke neurogenesis: emerging principles of migration and localization of immature neurons. Neuroscientist *14*, 369–380.

Orsi, G.A., Kasinathan, S., Zentner, G.E., Henikoff, S., and Ahmad, K. (2015). Mapping regulatory factors by immunoprecipitation from native chromatin. Curr Protoc Mol Biol *110*, 21.31.1–21.31.25.

Paez-Gonzalez, P., Asrican, B., Rodriguez, E., and Kuo, C.T. (2014). Identification of distinct ChAT(+) neurons and activity-dependent control of postnatal SVZ neurogenesis. Nat Neurosci.

Papuć, E., Wojczal, J., Stelmasiak, Z., and Rejdak, K. (2012). Bilateral paramedian thalamic infarction with hypothalamic dysfunction. Neurol. Neurochir. Pol. *46*, 279–283.

Paton, J.A., and Nottebohm, F.N. (1984). Neurons generated in the adult brain are recruited into functional circuits. Science *225*, 1046–1048.

Polo-Parada, L., Bose, C.M., Plattner, F., and Landmesser, L.T. (2004). Distinct roles of different neural cell adhesion molecule (NCAM) isoforms in synaptic maturation revealed by analysis of NCAM 180 kDa isoform-deficient mice. Journal of Neuroscience *24*, 1852–1864.

Prasad, R., Liu, Y., Deterding, L.J., Poltoratsky, V.P., Kedar, P.S., Horton, J.K., Kanno, S.-I., Asagoshi, K., Hou, E.W., Khodyreva, S.N., et al. (2007). HMGB1 is a cofactor in mammalian base excision repair. Mol Cell *27*, 829–841.

Raponi, E., Agenes, F., Delphin, C., Assard, N., Baudier, J., Legraverend, C., and Deloulme, J.-C. (2007). S100B expression defines a state in which GFAP-expressing cells lose their neural stem cell potential and acquire a more mature developmental stage. Glia *55*, 165–177.

Ringrose, L., and Paro, R. (2007). Polycomb/Trithorax response elements and epigenetic memory of cell identity. Development *134*, 223–232.

Robins, S.C., Stewart, I., McNay, D.E., Taylor, V., Giachino, C., Goetz, M., Ninkovic, J., Briancon, N., Maratos-Flier, E., Flier, J.S., et al. (2013a). α-Tanycytes of the adult hypothalamic third ventricle include distinct populations of FGF-responsive neural progenitors. Nat Comms *4*, 2049.

Robins, S.C., Trudel, E., Rotondi, O., Liu, X., Djogo, T., Kryzskaya, D., Bourque, C.W., and Kokoeva, M.V. (2013b). Evidence for NG2-glia Derived, Adult-Born Functional Neurons in the Hypothalamus. PLoS ONE *8*, e78236.

Rojczyk-Gołębiewska, E., Pałasz, A., and Wiaderkiewicz, R. (2014). Hypothalamic Subependymal Niche: A Novel Site of the Adult Neurogenesis. Cell. Mol. Neurobiol.

Ronfani, L., Ferraguti, M., Croci, L., Ovitt, C.E., Schöler, H.R., Consalez, G.G., and Bianchi, M.E. (2001). Reduced fertility and spermatogenesis defects in mice lacking chromosomal protein Hmgb2. *128*, 1265–1273.

Rybak, A. (2009). Expression and function of the let-7 microRNA during stem cell specification and development of the CNS.

Sahay, A., Scobie, K.N., Hill, A.S., O'Carroll, C.M., Kheirbek, M.A., Burghardt, N.S., Fenton, A.A., Dranovsky, A., and Hen, R. (2011). Increasing adult hippocampal neurogenesis is sufficient to improve pattern separation. Nature *472*, 466–470.

Sawamoto, K., Wichterle, H., Gonzalez-Perez, O., Cholfin, J.A., Yamada, M., Spassky, N., Murcia, N.S., Garcia-Verdugo, J.M., Marin, O., Rubenstein, J.L.R., et al. (2006). New neurons follow the flow of cerebrospinal fluid in the adult brain. Science *311*, 629–632.

Schatz, D.G., and Swanson, P.C. (2011). V(D)J Recombination: Mechanisms of Initiation. Annu. Rev. Genet. *45*, 167–202.

Schmahmann, J.D. (2003). Vascular Syndromes of the Thalamus. Stroke.

Shechter, D., Dormann, H.L., Allis, C.D., and Hake, S.B. (2007). Extraction, purification and analysis of histones. Nat Protoc *2*, 1445–1457.

Shen, Q., Wang, Y., Kokovay, E., Lin, G., Chuang, S.-M., Goderie, S.K., Roysam, B., and Temple, S. (2008). Adult SVZ Stem Cells Lie in a Vascular Niche: A Quantitative Analysis of Niche Cell-Cell Interactions. Cell Stem Cell *3*, 289–300.

Shen, X., Kim, W., Fujiwara, Y., Simon, M.D., Liu, Y., Mysliwiec, M.R., Yuan, G.-C., Lee, Y., and Orkin, S.H. (2009). Jumonji Modulates Polycomb Activity and Self-Renewal versus Differentiation of Stem Cells. Cell *139*, 1303–1314.

Sierra, A., Encinas, J.M., Deudero, J.J.P., Chancey, J.H., Enikolopov, G., Overstreet-Wadiche, L.S., Tsirka, S.E., and Maletic-Savatic, M. (2010). Microglia shape adult hippocampal neurogenesis through apoptosis-coupled phagocytosis. Cell Stem Cell *7*, 483–495.

Sozmen, E.G., Hinman, J.D., and Carmichael, S.T. (2012). Models that matter: white matter stroke models. Neurotherapeutics *9*, 349–358.

Sozmen, E.G., Kolekar, A., Havton, L.A., and Carmichael, S.T. (2009). A white matter stroke model in the mouse: axonal damage, progenitor responses and MRI correlates. J Neurosci Methods *180*, 261–272.

Sparmann, A., Xie, Y., Verhoeven, E., Vermeulen, M., Lancini, C., Gargiulo, G., Hulsman, D., Mann, M., Knoblich, J.A., and van Lohuizen, M. (2013a). The chromodomain helicase Chd4 is required for Polycomb-mediated inhibition of astroglial differentiation. The EMBO Journal *32*, 1598–1612.

Sparmann, A., Xie, Y., Verhoeven, E., Vermeulen, M., Lancini, C., Gargiulo, G., Hulsman, D., Mann, M., Knoblich, J.A., and van Lohuizen, M. (2013b). The chromodomain helicase Chd4 is required for Polycomb-mediated inhibition of astroglial differentiation. The EMBO Journal *32*, 1598–1612.

Stros, M. (2010). HMGB proteins: interactions with DNA and chromatin. Biochim. Biophys. Acta *1799*, 101–113.

Sun, W., Guan, M., and Li, X. (2014). 5-hydroxymethylcytosine-mediated DNA demethylation in stem cells and development. Stem Cells and Development 140108125209002.

Sun, Y., Nadal-Vicens, M., Misono, S., Lin, M.Z., Zubiaga, A., Hua, X., Fan, G., and Greenberg, M.E. (2001). Neurogenin promotes neurogenesis and inhibits glial differentiation by independent mechanisms. Cell *104*, 365–376.

Szulwach, K.E., Li, X., Li, Y., Song, C.-X., Wu, H., Dai, Q., Irier, H., Upadhyay, A.K., Gearing, M., Levey, A.I., et al. (2011). 5-hmC–mediated epigenetic dynamics during postnatal neurodevelopment and aging. Nat Neurosci *14*, 1607–1616.

Taniguchi, N., Carames, B., Kawakami, Y., Amendt, B.A., Komiya, S., and Lotz, M. (2009a). Chromatin protein HMGB2 regulates articular cartilage surface maintenance via beta-catenin pathway. Proc Natl Acad Sci USA *106*, 16817–16822.

Taniguchi, N., Carames, B., Ronfani, L., Ulmer, U., Komiya, S., Bianchi, M.E., and Lotz, M. (2009b). Aging-related loss of the chromatin protein HMGB2 in articular cartilage is linked to reduced cellularity and osteoarthritis. Proc Natl Acad Sci USA *106*, 1181–1186.

Tennant, K.A., and Jones, T.A. (2009). Sensorimotor behavioral effects of endothelin-1 induced small cortical infarcts in C57BL/6 mice. J Neurosci Methods *181*, 18–26.

Testa, G. (2011). The time of timing: How Polycomb proteins regulate neurogenesis. Bioessays *33*, 519–528.

Thiel, A., and Heiss, W.-D. (2011). Imaging of microglia activation in stroke. Stroke *42*, 507–512.

Tong, C.K., Chen, J., Cebrián-Silla, A., Mirzadeh, Z., Obernier, K., Guinto, C.D., Tecott, L.H., Garcia-Verdugo, J.M., Kriegstein, A., and Alvarez-Buylla, A. (2014). Axonal Control of the Adult Neural Stem Cell Niche. Cell Stem Cell.

Viaene, A.N., Petrof, I., and Sherman, S.M. (2011). Synaptic properties of thalamic input to layers 2/3 and 4 of primary somatosensory and auditory cortices. J. Neurophysiol. *105*, 279–292.

Wang, Y., Jin, K., and Greenberg, D.A. (2007). Neurogenesis associated with endothelin-induced cortical infarction in the mouse. Brain Research *1167*, 118–122.

Wu, M., Nissen, J.C., Chen, E.I., and Tsirka, S.E. (2012). Tuftsin promotes an anti-inflammatory switch and attenuates symptoms in experimental autoimmune encephalomyelitis. PLoS ONE *7*, e34933.

Xu, K., Wu, Z., Renier, N., Antipenko, A., Tzvetkova-Robev, D., Xu, Y., Minchenko, M., Nardi-Dei, V., Rajashankar, K.R., Himanen, J., et al. (2014). Neural migration. Structures of netrin-1 bound to two receptors provide insight into its axon guidance mechanism. Science *344*, 1275–1279.

Xu, Y., Tamamaki, N., Noda, T., Kimura, K., Itokazu, Y., Matsumoto, N., Dezawa, M., and Ide, C. (2005). Neurogenesis in the ependymal layer of the adult rat 3rd ventricle. Exp Neurol *192*, 251–264.

Yamashita, T., and Ninomiya, M. (2006). Subventricular zone-derived neuroblasts migrate and differentiate into mature neurons in the post-stroke adult striatum. The Journal of ….

Zhang, R.L., LeTourneau, Y., Gregg, S.R., Wang, Y., Toh, Y., Robin, A.M., Zhang, Z.G., and Chopp, M. (2007). Neuroblast division during migration toward the ischemic striatum: a study of dynamic migratory and proliferative characteristics of neuroblasts from the subventricular zone. Journal of Neuroscience *27*, 3157–3162.

(1994). An approach to correlate tandem mass spectral data of peptides with amino acid sequences in a protein database. *5*, 976–989.

(2004a). The International Protein Index: an integrated database for proteomics experiments. *4*, 1985–1988.

(2004b). A model for random sampling and estimation of relative protein abundance in shotgun proteomics. *76*, 4193–4201.

(2004c). The Mouse Brain in Stereotaxic Coordinates - George Paxinos, Keith B. J. Franklin - Google Books.

(2005). Fluoro Jade-B Detection of Dying Cells in the SVZ and RMS of Adult Rats After Bilateral Olfactory Bulbectomy - Springer.

(2006). Cerebral Blood Flow Threshold of Ischemic Penumbra and Infarct Core in Acute Ischemic Stroke: A Systematic Review. *37*, 1334–1339.

(2007a). Catch-and-Release Reagents for Broadscale Quantitative Proteomics Analyses - Journal of Proteome Research (ACS Publications).

(2007b). Genome-wide atlas of gene expression in the adult mouse brain. *445*, 168–176.

(2008). American Statistical Association Portal :: High-Dimensional Sparse Factor Modeling: Applications in Gene Expression Genomics - Journal of the American Statistical Association - Volume 103, Issue 484.

(2010). Automated home-cage behavioural phenotyping of mice. *1*, 1–9.

(2012). Fiji: an open-source platform for biological-image analysis. *9*, 676–682.

(2014a). The artery of percheron and etiologies of bilateral thalamic stroke. *81*, 80–82.

(2014b). High-resolution mapping of transcription factor binding sites on native chromatin : Nature Methods : Nature Publishing Group.

(2015a). Common misconceptions about data analysis and statistics. *172*, 2126–2132.

(2015b). Late-onset thermal hypersensitivity after focal ischemic thalamic infarcts as a model for central post-stroke pain in rats.